MITIGATING THE IMPACT OF OCEAN AMBIENT NOISE IN AN UNDERWATER ACOUSTIC COMMUNICATION SYSTEM

by

Afolarin Egbewande

Submitted in partial fulfillment of the requirements
for the degree of Doctor of Philosophy

at

Dalhousie University
Halifax, Nova Scotia
February 2022

Table of Contents

List of Tables

List of Figures

List of Abbreviations Used

ADC	Analog-to-Digital Converter
ADEON	Atlantic Deepwater Ecosystem Observatory Network
AF	Array Factor
AIS	Automatic Identification System
AMAR	Autonomous Multichannel Acoustic Recorder
AR	Autoregressive
BER	Bit-error Rate
CANAPE	Canadian Basin Acoustic Propagation Experiment
CB-MFP	Coherence-based Matched-field Processing
CIR	Channel Impulse Response
CPA	Closest Point of Approach
CRB	Cramer Rao Bounds
CSD	Cross-spectral Density
DFE	Decision-feedback Equalizer
DOA	Direction of Arrival
EM	Electromagnetic
HLA	Horizontal-line Arrays
IoUT	Internet of Underwater Things
ISI	inter-symbol Interference
LTE	Long-term Evolution
MAC	Media Access Control
MFP	Matched-field Processing
MI	Magneto-Inductive

MIMO	Multi-Input Multi-Output
ML-BF	Maximum-likelihood Beamformer
MMSE	Minimum Mean-square Error
MVDR	Minimum Variance Distortionless Response
NR	New-Radio
OAN	Ocean Ambient Noise
OFDM	Orthogonal Frequency-Division Multiplexing
PSD	Power Spectral Density
ROV	Remotely-Operated Vehicles
RRC	Root-Raised Cosine
SNR	Signal-to-noise Ratio
SSP	Sound Speed Profile
TDOA	Time-difference of Arrival
ULA	Uniformly-linear Array
UWA	Underwater Acoustics
UWAC	Underwater Acoustics Communication
VLA	Vertical-line Array

Abstract

In wireless communication links, receivers are typically designed to mitigate the variability in the propagation channel in presence of arbitrary white Gaussian noise. However, the variations in the instantaneous channel properties introduce high statistical variability in the communication link reliability. In fact, the underwater acoustic channel in the ocean is particularly sensitive to the changes in environmental conditions. Extensive research has been done on the propagation but it is typically assumed that ocean noise compares with terrestrial noise in the design of underwater acoustic receivers. This assumption does not accurately represent the impact of ocean ambient noise on the performance of underwater acoustic communication systems, particularly when using receiver arrays.

This dissertation studies the unique properties of oceanic ambient noise, particularly the variability in its directional properties. The application developed in this work focuses on both anthropogenic noise due to vessels and naturally occurring ambient noise within the channel bandwidth. To this end, the characteristics of these noise sources and their impact on the underwater acoustic link are discussed in this dissertation.

Firstly, using a compact receiver array, an acoustic source tracking procedure is designed to characterize the directional properties of vessel noise. This is achieved using a maximum-likelihood beamformer to estimate the bearing and a coherence-based matched-field processor to estimate the range of a vessel over its travel duration. Although the performance of most methodologies developed for characterizing vessel noise in literature are evaluated using computer simulations, the algorithm applied in this dissertation are tested with actual measurements of vessel noise from ocean experiments. It is observed that the noise directionality can be estimated accurately using a compact array but relies on the geometry of the array.

Secondly, noise models are developed to characterize the unique properties of naturally occurring ambient noise at a compact array of acoustic receivers. Synthetic ambient noise is generated with defined properties and validated against measured ambient noise.

Thirdly, the performance of a space-time receiver for signals processed in measured ambient noise is validated against signals processed in synthetic noise processes. It is observed that the variations in the space-time properties of ambient noise do not compare with the usual uncorrelated noise assumption in the design of an underwater acoustic receiver. Also, the bit-error rate of the space-time filter depends on optimizing the training and payload duration in the received signal to adapt to the time-varying property of ocean ambient noise.

Acknowledgements

First, my appreciation goes to my supervisor Dr. Jean-François Bousquet for giving me the opportunity to work on this project and other projects during my doctorate program. My sincere appreciation also goes to my supervisory committee – Dr. David Barclay, Dr. Robert Adamson and Dr. Jose Gonzalez-Cueto for their constructive comments toward the completion of this work.

I am grateful to Mitacs for the Accelerate Award and to Jasco Applied Sciences Nova Scotia who provided funds and some of the data sets used in this work. Special thanks to the Applied Science team at Jasco, particularly to Dr. Bruce Martin for his helpful insights and guidance toward the successful completion of this work. My gratitude also goes to Dr. Lanfranco Muzi for being there to help throughout this work especially with navigating the remote-work environment. I must also express my gratitude to wonderful friends – Mboza Lukindo, Mary Lukindo, Ibimina Koko Yayra Gbotso – and colleagues (current and alumni) in the research group: Xiao Lui, Andrew Dobin, Surinder Singh, Hossein Ghannadrezaii, Adam Forget, and others – who have been a part of my journey during my time at the UW-STREAM lab.

I am also profoundly grateful for the support I received from my dad and siblings – Folabi, Folake and Folahan, who have always been a part of my life's and academic journey. Words will fail me to express my gratitude to my mother (who sadly passed before the end of this study), whose love and faith continues to strengthen me in my pursuits. My most profound gratitude goes to my wife – Devene, who has been so supportive since the beginning of this work. Finally, my deepest appreciation goes to God, the source of my wisdom and inspiration.

Chapter 1

Introduction

1.1 Background

It is estimated that two-thirds of the earth's surface is covered by the oceans. There are abundance of resources in the oceans, making them highly valuable to human existence. Some of the benefits derived from the oceans include food supply, travel, trade, mineral exploration, power generation, security, and leisure activities. Thus, ocean stakeholders span across a wide demography – mineral exploration companies, military and defense, governments and research institutes, just to name a few. Among these stakeholders, there has been an increasing need to deploy systems in the ocean for different applications. For instance, the oil and gas industry deploys systems to protect sub-sea infrastructure such as pipelines and cables. Systems are deployed in defense applications for intelligence and surveillance purposes. Governments are increasingly interested in protecting endangered species and managing the ocean ecosystem, while oceanographers and scientists are keen on studying trends in oceanic activities that will preserve the earth's health. As the scope of applications of underwater systems continue to grow, so does the requirements on the system performance. In fact, in recent times, there has been significant interest in deploying underwater sensor networks for integrated sensing and communication which will facilitate the IoUT

Considering the expanse of the ocean, a key challenge in the deployment of underwater sensors is with establishing and maintaining communication in-between the sensor nodes deployed at sea without the hassle of laying heavy cables. Various communication techniques have been studied throughout the years, including the use of EM propagation, MI coupling, optical transmission and acoustic waves.

EM propagation is used extensively in radios, for terrestrial communication networks. For example, in modern day applications, wideband spectra with carriers up to 50 GHz in the millimeter wave band, are being developed for 5G applications [**?**]. This

includes Wifi networks and satellite links that can establish maritime networks over the sea. However, for communication below the sea surface, EM waves are rapidly degraded by attenuation due to high conductivity in sea water [**?**]. For this reason, EM waves have only been successfully applied in short-range and high-bandwith links. In controlled conditions, researchers have demonstrated nominal improvements in the data rates achieved via EM waves, albeit for a limited range. For instance, EM wave communication was demonstrated to achieve data rates up to 500 kbps over a 90-meter range in [**?**], and up to 10 Mbps over a 100-meter range in [**?**] by first modeling the EM wave propagation before deployment. Overall, EM still requires a lot of research for it to be deployed for underwater communications.

Due to similar magnetic permeability in the air-water boundaries, MI has been a promising option for underwater wireless communications. MI has been demonstrated to be robust against multipath propagation and fading underwater [**?**]. Hence, in recent times, extensive research has been carried out to apply MI in harsh underwater environments, subject to high ambient noise levels [**?**]. Data rates up to about 1 kbps have been achieved in MI applications for ranges up to 40 meters [**?**]. However, high path loss (induced by energy conversion loses) limits MI's propagation range, hence its use is limited to short-range multi-hop applications.

Optical waves have recently been investigated as a means of communicating underwater and rely on the visible light spectrum to transmit information signals. Though they are not limited in bandwidth, they are rapidly absorbed and suffer from severe scattering underwater [**?**]. Hence, optical waves can be applied in short-range applications where a direct line-of-sight is achievable.

Although a combination of the aforementioned wireless connectivity techniques have been proposed in underwater sensor networks, acoustic waves remain the best solution for underwater wireless communications, especially for long-range applications [**?**]. Indeed, sound propagates as pressure waves and can travel over several kilometers especially at low frequencies. This property makes acoustic communications advantageous for long-range applications although confined to lower bandwidths and its inherent challenges are unique relative to that of terrestrial radio frequency (RF) communications. Hence, acoustics technology is used in this work as a means to achieve wireless connectivity underwater.

1.2 Underwater Acoustic Communications

The principle of underwater sound has probably been used by marine animals for millions of years However, the first documented reference to UWA is reportedly by Leonardo da Vinci [1] in 1490 when he wrote the following,

"*If you cause your ship to stop and place the head of a long tube in the water and place the outer extremity to your ear, you will hear ships at a great distance from you.*"

By the 20th century, the tragic sinking of the Titanic compelled different research communities to explore underwater communication with great emphasis on disaster management. It is also reported that during the world wars, UWA was applied for applications in sub-sea detection and underwater telephones. Since that time, a lot of the findings in UWA have been applied for military surveillance, submarine communications, and in recent times for underwater sensor networks and communication to ROV.

There has been significant progress in the development of the physical layer for UWA networks. However, the development of systems in terrestrial communications are at least a few decades more advanced than in UWA systems. In fact, many of the technologies and signal processing techniques are inherited from RF applications. The big challenge remains on how to optimize these techniques for acoustic systems especially at the physical layer [**?**].

In the past decade, to enable a reliable underwater communication link, there has been a growing trend to adopt multicarrier communications typically used in LTE networks and even in 5G NR [**?**], to mitigate channel distortion. In multicarrier systems, data is transmitted over multiple carriers which are normally close spaced, making the communication link resilient to interference, narrow band fading and multipath effects. A widely used multicarrier technique is the OFDM. Also, the combination of MIMO and OFDM (as in LTE and NR) has been proven to be a promising solution for UWA communication applications [**?**, **?**, **?**, **?**]. Further, adaptive modulation techniques that rely on the prediction of the statistics of the acoustic channel was described in [**?**] to maximize data rates. These techniques – multicarrier modulation, MIMO-OFDM, adaptive modulation – have been used extensively in RF communications to date. However, the uniqueness of the UWA link largely due to the medium

(water) limits the effectiveness of UWAC systems compared to RF. It is therefore important to review the constraints for UWAC systems. This will be described in Section 1.3. Then, in Section 1.4, the research objectives will be presented.

1.3 Underwater Acoustic Communication System Constraints

The structure depicted in Fig. 1.1 forms the foundation for the development of most wireless communication systems.

At the transmitter, the information signal is modulated and matched to the carrier's phase symbol by symbol. The information symbols are upsampled by a clock with a very high frequency so that the symbols can be reconstructed at the receiver with minimal errors. The information symbols are bandlimited by a pulse shaping filter to the operational bandwidth in the system specification. Typically, a single source is used to transmit the signal; however, with the advancement in space-time coding techniques, multiple transmitters have also been considered to transmit using multiple sources [**?**, **?**].

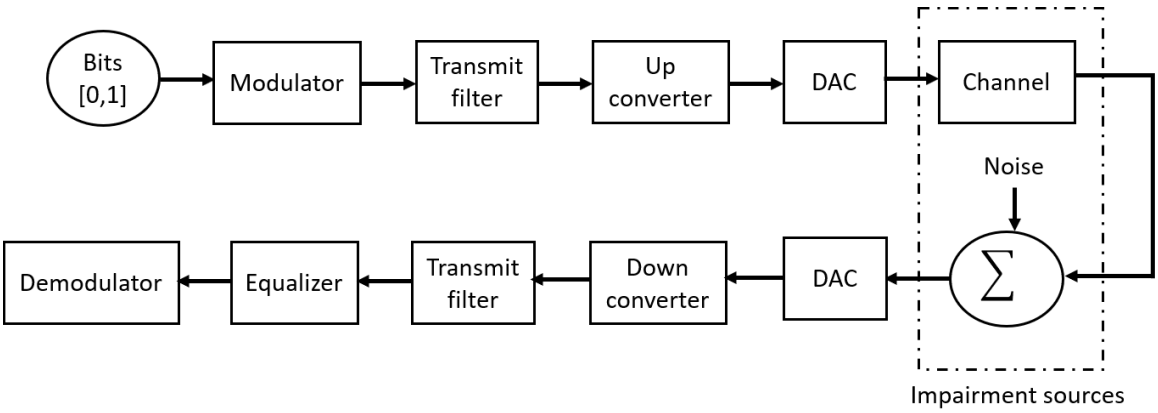

Figure 1.1: The standard structure of the UWAC system.

At the receiver, hydrophones are used to receive the information signals. The output of the hydrophone is converted to a discrete-time signal using an ADC. Usually a RRC filter is used to match the transmit filter (which is also often a RRC), to limit the bandwidth of the signal. The matched filter is designed to maximize the SNR at the receiver. The equalizer is required to mitigate the distortions (impairment sources) introduced by the propagation channel and the noise channel, while the

demodulator maps the complex baseband information symbols to the bit streams that were modulated at the transmitter.

Not shown, at the receiver, it is also crucial to synchronize the received signal, and a phase locked loop is also necessary for carrier frequency and phase recovery [**?**]. Carrier and clock recovery at the receiver is hugely important to reliably decode the information symbols. That being said, the evaluation of the receiver performance using a baseband model often ignores clock synchronization.

At the physical layer of the communication system, it is typical that the information signal is structured into frames, partitioned into training and payload durations as depicted in Fig 1.2. The training symbols contain a known sequence of bits so that the receiver can use the training duration to predict the channel characteristics before processing unknown (payload) symbols. However, the length of the training sequence reduces the spectral efficiency, and thus, the effective user throughput. Generally, the frames are repeated, i.e L_1 to L_N as in Fig 1.2, and the number of payload symbols in error in each frame is computed and used as a figure of merit to determine the performance of the communication system.

The frame structure in Fig 1.2 is generally adopted and the training symbols are used to define the equalizer coefficients to mitigate the effect of the wireless channel [2]. The linear equalizer processes the received signal with a linear filter. Two common approaches are: 1) the minimum mean-square error (MMSE) equalizer which estimates the error between the transmit information signal and the equalizer output; and 2) the zero forcing equalizer which approximates the inverse of the channel with a linear filter. An adaptive equalizer is typically a linear equalizer or a decision-feedback equalizer (DFE), which updates the equalizer parameters (such as the filter coefficients) while processing the data online. Typically, it uses the mean-squared error cost function which relies on an update procedure to minimize the error estimate between the transmit and received information symbols. Other applications rely on blind equalization techniques to estimate the transmit symbols without knowledge of the channel statistics. Although advantageous in that it does not use a portion of the channel capacity for training the filter, blind equalizers are often inadequate due to their slow convergence and/or high computational complexity.

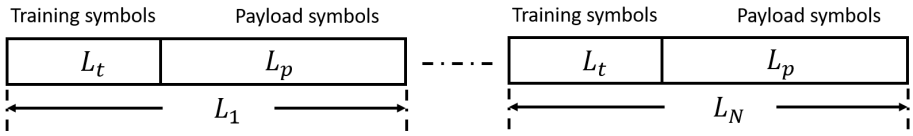

Figure 1.2: Standard frame structure showing training and payload duration in a communication system.

The evaluation of the communication performance requires an accurate representation of the distortion caused by the propagation channel as well as the noise interference at the receiver. To this end, models are usually developed for the propagation channel (or media) and the noise channel to predict their impact on the information symbols. Extensive research has been done to characterize the underwater acoustic (UWA) propagation channel and its impact on signal transmission. The current state-of-the-art shows that although there is no consensus on statistical characterization of the acoustic communication channel, however, experimental results have been demonstrated for different propagation environments so that some modeling strategies in RF has been applied for the UWAC channel [**?**]. The UWA channel is discussed in greater details in Chapter 2.

One of the challenges with UWAC is the lack of standards in the communication protocols as in LTE and NR. Most systems deployment (for sensing and acoustic communications) have relied on good practice and government restrictions as the basis for operation. One of such constraints in UWAC is the need to transmit at low power. This requirement is largely due to the threat that high power transmission poses to marine life [**?**, **?**, **?**]. Although preserving marine life is much desirable, low power transmission compounds the challenges in the UWA propagation channel. In fact, acoustic signals become more vulnerable to the noise floor at low transmit power. Furthermore, shipping noise (which has increased significantly over the years) worsens the impact of noise in UWAC systems. Hence, the need for robust UWAC systems at low transmit power has become a key topic of discussion among many research groups in recent times.

Considering the enormity of these challenges, some authors have even argued that UWA systems may never achieve higher data rates than they do right now due to the distortions from the propagation channel and the impact of noise [**?**], coupled with the susceptibility of sound waves to turbidity, salinity, and pressure gradients in the ocean.

This assertion is hugely based on the difficulties involved with mitigating channel distortions by improving systems design at the physical layer of the communication stack. However, UWAC can still be enhanced with state-of-the-art techniques in RF to achieve higher data rates. For instance, *scheduling* has been used in LTE and NR at the MAC to mitigate the small-scale and large-scale variability in the propagation channel (air) and noise [**?**]. Also, other techniques such as online antenna calibration as in LTE and NR can be applied to adapt to the varying channel conditions in UWAC. Other authors have also pointed out the advantages in applying cross-layer design in UWAC [**?**].

Considering the demand for low power transmission and the susceptibility of communication signals to ambient noise, it is important in the acoustic communication community to understand the impact of noise on the systems design even at the physical layer. Although it is common knowledge that the signals are swamped by noise at low transmit power, to the best of the author's knowledge it has not been documented in literature how the unique space-time properties of ambient noise specifically impact the UWAC space. Largely, the established knowledge about noise in RF communications has been transferred for systems design in UWAC.

It has been demonstrated in RF communication that the noise channel contains uncorrelated samples characterized by a Gaussian distribution and has equal power at all frequencies within the system's bandwidth [**?**]. This knowledge has also formed the basis of assumption about the ambient noise channel in UWAC. This assumption is particular to systems design in UWAC and not all oceanographic applications. It is very important to investigate this assumption about the noise channel to accurately characterize systems design in UWAC. Therefore, this dissertation focuses on the OAN channel and its impact on the UWAC link.

1.4 Research Motivation and Problem Statement

In an underwater communication system, the ambient noise source is unique, and standard techniques used at RF cannot be adopted. Radio noise is a combination of natural electromagnetic atmospheric noise emanating from electrical processes in the atmosphere like lightning, man-made radio frequency interference from other electrical devices, and thermal noise due to the receiver input circuits. In comparison, OAN

sources is a combination of man-made sources (due to shipping and seismic activities) and natural sources due to marine animals, precipitation and surface generated waves due to wind. The man-made sources produce impulsive noise while the naturally occurring sources could be either impulsive (as in marine mammals) or persistent (as in surface waves or shipping noise). Unlike radio noise, the spectrum of ambient noise is frequency dependent, making the samples temporally correlated. Similarly, ambient noise samples measured at an array of hydrophones are spatially correlated. These properties – temporal correlation (i.e. frequency dependence), spatial correlation as well as the impulsive spectrum makes ambient noise uniquely different from radio noise.

Ambient noise in the ocean can significantly impact the communication link. For instance in [1, **?**], ambient noise is highlighted as a limitation on the useful bandwidth in an UWAC system. Also in [**?**], the author presented closed-form approximate models for the time-invariant acoustic channel that takes into consideration a model of the acoustic path loss and the ambient noise. It was concluded that the time-varying propagation channel as well as path loss and ambient noise impact the capacity and distance of an acoustic link. Further, in [**?**] the author describes an underwater acoustic channel model that excludes the impact of ambient noise (primarily due to sea waves and sea creatures) as highly inaccurate. More recently, in [**?**], the author highlighted the major effects of ambient noise on bit-error rate using different routing protocols in an underwater sensor network. Summarily, several authors have shown that the impact of ambient noise in an UWAC link cannot be explained away. But the question remains – by how much?

However, to evaluate the performance of UWAC systems, it is typically assumed that the noise at the receiver is uncorrelated in frequency, time, and space. This is typical in wireless radio receivers, in which the noise sources are known to be uncorrelated and have a white spectrum [**?**]. This assumption underestimates the impact of acoustic OAN sources on the performance of UWAC systems. Previous works have confirmed the impact of the statistical distribution of impulsive ambient noise sources on an UWAC receiver [3, **?**, **?**, **?**], but the impact of directional ambient noise (particularly from naturally occurring sources) on UWAC is still not well understood. To the best of the author's knowledge, as at the time of writing this dissertation, there

are no models in literature that characterize the ambient noise channel (excluding the impulsive sources) in an UWAC receiver. At best, some authors have only replaced ambient noise by any frequency-dependent noise in UWAC systems.

Having established the above knowledge gap in the understanding of the OAN channel in UWAC, it is therefore important to investigate the specific attributes of the noise channel that impacts the quality of the UWAC link and some design considerations at the physical layer. This dissertation gleans from the well established knowledge about the attributes of OAN such as the directionality [4], space-time correlation [5] and the frequency dependent spectral properties [**?**] since the early days of the studies on OAN. As depicted in Fig.1.1, the characteristics of the ambient noise channel is the primary focus in this dissertation.

To this end, to provide an understanding about the characteristics of OAN, especially with respect to the acoustic communication link, three tasks are defined in this dissertation; first, the variability in the directionality of vessel noise is characterized through source sensing; second, models are described to characterize the directional, spatial and spectral properties of naturally occurring ambient noise at a compact acoustic array; and third, the impact of directional ambient noise on an UWAC link is characterized.

1.4.1 Research Objectives

The work described in this dissertation is in response to specific needs in the underwater acoustic community.

The first part of this dissertation provides an in-depth study that characterizes the unique spatial properties of vessel noise as a persistent source of ambient noise. This task approaches the spatial property by actually investigating the directional property of vessel noise.

The second part of this dissertation develops a space-time model that is able to generate synthetic ambient noise process which can be applied in modeling an UWAC link with a greater accuracy.

The third part of this work provides an analysis of the impact of ambient noise on the array gain and the bit-error rate of spatial arrays in a coherent communication system. The section focuses on the impact of surface generated and vessel noise in

an UWAC system. A system design is proposed to mitigate vessel noise in an UWAC link.

Summarily, the first part of this dissertation is two-edged in that it is developed in response to the need for an enhanced system design that uses acoustic technology to track vessels over a long range while exploiting the directional property of vessel noise. The system design estimates the position of a vessel by using its self-noise over about a 2 km range by post processing measured acoustic data. The data measurements and other scientific support were provided by Jasco Applied Sciences [1] who is also the partner organization for this project. The outcome of this design provides an understanding about the variability in the directional property of vessel noise as well as meeting the need of the partner organization for an enhanced vessel tracking system that relies on passive arrays.

Overall, this dissertation is developed in response to the need for high reliability in acoustic systems especially in noisy environments where low power transmission is also a requirement. At low transmit power, UWAC systems become more susceptible to the characteristics of ambient noise, referred to as noise in this study, especially in environments where surface generated noise levels are high. The models developed in this work are validated against actual ambient noise measurements provided by Jasco Applied Sciences and the UW-STREAM lab of Dalhousie university. The author anticipates that the results provided about the impact of ambient noise on the UWAC link would provide a baseline for modeling acoustic receivers in the UWAC research community.

1.4.2 Research Contributions

Three major contributions are highlighted in this thesis.

First, a system design that characterizes the time varying directionality of spatial ambient noise through source sensing is characterized. To this end, a system is designed to estimate the directionality of vessel noise and surface generated noise.

Second, two distinct noise models are developed to generate synthetic noise processes that represent ambient noise in a shallow water environment.

[1] Jasco Applied Sciences is an acoustics manufacturing and ocean science company with the head office based in Nova Scotia Canada.

Third, is the quantification of the impact of ambient noise on an underwater acoustic link. To this end, the impact of directional ambient noise on an UWAC systems is evaluated even in narrowband conditions.

Characterization of Directional Ambient Noise Through Acoustic Sensing

A system design that characterizes directional ambient noise through source sensing is developed in this dissertation. The system estimates the position (characterized by bearing, depth and range) of a vessel using the changes in the directional property of the noise produced by the vessel's propeller. A system-level algorithm is used to demonstrate the properties of directional vessel noise using a combination of a beamforming technique, matched-field processing (MFP) and Kalman filtering. The system compares the positional estimate of a vessel using acoustic measurement of the vessel noise with the standard satellite report on a vessel's position with a reasonable match.

The MFP technique relies on estimates of the spatial coherence of the vessel noise measured at a spatial array. Spatially coherent signals have been used in literature for several purposes including source detection. Often, the MFP algorithms rely on plane-wave beamforming techniques in which the empirical ambiguity surface is matched against the ambiguity surface of the modelled source fields. This technique is prone to errors as a result of the sidelobes induced in the beam pattern when applying the beamforming algorithms. However, the coherence-based MFP developed in this work replaces the usual beamforming technique with an algorithm that matches the empirical coherence against the modelled coherence of the noise fields. The associated challenge with sidelobes in conventional MFP techniques and the coherence-based MFP are described in greater detail in Chapter 2 and Chapter 3 respectively.

The work described in Chapter 3 contains materials that is currently under an internal review for the following publication:

- A. Egbewande, et. al, "A System Design for Vessel Tracking Using Compact Acoustic Arrays" in Journal of Acoustic Society of America - Extended Letter (Under Review).

Modelling Space-time Noise for UWAC

In a second contribution, two distinct models are developed to generate synthetic noise model at an array of narrowband acoustic receivers.

In a first model – the directionality-based model, a synthetic noise process is generated at a compact array from the directionality function of the noise field. This method extends the model presented in [4] for noise fields over vertically separated pairs of sensors to a generalized solution for a multi-element VLA. The second model – the coherence-based model generates a synthetic noise process from the spatial coherence function of the noise fields. This method relies on previous work in [**?**] in which a synthetic noise process with defines spatial coherence property is generated by applying a mixing matrix characterized by the decomposition of the complex coherence matrix. The two noise models are developed to match actual measurement scenarios described in this work.

The development of these models are justified in that they provide some fundamental understanding about the attributes of the ambient noise channel that impacts the UWAC link. Although several models have been described in literature to characterize the properties of ambient noise, they are not developed to accurately represent the transient characteristics of noise that are representative of different measurement environments, particularly at an array of receivers.

The work described in this chapter contains materials that were presented at the following conference and submitted for journal publication:

- A. Egbewande and J. Bousquet, "Space-Time Noise Characterization for Underwater Acoustic Communications," OCEANS 2018 MTS/IEEE Charleston, 2018, pp. 1-5.

- A. Egbewande, et. al, "The Effect of Directional Noise on the Reliability of an Acoustic Receiver in Shallow Environments", in IEEE Journal of Oceanic Engineering (IEEE-OES), Submitted June 2021.

Impact of Ambient Noise on Coherent Receivers

In a third contribution, the developed models are applied in a coherent UWAC system developed in baseband (excluding the carrier frequency modulation) for demonstration purposes. The received signal at an array of receivers is processed in measured ambient noise and compared with the synthetic noise processes developed in this work. In one scenario, the modulated symbols are transmitted over a controlled channel so that the impact of the ambient noise can be isolated from the propagation channel. This approach is typical in evaluating the impact on noise on wireless communication systems. In a second scenario, the information symbols are transmitted over a time-varying multipath channel, so that the impact of ambient noise is assessed for realistic deployment scenarios.

The impact of the ambient noise channel on the performance of a communication link is therefore evaluated and informed suggestions are provided to effectively mitigate the impact of ambient noise in an UWAC receiver. A portion of the work described in this chapter contain materials that were submitted in:

- A. Egbewande, et. al, "The Effect of Directional Noise on the Reliability of an Acoustic Receiver in Shallow Environments". In IEEE Journal of Oceanic Engineering (IEEE-OES), Submitted June 2021.

Other related work that have been presented at conferences include:

- Singh, S., Egbewande, A., Chalmers, A., Taylor, R., de Gooyer, J. and Bousquet, J.F., "A MIMO Underwater Acoustic Transmitter Implementation with Space-Time Block Coding" in 4th Underwater Acoustics Conference and Exhibition (UACE) 2019

- Egbewande, A. and Bousquet, J.F., 2017, November. "Measurement of a Space-time Noise Mitigation Technique". In Proceedings of the International Conference on Underwater Networks and Systems (pp. 1-2).

- Egbewande A, Bousquet JF. Optimum space-time filter performance using a realistic noise model of the ambient environment. InUnderwater Acoustic Conference and Exhibition series, Skiathos, Greece 2017 (pp. 911-916).

1.5 Outline of Dissertation

The rest of this dissertation is organized as follows:

In Chapter 2, a more detailed review of the UWA system development is provided. Hence, key concepts that are used in the technical development of this work are also introduced to provide the reader an understanding of the topics discussed in this work.

In Chapter 3, the algorithms that estimate the position of a vessel using acoustic arrays are described. The algorithms rely on; 1) an optimum beamformer to estimate the bearing of the vessel; 2) a coherence-based MFP to estimate the range and depth of the vessel; and 3) a Kalman filter to remove the effect of estimation noise in both bearing and range. The measured acoustic position is also compared with the reported satellite data on the vessel.

In Chapter 4, two noise models are presented whose spatial properties rely on the directionality function and the coherence of the noise fields. The spectral characteristics are also derived from well-known analytical equations. The spatial and the spectral properties of the noise models are also validated against measured OAN.

In Chapter 5, a simple space-time receiver is developed to demonstrate the impact of naturally ambient noise on the acoustic link. For this purpose, a baseband information signal is processed in the presence of measured ambient noise. The receiver performance characterized by the BER is compared with that of the signal processed in the presence of the synthetic noise process.

Finally, a summary of the findings and suggestions for future work is provided in Chapter 6.

Chapter 2

Impairments in the Underwater Acoustic Channel

In this chapter, the fundamental impairments in the underwater acoustic propagation media are described. First, in Section 2.1, the physics of the acoustic waveguide is briefly introduced. Second, in Section 2.2, the factors that impact acoustic wave propagation in an underwater environment are reviewed. Then in Section 2.3, a channel profile obtained from an ocean experiment is used to depict the typical factors that contribute to channel impairments in UWAC. Finally, in Section 2.4 a succinct description is provided for the linear model typically used to represent the UWAC system.

2.1 The Acoustic Waveguide

The ocean is an acoustic waveguide bounded by the sea surface and the seafloor. Sounds radiated by an acoustic source (located at z_s) interacts with both the surface and the seafloor before arriving at receivers (located at z_1 and z_2) as shown in Fig. 2.2. Models are developed to characterize the way acoustics waves interact with these boundaries. Modeling acoustic waveguides serves to reliably predict the propagation channel in an underwater communication link. It can also be used, for example, in target tracking and other localization applications [**?**], since the waveguide models make it possible to localize the acoustic sources.

In acoustic modeling, the sea surface can be considered to be a simple horizontal boundary often viewed as a nearly perfect reflector. The exception are cases such as in the Arctic, where the ice cover at the surface is an elastic medium which couples with and affects the acoustic propagation [6]. On the other hand, the seafloor is a lossy boundary with varying topography throughout the seafloor. Both boundaries have small-scale roughness associated with them, e.g. surface gravity waves, which causes scattering and attenuation of sound. The scattering on the seafloor depends on the sediment type which could be a mixture of different elements – ranging from silt

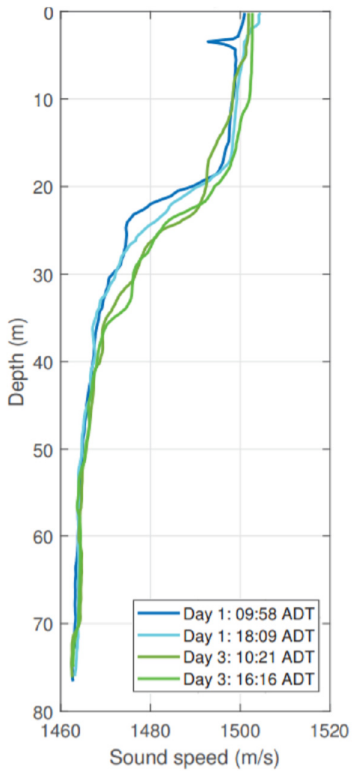

Figure 2.1: Sound speed profile computed from an acoustic measurement in July 2017.

to rocky sand, and of different particle sizes [**?**] with varying reflection characteristics in different locations. These factors make the seafloor a more complex boundary, and introduces difficulties in modelling the ocean acoustic waveguide for different geographical locations.

The variability in the sound speed as a function of depth is also a major factor in the propagation of sound in the acoustic waveguide. Fig. 2.1 represents the SSP obtained from a sea experiment that was run in 2017. This result is referenced simply to depict the variability in the SSP as a function of depth. It is shown that the sound speed fluctuates the most near the surface boundary largely due to the daily heating and cooling, precipitation, mixed layer temperature due to wind, salinity and depth [6]. Hence, the SSP of a measurement environment depends on the column depth and the measurement location. For instance, for the same column depths, the SSP is different in the polar region compared to locations closer to the equator.

Although the general ocean-acoustic propagation involves the interaction of the

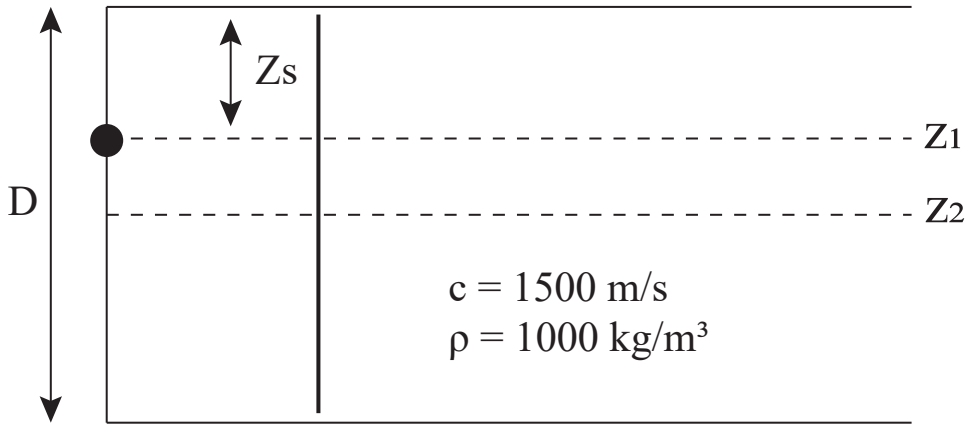

Figure 2.2: Ideal isovelocity ocean waveguide with pressure-release surface and bottom.

signals with the sea surface and sea bottom boundaries, the ideal waveguide is often well suited to illustrate the basic waveguide phenomena associated with the ocean acoustic propagation. The ideal waveguide is a range-independent, isovelocity (depth-independent) water column with perfectly reflecting boundaries as depicted in Fig. 2.2. The waveguides are easily characterized by simple models due to the homogeneity of the water column and a uniform sound speed with depth. However, heterogeneous waveguides with layered media i.e. varying sound speed and density, require more complex models to model the acoustic wave propagation. The choice of a waveguide model depends on the column depth, associated boundaries and the radiation conditions [6]. These factors in turn importantly determine the accuracy of a source-sensing/localization algorithm or the reliability of signal detection in a communication system.

Although it remains a difficult task to model the acoustic waveguide to perfectly match the actual deployment environment, several methodologies have been developed over the years to optimize both the boundary parameters and the computational time of the models [6].

Waveguide modeling characterized by the interaction of acoustic pressure at the surface and seafloor remains the central principle to achieve reliable communication

links in UWAC systems design. It is also the foundation for acoustic source sensing/tracking. The principle of signal interaction in the acoustic waveguide is applied in the source ranging algorithm described in Chapter 3 to estimate the position of a vessel.

2.2 The Underwater Acoustics Propagation Channel

In underwater acoustic communication, similar to the terrestrial network, the physical layer of the communication stack is responsible for encoding and decoding of information signals to achieve reliable data transmission and reception between communication devices. The efficient design of UWAC systems must mitigate the sources of distortion in the acoustic channel. As such, pre-coding can be done at the transmitter, and equalization can be realized at the receiver. In an UWAC channel, the information signal suffers from degradation due to transmission loss, intersymbol interference due to multipath, spatial and temporal variability of the channel as well as ambient noise [1].

Transmission loss is measured as the sum of losses due to geometrical spreading and attenuation. The spreading loss is a measure of the weakened signal as it propagates away from the source. Attenuation on the other hand, is a measure of the part of the acoustic energy that is absorbed (i.e. transformed into heat) or scattered due to different in-homogeneous factors such as dependence on temperature, pressure, salinity, and acidity (pH value). Salinity and temperature variations as a function of depth also determine the sound speed as a function of depth. This phenomenon is more pronounced in deep water columns but is less of a problem in shallow environments where the sound speed is of a relatively uniform value of approximately $1500m/s$ depending on the measurement site.

Spatial and temporal variability in the acoustic channel are primarily due to the interaction of acoustic waves in the propagation waveguide as well as platform motion. In the acoustic waveguide, sound waves reflection from the surface is worsened by surface motion which in turn causes wave bending.

Noise in the ocean are primarily characterized by the sources that produce them. These sources – either man-made and/or artificial contribute to the overall noise level in the ocean. Thus, the reliable detection of a communication signal relies on the sea

state which is also characterized by the ambient noise sources present during the signal transmission.

It has been demonstrated that transmission loss and noise determine the available bandwidth, propagation range and the signal-to-noise-ratio [**?**]. The time-varying multipath determines the signal design and the processing techniques adopted [**?**, **?**]. Furthermore, spatial variability due to the propagation waveguide and platform motion influences the signal design and the receiver structure that optimizes coherent signal detection [**?**]. Both spatial and temporal variability determine the channel throughput and performance of the communication system. Summarily, the key factors that affect acoustic signal propagation underwater are multipath propagation, bandwidth limitations, Doppler spread, small scale space-time variations, and noise in the acoustic channel. These factors are reviewed next.

2.2.1 Multipath

As discussed earlier, acoustic propagation is prone to severe multipath bounces due to the wavefront being reflected from the surface and the bottom of the ocean, depending on the propagation environment. The multipath profile of an acoustic channel is different in deep and shallow water. It also depends on the communication range, column depth and deployment depths of the transmitter and receiver nodes. Although boundary reflections due to both surface and bottom are not as pronounced in deep water columns, ray bending due to variations in the sound speed of water aggravates the channel distortion in deep columns. Also, due to the low sound speed (about 1500 m/s) of water, copies of the reflected paths of arrival could spread over hundreds of milliseconds, making the channel frequency-selective.

Many models have been presented to capture all these parameters in the acoustic multipath channel. However, in its simplest form, the acoustic channel can be modelled as an FIR filter

$$h(t) = \sum_{p} h_p(t - \tau_p), \tag{2.1}$$

where p is the path index, h_p is the signal amplitude of each propagation path, the path delay $\tau_p = l_p/c$, where l_p is the path length and c is the sound speed in water.

The multipath power delay profile (often referred to as the multipath profile) of a propagation environment is determined by the number of paths with significant amplitudes and the delay between successive paths. For instance, for a transmitter and receiver separated by distance r, at nominal depths d_1 and d_2, the time difference in the surface-reflected paths due to waves (or wind) is [**?**]

$$l(t) \approx l_0 + 2\Delta h(t)\cos\theta_0 = l_0 + \Delta l(t), \tag{2.2}$$

where l_0 is the nominal path length, θ_0 is the nominal angle of incidence. Due to the difference in path lengths, the signal component which is generalized as $A\cos\omega t$ (where A and ω are the signal amplitude and frequency, respectively) at the receiver, appears to be phase-modulated by a waveform

$$\Delta\psi(t) = \frac{\omega}{c}\Delta l(t). \tag{2.3}$$

The bandwidth of the received phase-modulated signal is

$$B - w = 2f_w(1 + \Delta\psi), \tag{2.4}$$

where $\Delta\psi_m$ is the modulation index.

The *mean excess delay*, *rms delay spread*, and *excess delay spread* are multipath channel parameters that can be estimated from a given multipath profile. The rms delay spread and mean excess delay are estimated from the temporal or spatial average of consecutive impulse responses collected and averaged over a local area. Also, several measurements obtained from many local areas (i.e. large-scale area) determine the statistical range of the multipath channel parameters which can be used in the design of the UWAC system.

At the receiver, copies of the signals from each propagation path are incoherently received due to different path delays causing ISI. To reliably receive the transmitted signal at the receiver, the goal is to coherently sum up these multiple paths. The multipath bounces also vary as a function of time and even spatially. Hence, signal processing techniques are developed at the receiver to predict the multipath profile and track the changes in the channel characteristics.

One other key challenge with signal propagation in UWAC is that the multipath

profile is significantly determined by the column depth and the type of sediment at the seabed. For instance, hard sediments such as rocks and gravel reflect sounds differently from silt and clay [**?**, 7].

2.2.2 Small-scale Variations

In UWAC (or any wireless communication) systems, fluctuations in the received signal due to small-scale and large-scale variations in the multipath propagation channel are an inherent challenge in reliably detecting the signal at the receiver. Small-scale variations are largely associated with changes in the propagation medium and the relative motion between the transmitter and the receiver. Historically, these variations have been perceived as a problem. Recently, to mitigate this pheneomena, the development of channel-dependent scheduling, wherein signal transmission takes place when the channel conditions are favorable, have been applied in long-term evolution (LTE) networks and in the emerging 5G new-radio (NR) networks [**?**].

Specifically, in shallow acoustic environments, the small-scale variations are attributed to surface scattering due to waves. In deep water columns, surface scattering compounded by internal waves along each deterministic path, contribute to the small-scale time variations [6]. Surface scattering is caused by wind-driven waves displacing the reflection points of the propagation paths at the surface, resulting in signal dispersion. Internal waves (otherwise called gravity waves), on the other hand, are caused by a stratified column as the water density changes with depth due to changes in temperature and/or salinity.

Generally, in wireless channels, the goal is to predict the multipath profile at the receiver by developing statistical models that capture the time-varying profile of the channel. There are several models available to characterize the channel probability distribution in radio channels, and in [**?**] a model has been developed to account for the different time constants associated with different phenomena, including the surface roughness, inherent motion of nodes affected by currents, and mobility of underwater vessels. Studies have demonstrated that the mean channel amplitude as a function of depth can follow a log-normal distribution [**?**]. This is attributed to the reverberation, which causes caustics in the ocean. Additionally, experimental results showed that the amplitude for the different tap delays can exhibit Rician [**?**] or Rayleigh fading [8].

Recall that channel profiles with a dominant path of arrival (i.e. line-of-sight) are characterized by Rician distribution, while Rayleigh distribution describes channel with no dominant paths [9].

2.2.3 Bandwidth

Communication between acoustic devices is determined by the allocation of an operational bandwidth on which the information signals are transmitted and received by the receiver. The factors that determine the operational bandwidth of an acoustic link are transmission loss, spatial variability and noise (discussed later in this section).

Transmission loss as discussed earlier, is caused by geometrical spreading and attenuation (due to absorption loss). Transmission loss increases with range and frequency, limiting the useful bandwidth in acoustic propagation to the lower frequencies. Spatial variability is caused as a consequence of shadow zones in the acoustic waveguide [1].

The frequency-dependent transmission loss and noise determine the bandwidth, achievable range and the signal-to-noise ratio (SNR) measured at the receiver. Both factors also determine the carrier frequency. Often, the transmission bandwidth is at least 10% of the carrier frequency. This in turn implies that acoustic communication links are more than often wideband and susceptible to multipath reflections. Bandwidth limitation is a key consideration in the design of UWAC systems. It determines the maximum achievable range and in fact the data-rate of an acoustic link.

Further, the bandwidth of the channel can be quantified by the coherence bandwidth which in turn is related to the multipath profile of the channel. Hence, the coherence bandwidth of the channel is described in this section.

Coherence Bandwidth

The received signal amplitudes from the multipath profile as shown in (2.1) yield copies of the transmit signal that are spread out in time. In the frequency domain, the multipath induces a variation of the channel amplitude as a function of frequency. The coherence bandwidth is the measure of the maximum frequency difference for which signal amplitudes are still strongly correlated [9]. Hence, coherence bandwidth is used to characterize the channel in the frequency domain, which is analogous to

delay spread in the time domain. It is a statistical measure of the frequencies over which the channel is considered to be flat i.e. all the spectral components passes with approximately equal gain and linear phase. Implicitly, this implies that two signals with frequency separation greater than the coherence bandwidth are affected differently by the channel.

Generally, in wireless communication, the coherence bandwidth, expressed as

$$B_c \approx \frac{1}{5\sigma_t}, \tag{2.5}$$

is defined as the bandwidth over which the frequency correlation is above 0.9, where σ_t is the r.m.s delay spread of the channel.

2.2.4 Doppler Spread

Doppler, is the change in frequency of a wave with respect to an observer who is moving relative to the source producing the wave. In wireless communications, Doppler is caused by the relative motion between a transmitter and a receiver resulting in the received signal being shifted in frequency. The low sound speed in water aggravates the Doppler effect in acoustic propagation, making it one of the most challenging medium for communication. Also, wind-driven waves displacing signals at the surface of the ocean causes a relative motion in the reflected points. The non-coherent combination of the signals at the receiver sensor results in frequency spreading of the surface-reflected signals, leading to the concept of *Doppler spreading*.

The Doppler spread caused by a surface reflected path at a discrete frequency f_0 can be expressed as [9]

$$f' = 0.0175(f_0/c)w^{3/2}\cos\psi, \tag{2.6}$$

where ψ is the incidence angle and w is the wind speed in m/s. From (2.6), higher Doppler spreads are expected at higher frequencies (which is typical for short-range communication links), while lower Doppler spreads are expected at lower frequencies (i.e. for long-range links).

In the time domain, the coherence time is used to characterize the time-varying nature of the frequency dispersion in the channel. Hence, coherence time is a measure

of duration over which the CIR is invariant. This also implies the duration over which two received signals have a strong potential for amplitude correlation. Coherence time is defined by

$$T_c = \sqrt{\frac{9}{16\pi f_m^2}}, \tag{2.7}$$

where $f_m = c/\lambda$ is the maximum Doppler shift.

2.2.5 Acoustic Ocean Ambient Noise

Noise in the ocean is ubiquitous – caused by both man-made (anthropogenic) and naturally occurring sources. The natural sources can be grouped into sources due to surface waves and precipitation, and impulsive noise due to marine life. The anthropogenic sources are due to man-made activities, such as shipping and pile-driving. Ambient noise sources due to shipping is dominant in frequencies between 10 Hz to 500 Hz, while surface agitation is dominant between 1 kHz to 10 kHz, and the impulsive sources (due to marine mammals and anthropogenic activities) are dominant in frequencies between (10 Hz - 100kHz) [**?**]. Sonar systems designed for UWAC systems operating in these bands are susceptible to these noise sources, further limiting the available operational bandwidth.

The unique attributes of OAN, referred to as noise in this study, are well known in literature. Some of these attributes are discussed next.

Directionality

It is well established that ambient noise sources are directional in their propagation. In fact, modeling ocean noise often relies on the directionality of the noise field. For instance, the characterization of surface generated noise [4, 5], shipping noise [**?**], and impulsive noise produced by marine mammals [**?**] are all founded in the directional propagation of the sources that produce them. The directional noise characteristics in deep and shallow water environments are described in [5, 4, 1, 6, 10], and several related models have been developed for ocean noise. OAN is known to be directional, producing spatially correlated samples when measured at spatially separated hydrophones. This property distinguishes ocean noise from the standard

white Gaussian noise samples.

Coherence

The coherence property of noise relies on the correlation of the noise samples at spatially separated sensors. The coherence can serve to evaluate the degree of resemblance for the noise field received at any two spatially separated sensors, and it is a representation of the squared magnitude of the phase shift in the measured noise fields at these spatial sensors.

Cox in [4] derived the integral expression for two vertically aligned sensors $\{x, y\}$, separated by distance d in a spatially homogeneous ambient noise field, by relating the spatial coherence function with the directionality of the noise fields by

$$\Gamma_{yz} = \frac{1}{2}\int_0^{\pi} F(\theta) e^{i\omega\tau_d \cos\theta} \sin\theta d\theta, \tag{2.8}$$

where $i = \sqrt{-1}$, θ is the polar angle measured from the zenith, $c = 1500m/s$ is the sound speed and $\tau_d = \frac{d}{c}$ is the time difference of signal replicas measured at the sensors. The directionality function $F(\theta)$ represents the noise power integrated over all the azimuthal angles. Thus, from (2.8), the coherence measured at any pair of hydrophones is uniquely related to the directionality function of the noise fields.

It is also well established that the coherence measured at any pair of spatially separated sensors depends on the orientation of the receiver. For instance, in [5], it was demonstrated that the spatial coherence measured at a horizontal pair of sensors (separated by an angle $\gamma = 0$) decays faster than that of vertical pairs (i.e. $\gamma = 90$) in an infinitely deep ocean. This is observed in Fig.2.3 where the spatial coherence decays rapidly beyond the first zero in the horizontal array than in the vertical pairs.

Hence, in applications that rely on the measure of the spatial coherence to estimate different oceanic parameters, vertical arrays are often preferred to horizontal arrays. The coherence measured at a VLA is discussed in greater details in chapter 3.

Power Spectral Density

The spectral characteristics of ocean noise have been well defined [1]. The major components are turbulence, shipping, wind and thermal noise. Each component is

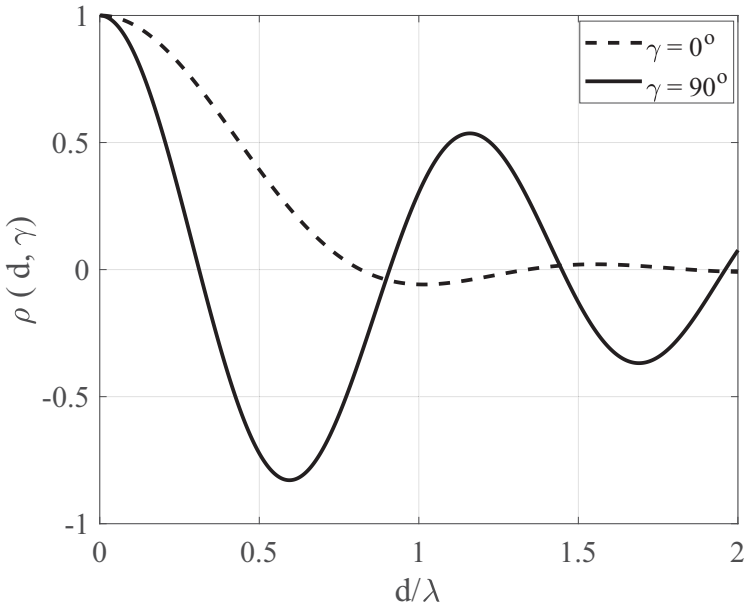

Figure 2.3: Effect of receiver orientation on the spatial coherence of surface noise fields for the case of directional noise sources.

dominant at different portions of the frequency spectrum as discussed earlier. The analytical expressions for the PSD (in dB re μPa) of the different components of ambient noise are

$$\begin{aligned} N_t(f) &= 17 - 30\log f \\ N_s(f) &= 40 + 20(s-0.5) + 26\log f - 60\log(f+0.03) \\ N_w(f) &= 50 + 7.5w^{(1/2)} + 20\log f - 40\log(f+0.4) \\ N_{th}(f) &= -15 + 20\log f, \end{aligned} \tag{2.9}$$

where f denotes frequency in kHz, and $\{N_t, N_s, N_w, N_{th}\}$ represent sources due to turbulence, shipping, wind and thermal noise, respectively. The total noise PSD (in dB re μPa) measured at sensor y for a given frequency f $[kHz]$ is therefore

$$S_{yy} = N_t(f) + N_s(f) + N_w(f) + N_{th}(f). \tag{2.10}$$

Fig. 2.4 shows the ambient noise PSDs for shipping activities and with wind

speeds up to 10 m/sec (19.4 knots) obtained from (2.9). It is observed that each noise source is dominant in bandwidths up to 10 kHz. Turbulence noise is dominant in the frequency band 0.1 $Hz - 10$ Hz, while shipping activities are the major factors contributing to noise in the frequency region 10 $Hz - 1$ kHz, although propagation effects (e.g. high frequency absorption, or mode stripping in shallow water environments) can modify the shipping noise signature that arrives at the sensor. Shipping activities are usually weighted by a factor s which is a value between 0 and 1 representing low and high shipping activity, respectively. Surface agitation due to wind (where w is the wind speed in m/s) is dominant between 1 kHz to 10 kHz. Moreover, impulsive sources (due to marine mammals and anthropogenic activities) have also been showed to be dominant in frequencies between (10 Hz - 50 kHz) [1].

Although the spectrum of the ambient noise channel is often approximated as white noise in UWAC systems, in practice it is indeed colored exhibiting a decaying PSD with a rate of $\approx$ 18dB/decade as demonstrated by the inverse frequency $(1/f)$ in Fig. 2.4. This implies that the ocean column acts as a low-pass filter to yield an ambient noise process. Thus, the ambient noise PSD is usually considered as a $1/f^n$ spectrum i.e. noise has more power at lower frequencies than at the higher frequencies [8]. Coincidentally, sonar systems designed for UWAC systems operating in these bands are susceptible to these noise sources, further limiting the operational bandwidth.

Generally, it is more challenging to model or predict noise in shallow water than in deep water columns, due to variability in both space and time primarily owing to bottom interactions. Typically, shallow water environments are approximately about 200 meters, while deep columns are in excess of 2000 meters. Ambient noise in shallow environments are classified into sources due to wind, shipping activities and biological noise mostly due to snapping shrimp. It is also noteworthy that ambient noise power decreases with depth with about 9dB higher noise levels in shallow water compared to deep environments [**?**].

The properties of OAN are not only limited to the spatial and spectral domains. In fact, other statistical properties such as the autocorrelation, probability distribution and linearity of OAN are also quite unique to the sources that produce them. To analyze the distribution and linearity of OAN, it is commonplace to apply bi-spectral

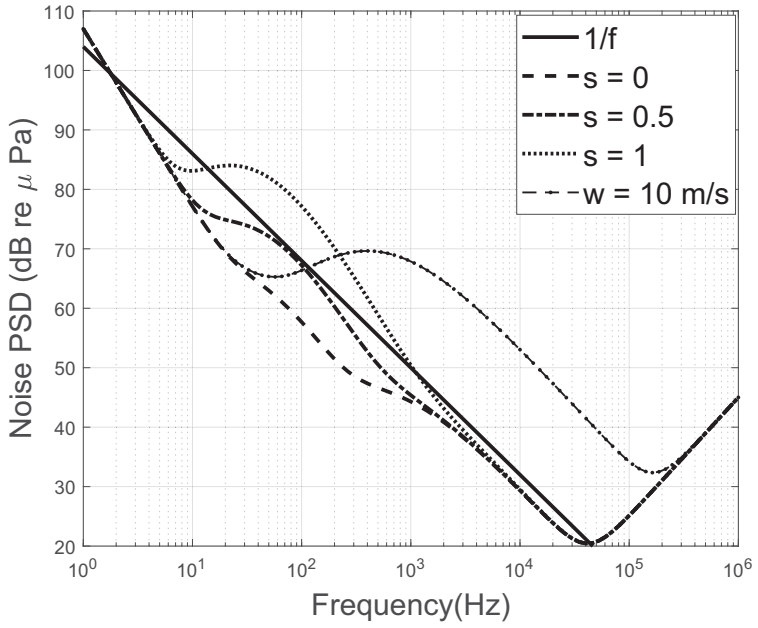

Figure 2.4: Power spectral density of the ambient noise level in dB re μPa/Hz for wind speed 10 m/s (19.4 knots) and different shipping noise is presented for high (s=1), moderate (s=0.5), light (s=0) shipping activities.

analysis in literature. For instance, a classical example is in [11], in which the author developed a statistical method for testing whether OAN has a Gaussian distribution and that it contains evidence of nonlinear components in the different noise sources observed from various ocean experiments. Often, these statistical properties of OAN are demonstrated by observing windows of the noise time series to establish duration limits over which certain distributions and linear properties of OAN are valid. The work developed in this dissertation excludes these statistical analyses, but are highly recommended for future studies on the modeling of OAN.

To summarize in this section, the unique properties of ambient noise are defined by its directionality, coherence and frequency-dependent spectrum. These properties have been proven to be useful in localizing shipping vessels or quantifying shipping activity [**?**, **?**, **?**], and monitoring wind speed and rainfall levels [12, 13, 14]. In other applications, the inversion of OAN can be used to obtain information about the seabed [**?**, **?**], bathymetry [**?**, **?**] and the water column [**?**, **?**]. This is because ambient noise has a spatial signature that depends on the ocean environment, while

its PSD is frequency-dependent even over a relatively narrow bandwidth (discussed in chapter 4), and depends on the nature and density of the sources present. However, these unique properties are often ignored in the design of an UWAC receiver where the noise is often assumed to be uncorrelated white Gaussian samples [**?**, **?**].

These key factors – multipath propagation, bandwidth limitations, Doppler spread, small scale space-time variations, and noise in the acoustic channel distort acoustic signal propagation underwater. Often, these factors are characterized by mathematical models which can be developed for computer simulations so that the performance of the communication system can be characterized in controlled conditions. In other scenarios, the values for these channel distortion parameters are obtained experimentally. The latter is often applied in UWAC, whereby through post-processing acoustic signals, the channel parameters in a specific area can be calculated.

Some results from an ocean experiment are described in Section 2.3 to depict a typical experiment where the channel parameters are computed from post-processed data transmission.

2.3 Characterization of the Multipath Channel

In this section, the CIR from an ocean experiment is shown as a function of time. The objective of this section is to simply show some of the sources of distortion in an UWA channel as earlier discussed. Hence, the details of the experimental setup is not discussed in this section, but the experiment (DalComm1) is revisited in Chapter 4.

In the results shown in this section, acoustic waveforms are transmitted by a single transmitter, while the waveform is received by a five-element hydrophone array. The transmit acoustic waveform shown in this section is a maximum length (ML) sequence used in spread-spectrum communication. The ML-sequence consists of 512 bits and is transmitted at a rate of $R_b = 240$ symbols per second so that the channel can be characterized for a maximum excess delay of 2.1 seconds and a processing gain of 24 dB.

The CIR of the ML-sequence is shown in Fig. 2.5 for the different measurement ranges – 1 km, 2 km, 4 km, 8 km, and 10 km. It is observed that the overall CIR measured at the hydrophones are similar over long-term except at the first hydrophone. During this sea trial, the sea state was relatively high – between 2 and 2.5, so that even

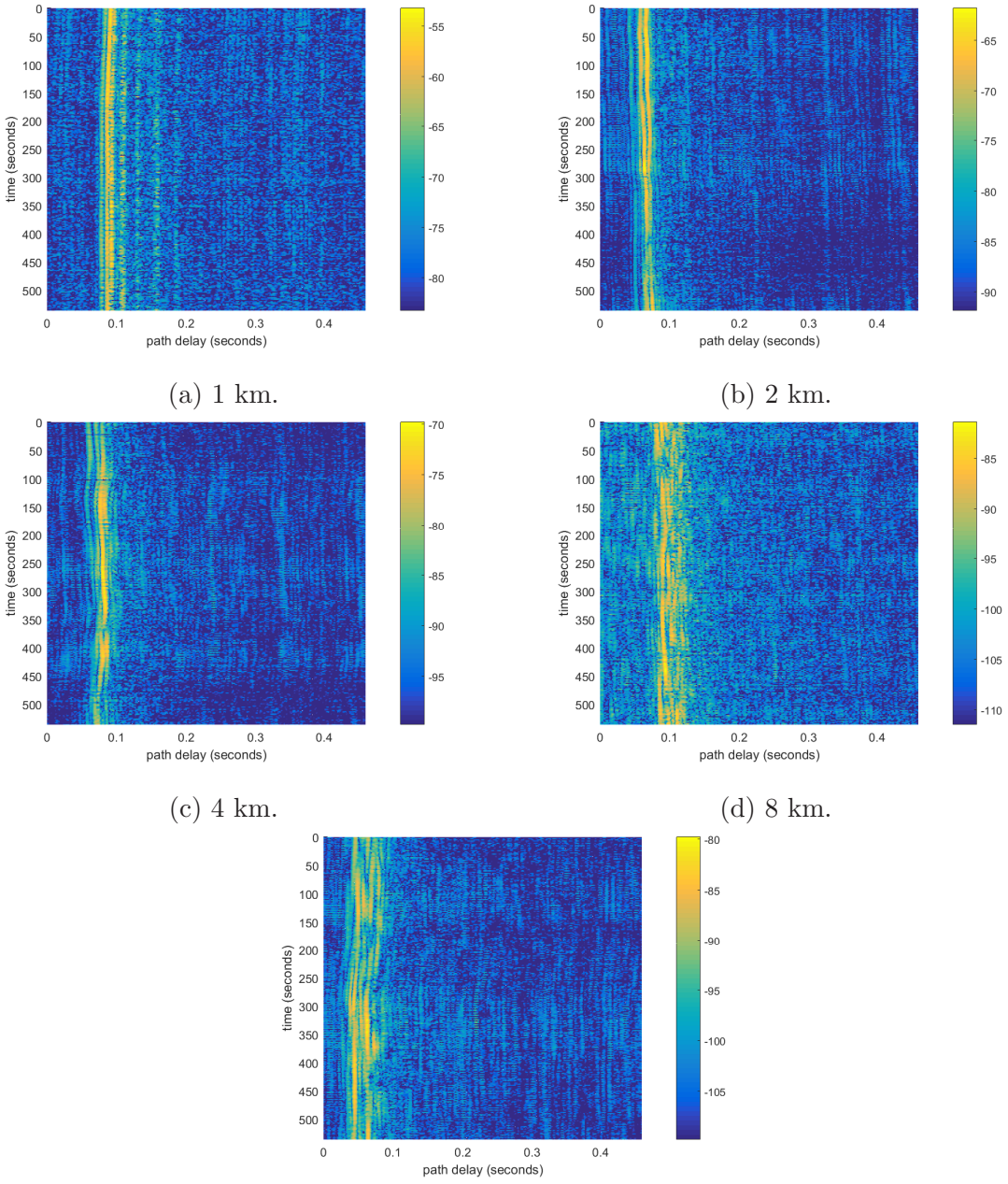

(a) 1 km.

(b) 2 km.

(c) 4 km.

(d) 8 km.

(e) 10 km.

Figure 2.5: Channel impulse response in dB as a function of time measured using M-sequence on hydrophone 1.

though the deployment vessel was anchored, it was drifting through the experiments. It can also be observed that as the distance between the transmitter and receiver increases, the multipath echo arrival becomes more diffused while the significant path arrival delay is more spread.

To further investigate the CIR, a single channel profile is also represented in Fig. 2.6. A close observation of the CIRs shows that for ranges at 2 km and 10 km, the channel delay is similar. Likewise, the channel profiles over the rest of the measurement ranges are similar.

Further, the Doppler spread measured for all the transmission ranges are shown in Fig. 2.7. The results show that the maximum Doppler spread observed in the 2 km range is about 0.14 Hz. Recall that the coherence time T_c can be obtained from (2.7), so that the average coherence time of the channel is about 3 seconds.

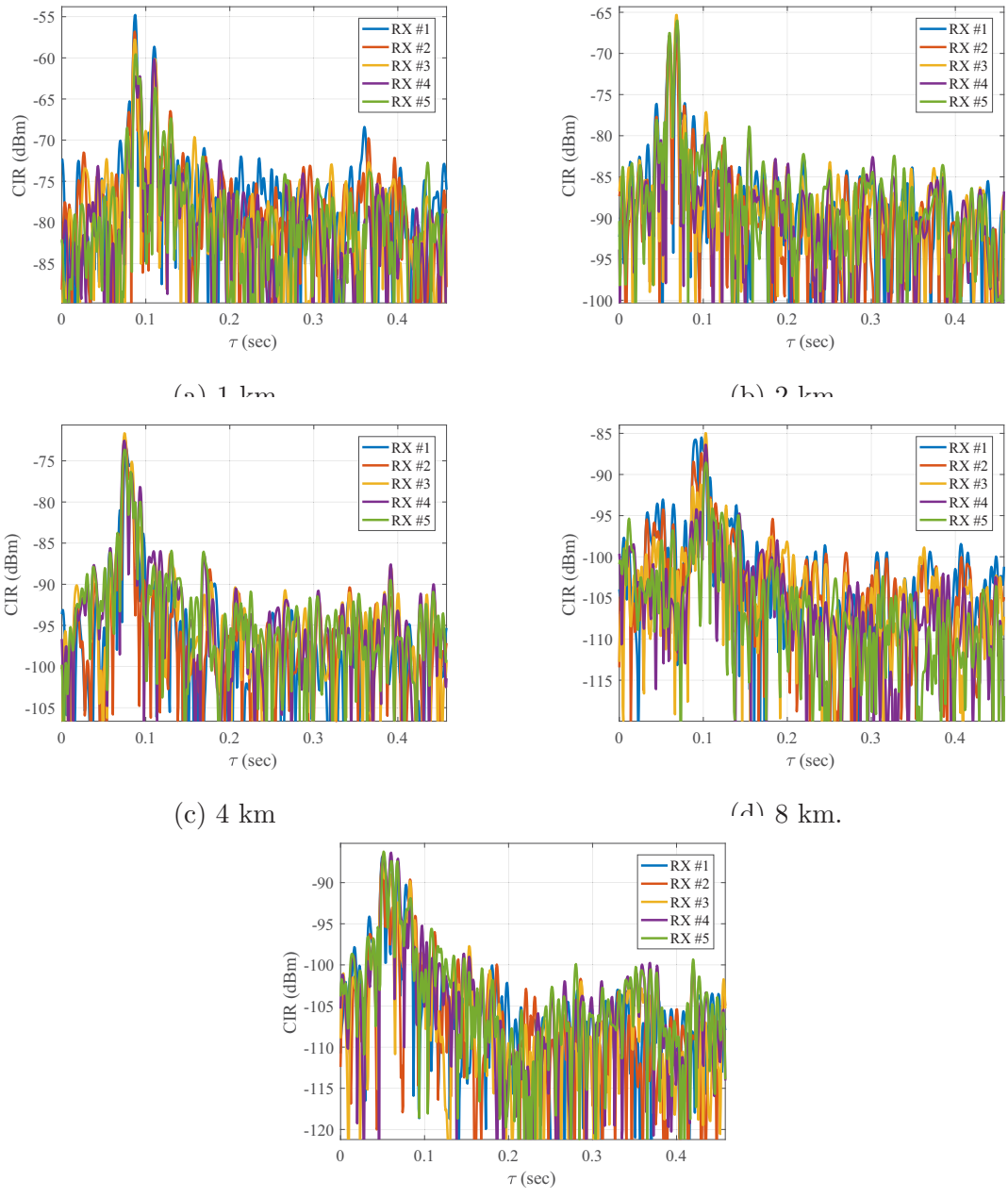

(a) 1 km

(b) 2 km

(c) 4 km

(d) 8 km.

(e) 10 km.

Figure 2.6: Example of channel impulse response profile in dB using ML-sequence.

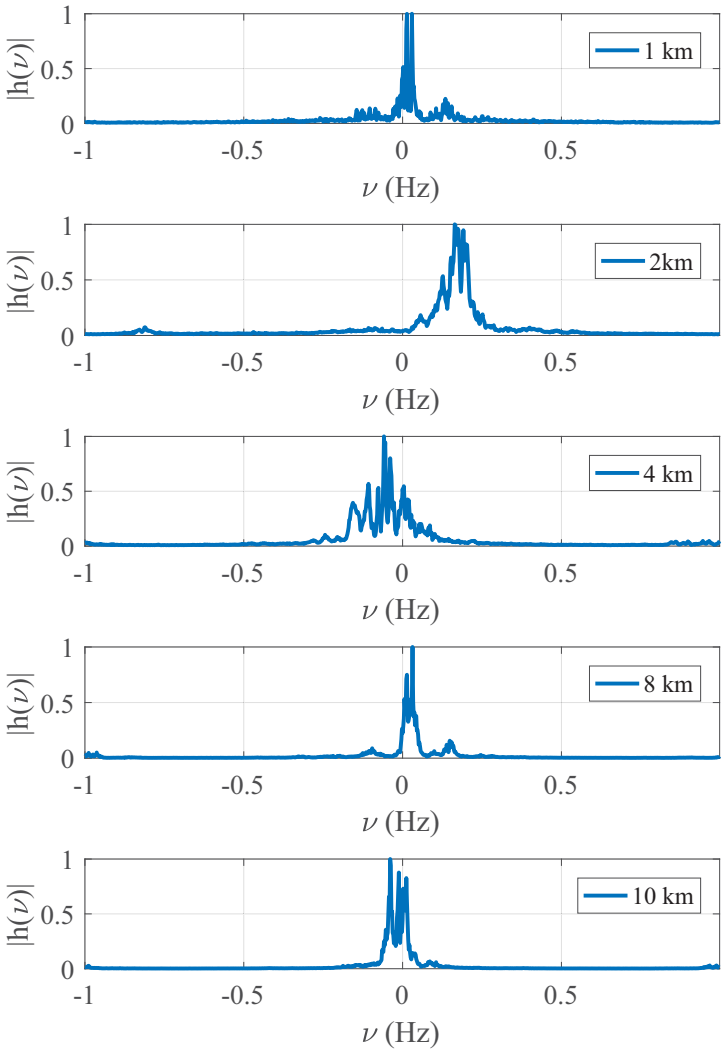

Figure 2.7: Doppler spread for all ranges

2.4 Model of a Space-time Linear System

It is quite usual to model the channel CIR as a linear system described in (2.1). This makes it possible to also model the signal $x(t)$ measured at the receiver by a linear model [15]

$$x(t) = s(t) \circledast h(\tau, t) + n(t) \tag{2.11}$$

where $s(t)$ is the information signal that contains the modulated symbols, convolved (or multiplied in the frequency domain) with the CIR $h(\tau, t)$, and $n(t)$ is the additive noise (as in Fig. 1.1). Eq.(2.11) can be extended for a multi-element receiver array, in which case $\mathbf{s}(t), \mathbf{h}(\tau, t),$ and $\mathbf{n}(t)$ are the information signal, CIR and noise measured at all the elements of the array, where the boldface notation depicts the combined vector of values spatially sampled at an array of sensors.

In RF communications, the noise is characterized by Gaussian distribution whose derived samples are uncorrelated and has a flat frequency spectrum. However, the attributes of OAN described thus far in this chapter do not compare with noise in RF. At the receiver, mitigating the impact of both the multipath channel and the noise are equally important to be able to reliably detect the transmit information signal.

Summarily, in this chapter, the high-level description of the acoustic waveguide and the factors that impact the propagation of sounds in an UWAC systems have been introduced. Chapter 3 focuses on the space-time directional properties of vessel noise. Chapter 4 discuses the directionality properties of ambient noise used for generating synthetic noise at an acoustic array. Finally, the impact of ambient noise as well as the multipath propagation is quantified on an adaptive space-time equalizer in Chapter 5.

Chapter 3

Space-time Directionality of Shipping Noise

3.1 Background

In this chapter, the time varying characteristics of the directionality of OAN is demonstrated. To this end, the unique space-time signature of vessel noise is demonstrated through acoustic source tracking.

The justification for the system design in this chapter is in two folds. First, the system is designed in response to the need of Jasco Applied Sciences for a covert system that relies on acoustic technology to track the position of a vessel over a long range. Second, the system provides insights into the time-varying directional property of vessel noise which is a significant contribution to the ability to mitigate shipping noise sources in an UWAC.

To achieve these objectives, first, a ML-BF is applied to estimate the directionality (hereafter interchangeably referred to as bearing) of the noise produced by a vessel's propeller, measured at a compact array of hydrophones. Second, a MFP technique is applied to estimate the range of the vessel to the array. Third, estimates of the bearing and range of the vessel are applied to compute the position of the vessel to the compact array.

The novelty in this chapter lies in the system level design which is derived from algorithms that have been applied for other solutions in the past. The ML-BF is a well-known solution for resolving the angle of arrival of signals while the MFP is a well-known solution in source localization. However, these algorithms are integrated together to achieve an efficient system that is able to track the bearing and range of a vessel. The system is developed as a proof of concept and suggestions are provided on how the system can be implemented and optimized for real-time deployments.

Therefore, Section 3.2 reviews the evolution of the technologies that have been used for vessel tracking applications over the years. The section also discusses the ongoing challenges in vessel tracking applications and proposes a system design in

response to some of these challenges. In Section 3.3, the noise measurement scenarios that are used in this chapter are described. In Section 3.4, the concept and design strategy in acoustic source tracking is introduced. In Section 3.5, a ML-BF that achieves the lowest possible variance of a linear TDOA estimator specified by the Cramér-Rao lower bounds is developed to estimate the optimum bearings of the vessel with respect to time. In Section 3.6, a type of MFP that relies on the estimate of the spatial coherence of the measured signal is developed for source depth and range estimation. Finally, in 3.7, a Kalman filter that removes the estimation noise from the computed bearing and range is presented along with a methodology that validates the estimates of the vessel's position as a function of time against the AIS data reported on the same vessel.

3.2 State-of-the-art in vessel tracking

Monitoring the location of vessels in the open ocean has been achieved mainly by using a line-of-sight communication e.g. AIS, Global System for Mobile Communications (GSM), WIFI; or maritime mobile satellite communication (e.g. Inmarsat, Iridium, VSAT) [**?**, **?**, **?**, **?**]; or a combination of these systems. Other systems rely on video detection of the vessel to estimate its position [**?**, **?**, **?**]. The AIS and GPS rely on the transponder on board the vessels to update the vessel's position and have been used extensively over the years and for different fleet tracking needs. Other systems that rely on video detection are prone to failure in inclement weather conditions and sea-state, thus limiting the scope of their applications [**?**, **?**].

Overall, there are challenges involved with having a homogeneous system that works in varying environmental conditions, for different kinds of vessels - ranging from kayaks to commercial vessels, and that would not totally rely on the discretion of the sailors to turn on an on-board transponders. These challenges have been identified by several ocean stakeholders and has led to standardized requirements for monitoring marine traffic over the decades.

Since 2002, the International Maritime Organization (IMO) has made it compulsory for all passenger vessels as well as all commercial vessels over a certain size to carry an AIS transponder[**?**]. Since then, the AIS has become ubiquitous in the marine industry. The AIS was introduced for three applications: 1) as a ship-to-ship

system for collision avoidance; 2) ship-to-shore technology for littoral States/regions to obtain information about a ship or cargo; and 3) operation of Vessel Traffic Services (VTS) management that controls and monitors maritime traffic [**?**]. Port authorities and other land-based ocean stakeholders are equipped with receivers so that they can view the local traffic without the need to transmit any information from shore.

Since the early days of using the AIS, information such as position (in longitude and latitude), ID, speed, heading, cargo, destination, etc. were collected via on-board GPS and other navigation sensors and broadcast at intervals via a VHF radio transmitter. Marine traffic was accessible via these AIS transceivers that were limited to the VHF range [**?**], about 10–20 nautical miles. With the rise in the global number of ships and the increasing need to secure the oceans, the short-range capabilities of the VHF enabled transceivers were too limited relative the growth in the marine industry [**?**]. Space-based AIS that rely on satellite communication have been developed to improve detection probability for long-range applications [**?**] and have been used extensively for vessel monitoring applications.

In 2009, SpaceQuest launched AprizeSat-3 and AprizeSat-4 that rely on AIS receivers [**?**]. By 2010, these receivers were successfully able to receive a search and rescue transmission test by the U.S. Coast Guard. Also, in 2010, Canada announced a partnership arrangement whereby data from AprizeSat-3 and AprizeSat-4 would be incorporated into the exactEarth system and made available worldwide as part of their exactAIS service [**?**]. In 2010 the Norwegian AISSat-1 nano-satellite was successfully launched into polar orbit to improve surveillance of maritime activities in the North Sea [**?**]. Since 2010, satellite AIS systems have been fully operational at commercial capacities globally for monitoring ship traffic, but not without some identified challenges.

The technical challenges with receiving AIS messages in areas with high marine traffic density have been identified in literature [**?**]. Also, given that the AIS is a self-reporting system, there are concerns about its reliability [**?**] and susceptibility to human manipulations [**?**, **?**]. The challenges involved with AIS data reliability may be classified into three categories[**?**]: 1) erroneous messages due to the fact that some information (such as the name of the vessel and the vessel destination) are entered by the crew on-board the vessel; 2) AIS messages being spoofed; and 3) AIS transponders

being turned off to perform illegal activities. Although erroneous AIS messages could be due to inadvertent human errors, message spoofing and on-off switching are the more frequent attacks on AIS messages [?, ?]. Techniques and algorithms have been proposed in literature to identify intentional AIS on-off switching [?, ?].

Having identified the satellite-based AIS as the widely used technology for vessel monitoring, its inherent challenges and its propensity to attacks, the AIS also falls short in meeting the pertinent needs involved with protecting marine life in the oceans. With the evolving understanding of earth's oceans over the years, human activities - system deployment for ocean observatory purposes, as well as commercial and leisure vessels have significantly increased [?, ?]. The derived benefits from increased oceanic activities have not been without some adverse effects on the ocean ecosystem. For instance, it was showed in [?] that between 1950 and 2007, there has been a rise in the global number of ships by a factor of 3.5, with a 3.3dB increase in noise levels every decade, mostly due to increased shipping activities. It has also been established that vessel traffic is an ubiquitous anthropogenic source of ocean noise and with a high potential to harm marine life [?, ?, ?, ?, ?, ?]. Therefore, there has been many efforts by different research groups to assess and reduce the impact of vessel noise on marine life. For instance, the Enhancing Cetacean Habitat and Observation (ECHO) program by port Vancouver in Canada is aimed at developing measures that quantify and reduce the threats posed by vessel traffic and port activities on at-risk whales in the region [?, ?]. Many research and ocean observatory groups as well as port and marine conservation authorities have showed interest in systems that are able to effectively manage anthropogenic activities without destroying marine life [?, ?].

To address the challenge involved with the increase in human activities and the risk posed to marine species, passive arrays of hydrophones have been used extensively to localize whale calls and fish vocalization in the ocean [?, ?, ?, ?] with promising results. For instance, through the ongoing measures by the Canadian government to reduce the risks to North Atlantic right whales, arrays of hydrophones have been deployed to monitor whale aggregated areas and restriction measures on human activities have been implemented in these areas. To this effect, season-long fishing has been closed, speed limits are enforced on vessels and new gear marking requirements are enforced in these areas [?, ?]. Furthermore, the interfering noise emanating from vessels have

also been showed to not only impact the communication space for fish vocalization and marine mammals [**?**, **?**], but also deteriorates the ability to accurately localize and track these aquatic species [**?**] with acoustic arrays. Having been demonstrated that acoustic sensors can localize marine animals, it is desirable to simultaneously localize vessels especially in areas with high density marine life.

The system described in this chapter is proposed as a solution that can estimate the range of vessels over a few kilometer radius. The system design is proposed as a proof of concept to enhance ongoing efforts towards ship noise assessment and noise saving calculations associated with maintaining tolerable noise levels for marine life. The motivation behind the design strategy proposed in this chapter is provided in this section.

Design Motivation

Underwater acoustic localization techniques are classified into two main categories, namely; 1) range-based, and 2) range-free algorithms. Range-based algorithms first estimate the distance or the direction of arrival (DoA) of a source to a target. Various algorithms for computing the DoA rely on estimates of the angle of arrival (AoA), time difference of arrival (TDOA), frequency-difference of arrival (FDOA), or other similar associated techniques. Subsequently, estimates of these ranges are then converted into different coordinates using multi-lateration or triangulation methods. On the other hand, range-free algorithms rely on the knowledge of the local topology and the positional estimates of the deployed sensor nodes, using the knowledge of nearby anchor nodes [**?**]. Hence, the range-free techniques are often applied in underwater acoustic sensor networks, while the range-based techniques are applied for array-based localization techniques. The system development presented in this chapter relies on the use of acoustic arrays which in-turn confines the localization techniques to the range-based algorithms.

Sensor arrays are capable of obtaining directional beam pattern applied to the source signals measured at the array. Hence, signals propagating from a desired direction can be amplified while those from undesired directions are attenuated, yielding an overall improvement in the SNR or SINR. This concept defines the underlying principle in beamforming.

TDOA techniques have been applied even for localizing broadband acoustic sources [**?**, **?**]. TDOA techniques require accurate estimates of the relative time-delay between the array elements (or sensor nodes, as in acoustic sensor networks). Since, the energy of acoustic signals are range-dependent, TDOA algorithms need to be carefully implemented to achieve great accuracies. Owing to this, some authors have proposed energy-based acoustic source localization techniques [**?**].

Further, AOA techniques exploit the phase difference measured at the receive sensors [16, **?**, **?**] and is applicable when the acoustic source emits coherent signals. Several beamforming techniques have been developed to estimate the AoA. The directional sensitivity of the array beamforming algorithm produces beam patterns with defined structures, secondary beams, as well as sidelobes which are smaller in amplitude and do not correspond to any direction in which the array is focused. Inherently, sidelobes are a major challenge with beamforming and must be considered in the efficient design of the beamformer.

Once the AoA is known, the question then remains, how far is the source from the array. This is necessary so that the position of the source can be characterized accurately. Matched-field processing (discussed in greater details in Section 3.4) is another array processing technique used for estimating the range of the source. In this technique, replica fields are computed by solving the wave equation for a source placed in an arbitrary position in the water column. The results is then compared with the measured acoustic pressure, and the best fit for the source location is derived by a searching mechanism, which often rely on beamforming techniques. The major drawback of the MFP is to predict the exact model of the environment and to be able to generate a look-up table (LUT) of the replica signals. In fact, to address this problem, some authors have to derive features directly from the data to predict the model of the environment [**?**, **?**]. Another implicit challenge is with applying beamforming techniques as the searching mechanism in MFP. This also introduces sidelobes in the MFP techniques.

As in most navigation problems, uncertainties are introduced in the source estimates, making it more cumbersome to convert the source range and/or direction into other coordinates. For this reason, state-space filters are applied, in which the range

and direction of the source is characterized by state-space models [**?**, **?**]. A classical example of this class of models if the Kalman filter, which has been applied in MFP for acoustic solutions [**?**, **?**]. In MFP applications, it is often required that the estimates of the range and bearing of the source be first converted to the Cartesian coordinate before applying the Kalman filter.

Overall, the ML-BF is developed to realize an optimal beamformer that estimates the directionality, while the CB-MFP is developed as a processor that does not rely on a beamforming algorithm to estimate the source (vessel's) range. A more detailed comparison of the beamforming algorithms and the discussed in Section 3.4.3, while the rest of this chapter describes the building blocks in the vessel tracking system.

3.3 Experimental Set-up

Two different noise measurement scenarios used to characterize the vessel's position are described in this section. Acoustic ambient noise is recorded at each of these experiments and the analyses developed in this dissertation rely on these measured ambient noise.

In a first trial – the Shallow Water CANAPE – which was run from September 2016-2017, experiments were run north of Barrow, AK, between the Chukchi Sea and Beaufort Basin. CANAPE consisted of a deepwater experiment (DW CANAPE) with its site in the central Canadian Basin and a shallow-water experiment (hereafter referred to as CANAPE) with its site in the northeast Chukchi Shelf. Both experiments included acoustic sources and acoustic receivers. The objectives of the CANAPE experiments were 1) to receive and record signals to quantify shallow and deepwater propagation and its spatio-temporal variability, 2) to assess ambient noise on the shelf, investigate environmental measurements and inference, and 3) measure mid-frequency reverberation and propagation.

There were four recording stations each containing an eight-channel hydrophone array. The recording units utilized JASCO's AMAR recorder. The recorded data was sampled at 16 kHz. AMAR1 - the first recording station used in this work, had a VLA with 2.5 m spacing, incorporated with horizontal arms near its mid-section that convert it into a spatial array of a tetrahedral structure (as in Fig. 3.1), thus able to estimate compass bearings in addition to a vertical arrival angle. The array was

deployed with the center element at a depth of 125.25 meters, and in a water column of about 149 meters. The data recording during these experiments were separated in time to record ambient noise which are used in this work. Shipping noise sources detected during these measurements were used to characterize the algorithm for vessel localization and tracking. It is noteworthy that the post-processing of the sonars recorded during these experiments is exclusive to JASCO and are not included in this dissertation. Albeit, the presence of active sonars at frequencies higher than 640 Hz (as in Fig. 3.1) in these data set interfere with the accuracy of the algorithms developed in this work.

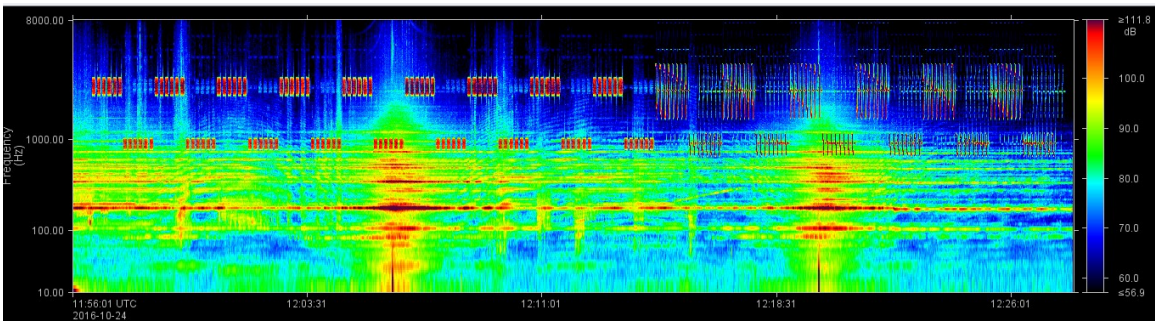

Figure 3.1: Power spectrum showing detected vessels in the October 2016 measurement

At a second sea experiment – the ADEON – which was developed and deployed in November of 2017, acoustic data were measured from the U.S. Mid- and South Atlantic Outer Continental Shelf (OCS). Acoustic arrays were deployed for long-term measurements of both the natural and human factors that are active in the region. The objectives of the ADEON experiments were 1) to understand the cumulative impacts that the natural and human factors have on marine resources and provide insight for ecosystem-based management efforts, 2) to assess baseline soundscape and ecosystem conditions that will support predictive environmental modeling and trend analyses in the the region, 3) to assess the spatial and temporal characteristics of the soundscape and biological sources, including their expected variation and correlation with distance, and 4) to provide an open source data stream platform that will facilitate future development of ecological models targeted for other environments and applications.

Although there were a few different arrays that were deployed at the ADEON

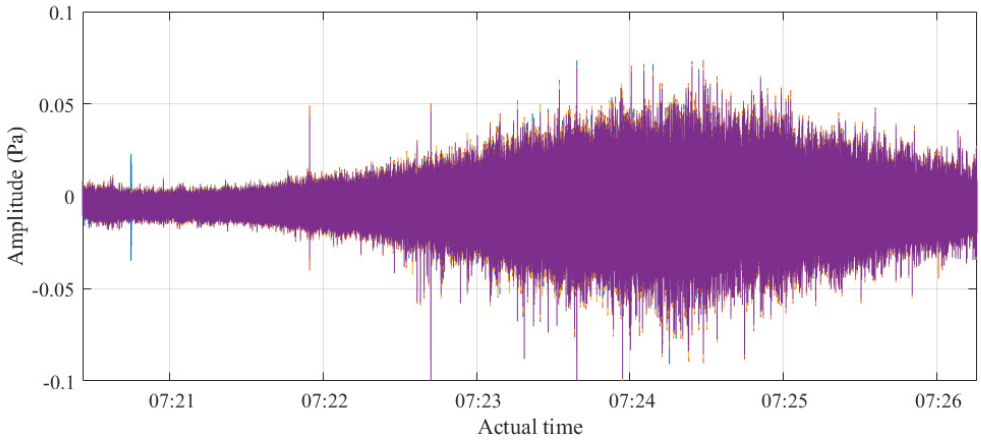

Figure 3.2: Time series from ADEON data set measured with timestamp 2019-06-08; 07:21:05, $B = \{0, 8000\}$ and $F_s = 16kHz$.

experiments, the array used in this study is a combination of a two-element VLA with 0.5 m spacing, and two horizontal elements with 0.5 m spacing, so that the array deployed at a depth of 291 m with a 1.5 m offset from the seafloor is described within the first quadrant of a sphere.

It is also expected that this array will be able to provide compass bearings in addition to a vertical arrival angle. Various acoustic sources were detected during these experiments. Some of the recorded data sets from ADEON experiments are open source [1] and some preliminary results showing the detection of various acoustic sources have been documented. The data set used for the vessel localization algorithm developed in this work are obtained from JASCO's AMARs sampled at 16 kHz and are strictly based on the detection of vessels. The power spectrum of the measured noise from the ADEON experiment prior to post-processing is showed in Fig 3.2.

3.4 Acoustic Source Sensing

Acoustic source sensing is the development of systems that are able to detect acoustic sources or in some cases to track them. Source detection relates to becoming aware of the presence of a type of acoustic source, for instance vessels, while source tracking deals with estimating the state (i.e. position, velocity or acceleration) of single or multiple moving targets. The latter is often of interest in surveillance or in military

[1] https://adeon.unh.edu/data_portal

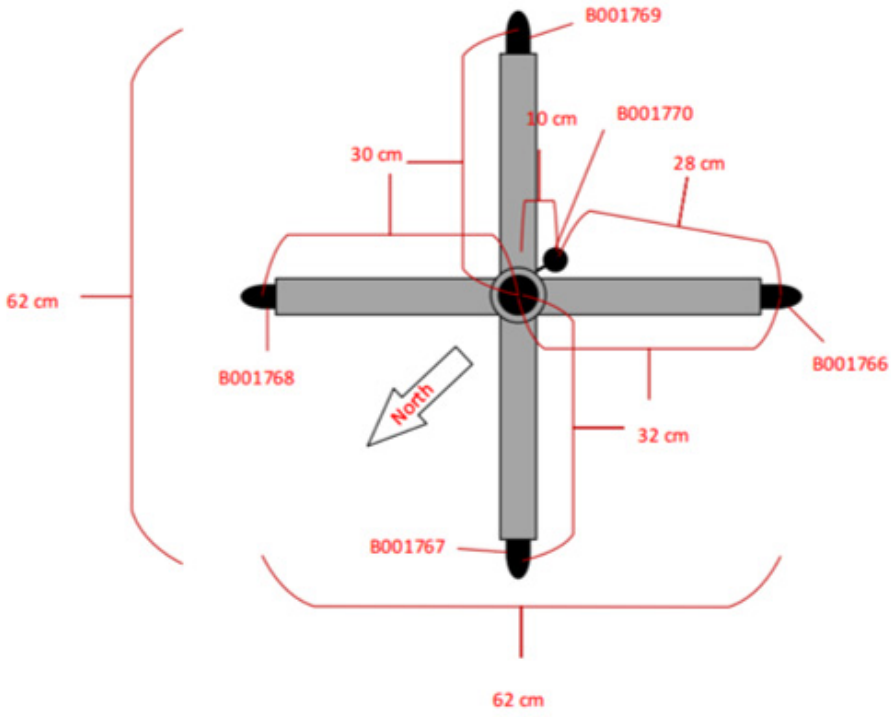

Figure 3.3: Geometry of the deployed array in CANAPE.

applications in which systems accuracy and low latency is of great importance. The term *source localization* is used interchangeably with *source tracking* in this work.

The traditional methods that apply acoustic sensors for source tracking either use active systems (as in sonar applications) or passive systems which majorly rely on acoustic hydrophones [**?**]. Traditionally, in active systems, a row of acoustic arrays transmit at a certain frequency and the target is tracked by the reflection of the echoes. These systems can be limited in mission-critical scenarios because; 1) they need to be towed by a submarine or ship; 2) their tracking areas depend on the mobility and trajectory of the tracking platform; and 3) it is expensive and almost impractical to maintain a 24-hour surveillance using the tracking platforms. Underwater sensor networks have been proposed to address some of these problems [**?**].

The application of acoustic sensors for source tracking relies on algorithms that are able to estimate the source position by computing either the source range, DOA, or time difference of arrival, or a combination of these observation parameters. When the target is detected, the measured acoustic pressure is spatially sampled and the observation parameters can be estimated by applying signal processing algorithms.

Finally, the estimation process may require some filtering techniques to improve the tracking accuracy [**?**].

Intuitively, visual detection (as in video surveillance) of moving targets comes to mind as a pertinent solution for source tracking. However, video systems are limited in scope due to variability in sea-state and weather conditions [**?**]. Thus, other methods have been studied in literature to achieve source tracking with less limitations.

3.4.1 Matched Field Processing

Matched field processing is a signal processing technique that has been applied extensively for target tracking. In principle, MFP estimates the range, depth and/or azimuth of a target by matching the complex pressure field measured at an array of sensors with replicas (often referred to as the *replica fields*) of the acoustic field computed from numerical models representing the acoustic pressure fields. The models rely on the knowledge of the waveguide i.e. parameters such as the sediment properties and the sound-speed profile. The replica fields shown in Fig. 3.4 are computed over a grid of possible locations (in range $\vec{r}$ and depth z) in an acoustic waveguide. The acoustic source (at the star symbol) is located at an unknown location $\vec{r}_0, z_s$ and the position estimate is chosen at the point of best match with the measured acoustic field at the array. The choice of the acoustic waveguide is important in replicating the signal propagation environment.

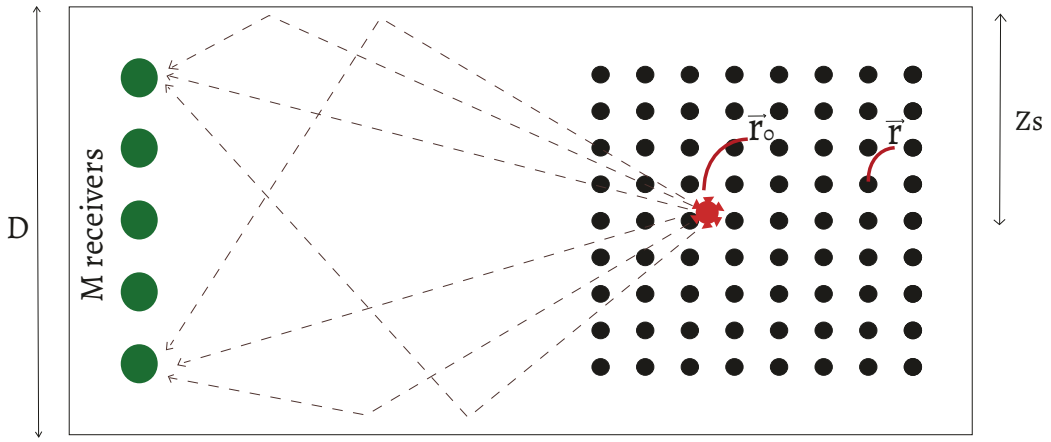

Figure 3.4: Depiction of the matched-field processing concept representing the grid of the field replicas.

To estimate the point of best match of the pressure fields, the replica fields are matched with the measured complex pressure fields at the array by computing the *ambiguity surface* of the propagation field. The ambiguity surface is computed by applying plane-wave beamforming techniques which are developed to estimate the DOA of a signal by canceling other interfering sources. However, just as in conventional plane-wave beamformers with sidelobes, the ambiguity surface also contains ambiguous peaks [6, 16]. This leads to a mismatch of the ambiguity surface. Moreover, the choice of the waveguide model coupled with array tilting due to mobility significantly contribute to mismatch in MFP.

3.4.2 Plane-wave Beamforming

In beamforming, the goal is to estimate signals of interest arriving from specific directions in the presence of noise and other interfering signals by using an array of spatially separated sensors. It is generally assumed that the spatial sensors have the same characteristics and are omnidirectional or isotropic such that their response to impinging signals are independent of the DOA. According to the relative locations of the sensors, the arrays can be divided into three classes: 1) one-dimensional (1-D) or linear arrays; 2) two-dimensional (2-D) or planar arrays; and 3) three-dimensional (3-D) or volumetric arrays. Each of the classes can be further grouped into categories based on the elemental spacing: 1) regular spacing which includes uniform and non-uniform spacing; and 2) irregular or random spacing. The beamforming technique developed in this work is based on arrays with regular spacing.

The beamforming problem is formulated on the assumption that the array is sufficiently distant from the source, such that the impinging signals is planar at the array. Thus, for a ULA, the received signal is of the form

$$\mathbf{x}(t) = \mathbf{s}(t)e^{j\omega_c t}, \tag{3.1}$$

where $s(t)$ is the signal envelope, ω_c denotes the carrier frequency and $j = \sqrt{-1}$. Due to the planar received signals, spatial beamformers are referred to as *plane-wave beamformers*.

The distance d that separates the plane waves arriving at the adjacent elements (sensor 0 and 1) of an array depicted in Fig. 3.5 is $d\ \cos\theta$. Also, the time interval Δt

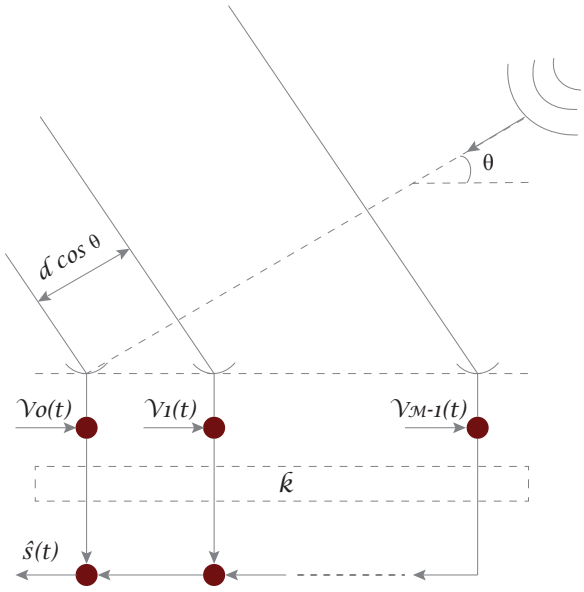

Figure 3.5: A uniformly-spaced array of sensors depicting plane-wave beamforming.

taken for the wave to propagate from sensor 0 to 1 is $d\ \cos\theta/c$, so that

$$\Delta t = 2\pi d \cos\theta/(\omega_c \lambda), \tag{3.2}$$

where λ is the wavelength and is related to c by the wavenumber (k) using

$$k = \frac{\omega_c}{c} = \frac{2\pi}{\lambda}. \tag{3.3}$$

Eq. (3.3) is of a single dimension and is applicable for ULAs. However, for 3-D arrays, the wavenumber equation can be represented in the Cartesian coordinate as $\mathbf{k} = [k_x, k_y, k_z]^T$. Similarly, for uniformly linear arrays, $[k_x, k_z] = 0$ for HLA so that $\mathbf{k} = [k_y]$, while $[k_x, k_y] = 0$ for VLAs such that $\mathbf{k} = [k_z]$.

The beamforming equation relies on the response of the array to copies of an impinging signal received at the array. From (3.1), $s(t)e^{j\omega_c t}$ is the signal at sensor 0 at a spatial origin at time t, while $s(t + \Delta t)e^{j\omega_c t}$ is the signal at sensor 1 at the same time instant. Therefore, for an M-element array

$$s(t)e^{j\omega_c}\left(t + \frac{2\pi d \cos\theta}{\omega_c \lambda}\right) = s(t)e^{j\omega_c t}e^{j\frac{2\pi m}{\lambda} d\cos\theta} \tag{3.4}$$

where $m = 0, 1, \ldots, M-1$ and the first element of the array is sensor 0. Eq.(3.4) is the output of the ULA obtained by linearly combining the measurements at the sensors.

It is also observed from (3.4) that in the frequency domain, the received signals at the elements of the array are phase shifted. Thus (3.4) forms the foundation for the *array factor* which is discussed in Section 3.4.3.

3.4.3 Array Factor

The AF describes the complex-valued radiation pattern (in the far field) for an array consisting of M-element isotropic radiators. From Fig. 3.5, because the transmission paths between a radiating source and the receive elements are not equal, delayed copies (in the time domain) of the information signal are received with a phase shift (in the frequency domain) at each element. This concept is obvious from (3.1) and (3.4) in which the phase information of the received plane waves are different at the elements of the array. From (3.1), for an impinging plane wave whose envelope a_m is of a unit energy, the phase shift experienced by an element at the spatial point of origin is zero, such that $a_m = x(t) = 1$. Thus, for a reference sensor at a spatial origin 0, the AF is

$$\begin{aligned} \text{AF} &= 1 + e^{jkd\cos\theta} + e^{jk2d\cos\theta} + \cdots + e^{jk(M-1)d\cos\theta} \\ &= \sum_{m=0}^{M-1} e^{jkmd\cos\theta} = \sum_{m=0}^{M-1} e^{jkmd\cos\theta/(M-1)}. \end{aligned} \tag{3.5}$$

By setting $\psi = kd\cos\theta$, the AF yields

$$\text{AF} = \sum_{m=0}^{M-1} e^{jm\psi} = 1 + e^{j\psi} + e^{j2\psi} + \cdots + e^{j(M-1)\psi}. \tag{3.6}$$

Multiplying (3.6) by $e^{j\psi}$ yields

$$\text{AF} \cdot e^{j\psi} = e^{j\psi} + e^{j2\psi} + \cdots + e^{jM\psi}. \tag{3.7}$$

Further, subtracting (3.7) from (3.6) yields $\text{AF}(1 - e^{j\psi}) = 1 - e^{jM\psi}$, and rearranging this results in

$$\begin{aligned} \mathrm{AF} &= \frac{1 - e^{jM\psi}}{1 - e^{j\psi}} \\ &= \frac{e^{jM\psi/2}}{e^{j\psi/2}} \cdot \frac{e^{jM\psi/2} - e^{-jM\psi/2}}{e^{j\psi/2} - e^{-j\psi/2}}. \end{aligned} \tag{3.8}$$

The maximum value of the AF occurs when $\psi = 0$. Hence, disregarding the phase information and normalizing (3.8) yields

$$\mathrm{AF} = \frac{\sin\left(M\psi/2\right)}{M \sin \psi/2}. \tag{3.9}$$

The array factor determines the beam pattern of an array which in turn determines the ability to measure the information signal at an array of receivers as accurately as possible. Among many factors, the following observations are made about the radiation pattern computed using the AF.

- A maximum beam is obtained at $\psi = 0$ which corresponds to $\theta = 90°$ (i.e. the broadside direction) which is determined as normal to the plane of the array.
- The width of the main lobe has an inverse relationship with M, such that the first null beam width is obtained where the numerator of (3.9) goes to zero.
- The width of the main lobe in terms of ψ is $2\pi/M$, while the width of the minor lobes are half that.
- The number of sidelobes increases as M increases, while the sidelobe level decreases with M.

These observations are characterized analytically and its application for the arrays used in this work are discussed in greater details in this chapter.

Fig. 3.6 shows the beam pattern for an isotropic ULA for an impinging signal at $0°$ with different number of elements and different elemental spacing derived from (3.9). It is observed that the beam pattern is symmetric for isotropic radiators and the beam width of the main lobe decreases as M increases. Similarly, the number of sidelobes increases with M.

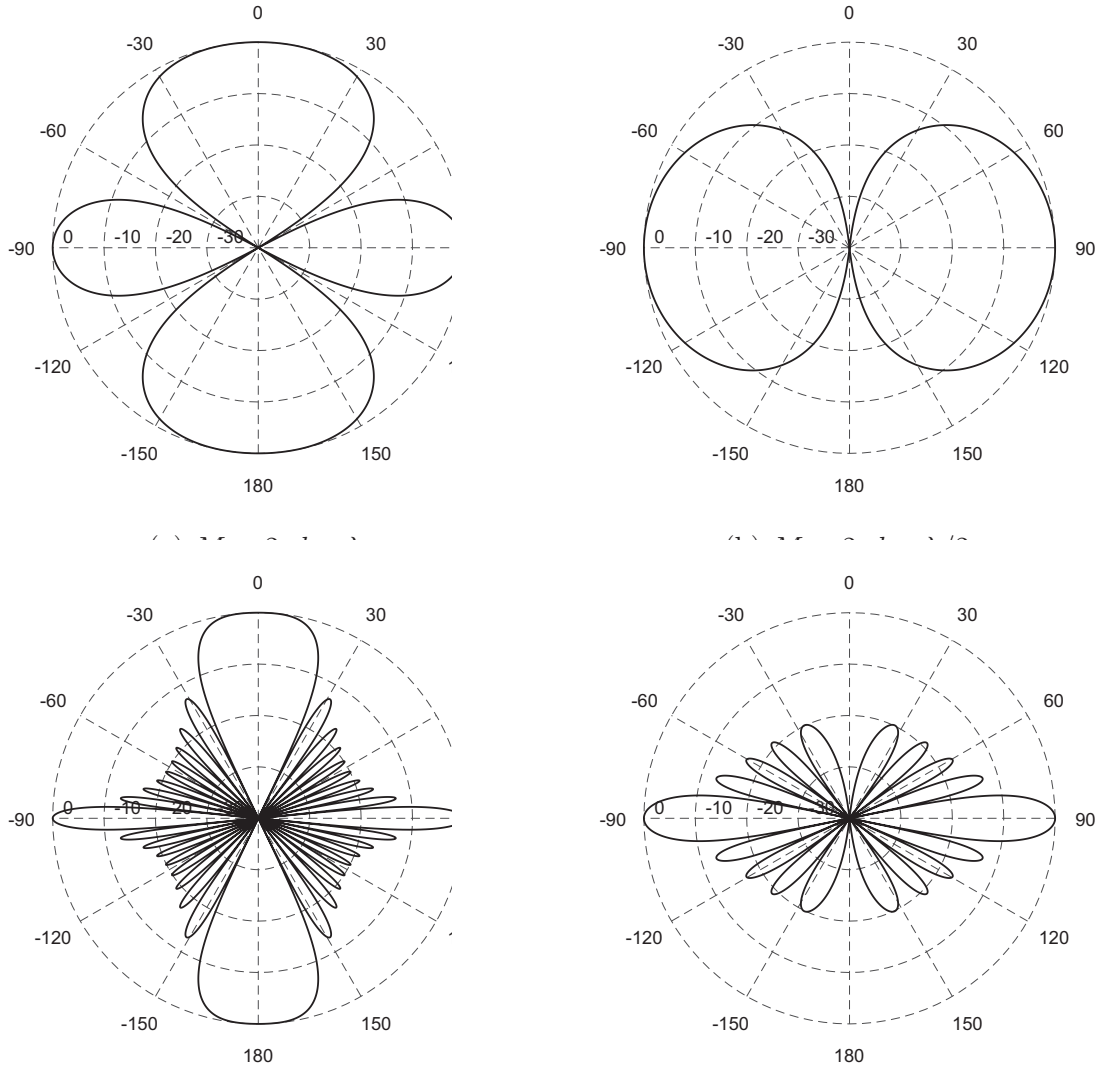

(c) $M = 10, d = \lambda$ (d) $M = 10, d = \lambda/2$

Figure 3.6: Array pattern construction for ULAs with different elemental spacing for $M = 2$ in (a) - (b); and $M = 10$ in (c) - (d). The radius values are evenly spaced angles between 0 and 2π

In beamforming, it is desirable to focus the beam in the direction of the signal of interest, while the interfering sources are eliminated. To achieve this, it is assumed that the magnitudes of the signal envelopes at all the elements are the same (i.e. $|a_0| = |a_1| = \ldots = |a_M - 1|$), which are all arbitrarily set to 1, and the phase shift between the elements is α. Therefore, the signal excitation at each element of the array can be expressed as $a_m = e^{jm\alpha}$ and the AF is

$$\text{AF} = \sum_{m=0}^{M-1} e^{jkmd\cos\theta + jm\alpha} \tag{3.10}$$

redefining $\psi = kd\cos\theta + \alpha$. The beam steering in specific direction is achieved by setting the value of α in the desired look direction. For instance $\alpha = 0°$ at broadside i.e. the impinging signal is received without having been phased shifted.

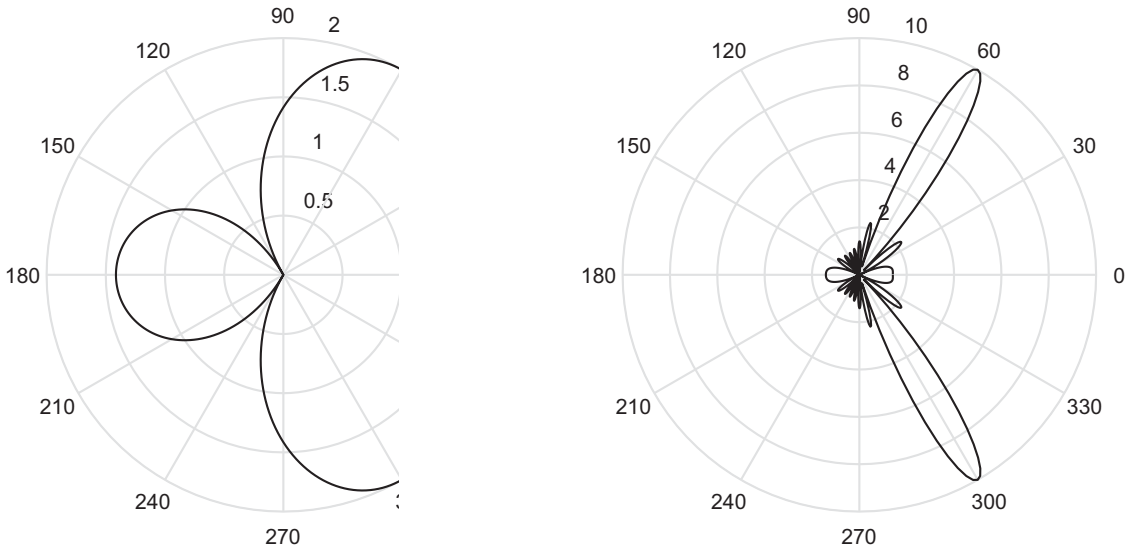

(a) $N = 2, d = \lambda$ (b) $N = 10, d = \lambda/2$

Figure 3.7: Beam steering pattern for a ULA with two and ten elements. The radius is evenly spaced angles between 0 and 2π

From Fig. 3.7, it is observed that the main lobe can be steered in the desired direction at 60° such that the gain of the signal of interest can be maximized in the look direction. Similarly, the directionality is maximized by increasing the number of elements M as in Fig. 3.7b.

The example illustrated in Fig. 3.7 is derived by setting the received gain (i.e. signal

envelope) to unity, such that the beam energy is maximized in the desired look direction. In practice, weighting vectors $\mathbf{w}_s$ are computed to maximize the gain in the look direction characterized by azimuth and elevation $\{\theta, \phi\}$.

There are several algorithms that have been developed in literature to compute the weighting vector that maximizes the total output power at the array in the look direction of the signal of interest. A well-known solution is the MVDR which minimizes the total array output power by setting the gain in the desired response direction to unity. The spatial weight $\mathbf{w}$ of the MVDR filter is computed from

$$\mathbf{w} = \frac{R_x^{-1}\mathbf{v}}{\mathbf{v}R_x^{-1}\mathbf{v}} \tag{3.11}$$

where $\mathbf{v}$ is the steering vector (i.e. the phase information at the array) corresponding to the desired response direction, and R_x is the covariance matrix that contains the contributions from all incoming signals and noise. Generally, beamforming algorithms are developed for narrow beams. However, in wideband scenarios, the performance deteriorates significantly. Hence, the system's bandwidth is divided into sub-bands wherein the beamforming algorithms can be applied. Details of the wideband beamformer are developed in [17, 18].

The overall goal of a beamformer is to estimate the direction of arrival (DOA) of a source as accurately as possible, for which several techniques have been developed in literature. These techniques are broadly categorized into 1) conventional beamformers; and 2) adaptive beamformers or phased array. Conventional techniques, such as the delay-and-sum beamformer, use a fixed set of weights and time-delays to combine the signals from the sensors in the array. These techniques primarily rely only on the information about the location of the sensors in space (contained in the steering vector) and the known DOA to estimate the signal of interest. In contrast, adaptive beamforming techniques such as the MVDR, Multiple Signal Classification (MUSIC) and the more recent Estimation of Signal Parameters via Rotational Invariance Techniques (ESPRIT) algorithms, combine the array steering vector with the properties of the signals measured by the array to improve the quality of the received signal while rejecting the unwanted signals from other directions.

A conventional beamformer, although simple in its implementation, has the weighting vectors of equal magnitudes across the elements of the array, hence limited in

practical applications. One major disadvantage of the delay-and-sum method is its poor resolution – the width of the main lobe and the power of the side lobes, limit its ability to separate closely spaced signals [16]. On the other hand, an adaptive beamformer, with a more complex implementation, dynamically adapts its response to the different conditions to mitigate interferes while minimizing the total noise output. Due to the variation of noise with frequency, in wide band systems it often desirable to implement the algorithms in the frequency domain.

Capon's minimum variance technique overcomes the poor resolution associated with the delay-and-sum and yields a significant improvement. However, Capon's method fails when the interferers are correlated with the desired signal. The MUSIC and ESPRIT algorithms rely on the decomposition of the eigen structure of the received signals and have shown excellent accuracy in signal resolution in both theoretical and experimental studies. MUSIC algorithm relies on the foreknowledge of the number of incoming signals or by searching the eigenvalues to determine the number of incoming signals. The ESPRIT algorithm does not rely on an exhaustive search through all possible steering vectors to estimate the DOA, hence reduces the computational requirements compared to MUSIC.

Although the ESPRIT as well as other adaptive beamforming approaches are efficient algorithms depending on the application, from statistical analysis, the ML-BF is an asymptotically unbiased optimal estimator whose solution is closest to the CRB [**?**]. It is also well known that the output of the optimum distortionless beamformer is the ML estimate of the signal. Thus, Section 3.5 discusses the ML-BF used to estimate the bearing and elevation of shipping vessels.

3.5 Maximum-Likelihood Adaptive Beamformer

In this section, a maximum-likelihood beamformer is described to estimate the optimum bearing of the sound produced by a vessel to a compact array.

Compact arrays are robust in estimating the azimuth and elevation angles (hereafter referred to as directionality) of acoustic sources. This property has been exploited in the detection and tracking of vessels [**?**, **?**] and marine mammals [**?**, **?**, **?**], and is suitable for broadband sound sources [**?**, **?**]. Generally, using compact arrays to estimate directionality relies on the estimate of the TDOA of a plane wave measured

at multiple sensors. Various TDOA estimators have been proposed in literature for estimating directionality [**?**, **?**, **?**, **?**, **?**]. It has also been established that the ML-BF approach achieves the lowest possible variance of a linear TDOA estimator specified by the Cramér-Rao lower bounds [17]. Hence, a ML-BF developed in [**?**, **?**] is applied to estimate the measured ambient noise directionality in bearings in this section.

Suppose that the received signal at sensor m (for $m = 0, 1, \ldots, (M-1)$) sampled at the same time instant, is arranged in a vector $\mathbf{x}(n)$. The received signal is a linear combination of the desired signal $\mathbf{s}(n)$ and the additive noise $\mathbf{n}(n)$ expressed similarly to (2.11) as

$$\mathbf{x}(n) = \mathbf{s}(n) + \mathbf{n}(n). \tag{3.12}$$

The output of a processor with coefficients $\mathbf{w} = [w_0 \ \ldots \ w_{(M-1)}]^T$ computed in the spatial s domain is

$$\mathbf{y}(n) = \mathbf{w}^H\mathbf{x}(n) = \mathbf{w}^H\mathbf{s}(n) + \mathbf{w}^H\mathbf{n}(n), \tag{3.13}$$

where H denotes the Hermitian transpose The power of the signal measured at the output of the linear processor is

$$P_y(n) = \mathbb{E}\{|\mathbf{y}(n)|^2\} = \mathbb{E}\{\mathbf{w}^H\mathbf{x}(n)\mathbf{x}^H(n)\mathbf{w}\} = \mathbf{w}^H\mathbf{R}_x(n)\mathbf{w} \tag{3.14}$$

where the output signal power is

$$P_s(n) = \mathbb{E}\{|\mathbf{w}^H\mathbf{s}(n)|^2\} = \mathbb{E}\{\mathbf{w}^H\mathbf{s}(n)\mathbf{s}^H\mathbf{w}\} = \mathbf{w}^H\mathbf{R}_s(n)\mathbf{w} \tag{3.15}$$

and the output noise power is

$$P_n(n) = \mathbb{E}\{|\mathbf{w}^H\mathbf{n}(n)|^2\} = \mathbb{E}\{\mathbf{w}^H\mathbf{n}(n)\mathbf{n}^H\mathbf{w}\} = \mathbf{w}^H\mathbf{R}_n(n)\mathbf{w}. \tag{3.16}$$

where $\mathbf{R}_s, \mathbf{R}_n$ are the covariance matrices of the signal and the noise respectively.

Eq. (3.15) and (3.16) show that the signal output power and noise output power are linear combinations of the weighted values of the signal and noise measured at the array. These equations form the basis on which most filtering techniques (spatial or temporal) are designed. In the spatial filtering sense, for plane waves arriving from an

impinging radial bearing angle θ at a spatial array of M-elements, with inter-element separation of d, the steering vector $\mathbf{v}(\theta)$ is

$$\mathbf{v}(\theta) = \exp(j2\pi md\cos\theta), \tag{3.17}$$

for $0 \leq \theta \leq 360^\circ$ in the horizontal plane. The desired goal is to compute a set of complex spatial weights ($\mathbf{w}$) that results in a perfect phase alignment of all the received signals at the sensors. The beamforming weighting vector that phase-aligns a signal from direction θ at the array elements is the steering vector that is matched to the array response of the impinging signal from the same look direction, i.e. $\mathbf{w}(\theta) = \mathbf{v}(\theta)$. Hence, the output of the spatially matched filter, derived from (3.13) yields

$$\mathbf{y}_s(n) = \mathbf{w}^H(\theta)\mathbf{x}(n) = \mathbf{v}^H(\theta)\mathbf{x}(n), \tag{3.18}$$

and the output noise power measured at the linear processor, derived from (3.14) is

$$P(n) = \mathbb{E}\{|\mathbf{w}^H\mathbf{x}(n)|^2\} = \mathbb{E}\{\mathbf{w}^H\mathbf{x}(n)\mathbf{x}^H(n)\mathbf{w}\} = \mathbf{w}^H\mathbf{R}_x(n)\mathbf{w}, \tag{3.19}$$

where P is the power of the impinging signal in the spatial dimension.

Eq. (3.19) is a sufficient solution to estimate the directionality for signals measured at ULAs where accuracy is a huge trade off for low system complexity. However, the steering vector of an optimum beamformer that is applicable for three-dimensional (3D) arrays (as described in Section 3.3) can be resolved in azimuth and elevation from the expression

$$\mathbf{v}(\omega, \Theta) = \exp(j2\pi f \mathrm{p}_m \mathbf{r}(\Theta)/c), \tag{3.20}$$

where p_m is the spatial location of sensor m, $\omega = 2\pi f$ is the discrete frequency values and c is the sound speed. Also, the array steering vector in a 3-D space is characterized by the spatial frequencies, such that

$$\mathbf{r}(\Theta) = \begin{bmatrix} k_x \\ k_y \\ k_z \end{bmatrix} = \begin{bmatrix} \sin(\theta)\cos(\phi) \\ \sin(\theta)sin(\phi) \\ \cos(\theta) \end{bmatrix} \tag{3.21}$$

and $\{\theta, \phi\}$ are the azimuth and elevation, respectively, which are to be estimated. To apply (3.20) and (3.21) on wideband signals, the signal bandwidth is divided into narrowband bins where spatial beamforming techniques can be applied. The signal radiated by the source is assumed to be a random process with non-uniform PSD, such that most of the energies of the signal is concentrated within the bandwidth $B = [f_0, f_{max}]$. The sensors are synchronized and the received signals are sampled at $F_s = 2f_{max}$.

With slight modifications to (3.12), the acoustic pressure field received at the array is a linear combination of the signal of interest and the additive noise, represented in the frequency domain as

$$\mathbf{X}(\omega) = \mathbf{S}(\omega) + \mathbf{N}(\omega), \tag{3.22}$$

where $\mathbf{S}(\omega)$ and $\mathbf{N}(\omega)$ are the N-dimensional FFT spectra of the signal of interest and the additive noise, respectively, and $R_N(\omega)$ is the covariance matrix of the background noise $\mathbf{N}(\omega)$ with a normal distribution and zero mean. Similar to (3.18), the output of the spatial beamformer also yields

$$\mathbf{Y}(\omega) = \mathbf{X}(\omega)\mathbf{v}^H(\omega, \Theta) = \mathbf{S}(\omega)\mathbf{v}^H(\omega, \Theta) + \mathbf{N}(\omega). \tag{3.23}$$

It is noteworthy that the signal of interest $S(\omega)$ in this application is the vessel noise.

The maximum-likelihood beamformer is based on the principle that the parameter vectors Θ can be estimated from the observed sample vectors $\mathbf{Y}(\omega)$, $\forall\ \omega \in B$. Thus, the ML estimate (i.e. $\hat{\Theta}_{ML}$), defined by the conditional joint probability density function resolves to the well-known result [17, **?**]

$$\hat{\Theta}_{ML} = \arg\max_{\Theta} \sum_{\omega \in B} \Re e\{\mathbf{Y}(\omega)\}. \tag{3.24}$$

The justification for the optimal performance of the ML-BF in the Cramér-Rao lower bounds has been described extensively in literature [17, 2, **?**]. Thus, this dissertation will detail the procedural implementation of the ML estimator that is developed to estimate the directionality of a source (vessel) as a function of time. The three steps for developing the ML-BF is described next, followed by the results computed at the output of the ML-BF.

Step 1. Partition the time-series into equal windows.
The time series observations of the measured noise across the elements of the array are divided into K intervals of length ΔT, where for $k = 1, 2 \cdots, K$, each window start time is equal to $(k-1)\Delta T \ + 1$ and the stop time is equal to $K\Delta T$.

As such, the ambient noise time-series at the k-th window is $\mathbf{x}_k$ and the entire time-series occupies $K\Delta T$ windows. A procedure for choosing an optimal ΔT is described in [17]. In this application, $\Delta T \approx 0.25$ s, i.e. 4096 samples for the broadband noise time-series sampled at the original sampling frequency $F_s = 16\ kHz$.

Step 2. Transform each time-series window to the frequency domain.
Following the expression in (3.22), the $K\Delta T$ windows are transformed to the frequency domain, such that $\mathbf{X}_k(\omega) \xrightarrow{\mathscr{F}} \mathbf{x}_k$ in the k-th window, and $k \in K$. Thus, there are $\mathbf{X}_1(\omega), \mathbf{X}_2(\omega), \ldots, \mathbf{X}_K(\omega)$ available sequences of snapshots, where $\mathbf{X}_k(\omega)$ is an N-dimensional vector and $N = 8192$ is the DFT size of the frequency domain snapshot at time k and (ω) denotes the frequency domain signal. This step requires high frequency resolution, thus N must be sufficiently large. Steps 1 and 2 can be easily computed using the *spectrogram* function in Matlab that computes the Fourier transform using short-time windows. In this processing, $N \approx 8192$ points.

Step 3. Compute the array response and the spectral matrix.
The steered response of the array is computed from

$$\mathbf{Y}_K = \mathbf{X}_K(\omega)\mathbf{v}^H(\omega, \Theta), \tag{3.25}$$

where $\mathbf{Y}_k$ is an N-dimensional vector. It is noteworthy that (3.20) is defined as a function of the wavenumber which is computed over the N DFT window, such that the expanded data matrix, i.e. the steered array response is

$$\hat{\mathbf{Y}} = \begin{bmatrix} \mathbf{Y}_1(0) & \vdots & \mathbf{Y}_2(0) & \vdots & \mathbf{Y}_K(0) \\ \mathbf{Y}_1(1) & & \mathbf{Y}_2(1) & \vdots & \mathbf{Y}_K(1) \\ \vdots & & \vdots & \cdots & \\ \mathbf{Y}_1(N-1) & & \mathbf{Y}_2(N-1) & \vdots & \mathbf{Y}_K(N-1) \end{bmatrix}. \tag{3.26}$$

is of dimension $K \times N$, normalized by the $\frac{1}{\sqrt{K}}$ factor. In array processing, the primary statistics of interest is to estimate the spatial spectral matrix. It has been shown that

in the ML sense, the estimate of the spatial spectral matrix is the sample correlation matrix [17] of the spatial snapshots expressed as

$$\mathbf{C}_{\mathrm{Y}} = \frac{1}{\sqrt{K}}\hat{\mathbf{Y}}\hat{\mathbf{Y}}^{H}. \tag{3.27}$$

Eq. (3.26) yields a four dimensional matrix whose dimensions represent the frequency bins of N- dimension, the spatial snapshots of K-dimension, the discretized directionality represented in azimuth θ and elevation ϕ. To obtain the ML estimate $\hat{\Theta}_{ML}$ from $\mathbf{C}_{\mathrm{Y}}$, a 2-D grid search of the azimuth and the elevation is set up to compute (3.24). The estimate $\hat{\theta}$ corresponds to the source directionality $\{\theta, \phi\}$ i.e. the directionality of the vessel.

3.5.1 Directionality Results and Discussions

To evaluate the the accuracy of the bearing estimates, data sets that show the presence of vessels at the CPA in both CANAPE and ADEON are processed. From (3.23), the signal of interest $S(\omega)$ is the vessel's noise emanating from the propeller.

It is expected that the directionality accuracy should be similar for both bearing and elevation. This expectation will hold in an ideal waveguide that is void of surface and bottom interactions. However, as indicated in [**?**], model (3.23) may not be accurate enough in the elevation domain due to variations in the propagation environment and boundary interactions with the propagated signals among other factors. This is especially true in shallow environments where the propagation of sounds could significantly differ in the vertical and horizontal planes. Additionally, in shallow environments, estimating the elevation angles could be challenging because the slant propagation angle of the source to the array could be much longer than the column depth [6] (see Fig. 3.17). Therefore, the estimation of the directionality is limited to the bearing domain in this work. However, to ensure accuracy in estimating the azimuth, especially in situations where the source is in close proximity to the array, a single value of the elevation angle is chosen, so that the model in (3.23) still holds true.

CANAPE's Results

The bearing estimates are computed from the five spatial (tetrahedral) elements from the CANAPE array. First, the array pattern is computed as a function of $\Theta \in \{\theta, \phi\}$ for $0 \leq \theta \leq 360^\circ$ and $\phi = 3^\circ$ (when the vessel is closest to array) using the five-element tetrahedra array.

The PSD of the measured acoustic pressure at the array over the travel duration of the vessel, is shown in Fig. 3.8. The PSD is computed from the model in (3.23) as a function of the travel time of the vessel. The power in the measured vessel noise estimated at the output of the beamformer shows a scaled maximum power of about 140 dB re 1 μPa^2 /Hz, and an overall minimum power of about 50 dB re 1 μPa^2 /Hz within the bandwidth $B_C = \{10,600 \text{ Hz}\}$. Further, it is observed that the noise power is persistent within certain bandwidths (for instance at about 170 - 200 Hz and about 370 - 390 Hz) than in the others. These observations confirm the frequency dependence of vessel noise which has been demonstrated in literature.

Also, recall from Fig. 3.1, that the measured acoustic pressure time-series shows high amplitudes at the CPA of the vessel. Similarly, Fig. 3.8 shows that the dominant power occurs around the $12:06$ timestamp within the bandwidth $B_C = \{10,600 \text{ Hz}\}$ for the vessel.

A similar observation is made in the normalized spectrogram of Fig. 3.9, showing the dominant energies in the time-series around the the $12:06$ timestamp. The normalized spectrogram is computed to emphasize the bandwidths and the timestamps over which the power in the signals are concentrated. The well established bathtub pattern [6] in the spectrum of vessel-generated noise is also more pronounced in the normalized spectrogram. From Fig. 3.8 and Fig. 3.9 suggest that the vessel must have closely approached the array around the $12:06$ timestamp. These observations are in agreement with the dominant amplitudes observed in the time-series shown in Fig. 3.8. These observations will be further verified in the source range estimation described in Section 3.6.

To avoid interference errors induced by the sonar transmission in the CANAPE data, the frequency bins corresponding to the sonars may be manually removed before applying the beamforming algorithm. However, this is a tedious operation which could also introduce some bias in the post-processing results. Therefore, the vessel

dominant bandwidth is limited to $B_C \approx \{10,600 \text{ Hz}\}$, and is sufficiently large to achieve the desired accuracy while avoiding the interference from the active sonars.

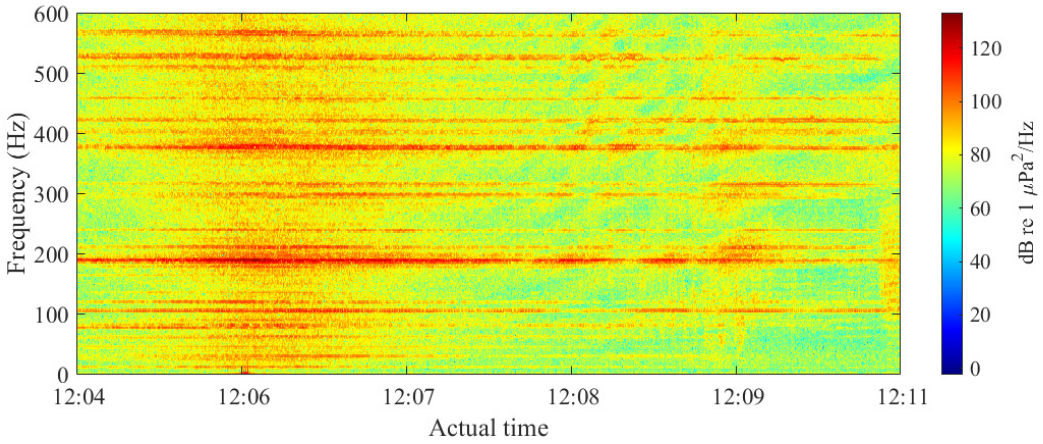

Figure 3.8: PSD of the measured noise process processed over 360 seconds, $B_C = \{10,600 \text{ kHz}\}$ and $F_s = 16kHz$.

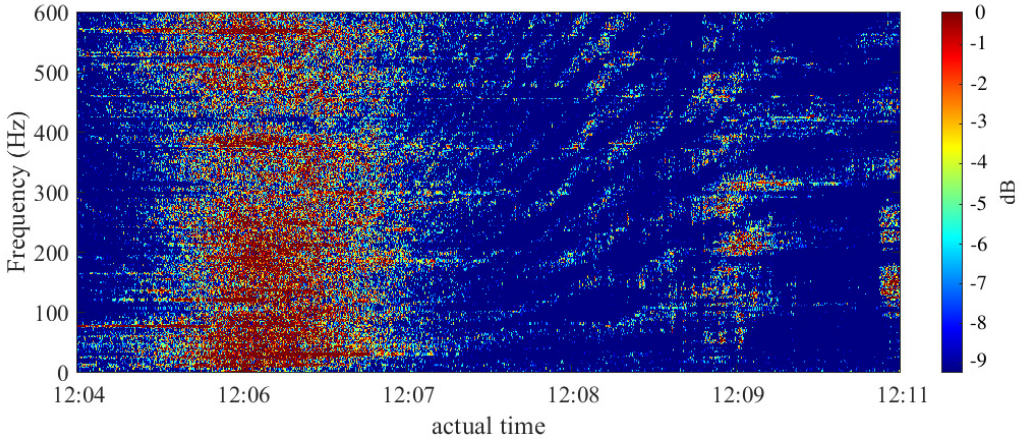

Figure 3.9: Output of the normalized spectrogram computed for $0 \leq \theta \leq 360°$, $B_C = \{10,600 \text{ kHz}\}$ and $F_s = 16kHz$.

Fig. 3.10 shows the output of the spectral matrix of the measured time-series, computed from (3.27) for $B_C = \{10,600 \text{ Hz}\}$ and $\Theta \in \{0 \leq \theta \leq 360°, \phi = 3°\}$. Similar to the earlier observations in the PSD and the normalized spectrogram of the beamformer, an abrupt transition is observed in the azimuth estimates of the vessel around the $12:06$ timestamp. It also noteworthy that the dominant azimuth lies between about $500° - 150°$ before the $12:06$ timestamp, after which the dominant azimuth lies between about $200° - 250°$ up until the end of the measurement at $12:11$.

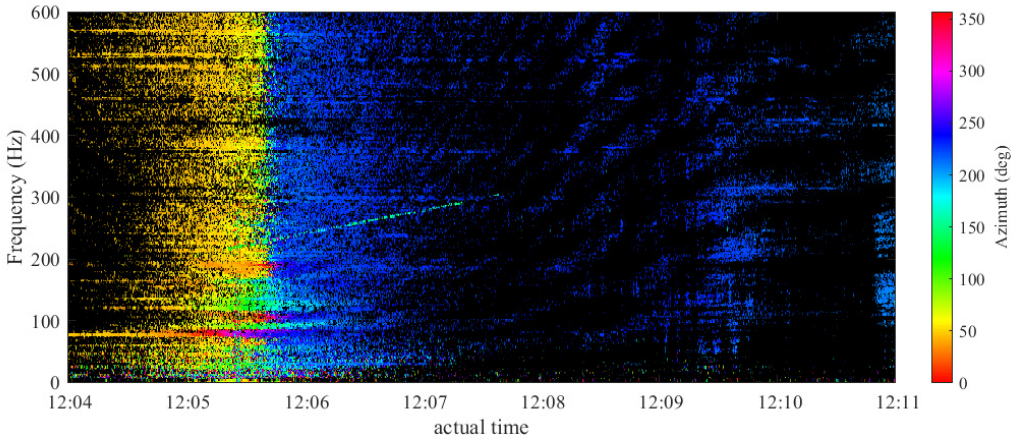

Figure 3.10: Output of the sample spectral matrix computed for $0 \leq \theta \leq 360°$, $B_C = \{10, 600 \text{ kHz}\}$ and $F_s = 16kHz$.

Finally, by applying (3.24), estimates of the bearings that correspond to the highest energy in the spectral matrix of (3.27) is computed. To achieve this, the power spectrum is summed over $B_C = \{10, 600 \text{ Hz}\}$ and the θ that corresponds to the maximum energy is obtained at each observation snapshot of the time-series. Fig. 3.11 confirms the hard transition of the bearings from about 50° to about 220° at the $12:06$ timestamp. By obtaining the vessel ID from the AIS data as demonstrated later in this chapter, it is determined that the vessel is a research vessel, and there are high chances that the vessel passed directly over the array at this timestamp.

Not included in this dissertation, it is suggested that the algorithm be optimized for instances when the vessel is close to the array to improve the bearing accuracy in such scenarios.

ADEON's Results

Similar to the CANAPE's results, the array pattern is computed from the combination of all the elements of the array, such that $\Theta \in \{\theta, \phi\}$ for $0 \leq \theta \leq 360°$ and $\phi = 3°$. Unlike the CANAPE data set, there were no sonar transmission in the ADEON data set. Thus, the entire measurement bandwidth $B_A = \{10, 8 \text{ kHz}\}$ of the data set could be fully utilized.

The following shows the results obtained from the estimates of the bearing by processing ADEON data set in a similar way as in CANAPE.

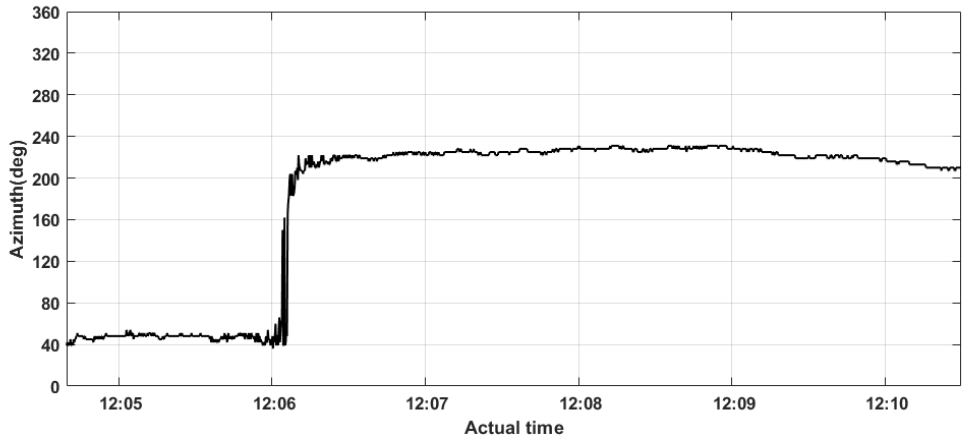

Figure 3.11: Bearings of the vessel as a function of time

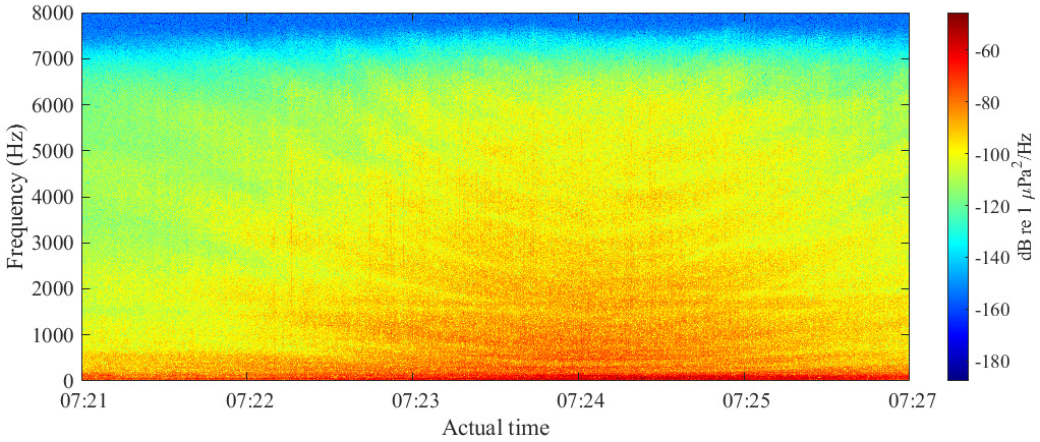

Figure 3.12: PSD of the measured noise process processed over 360 seconds, $B_A = \{10, 8 \text{ kHz}\}$ and $F_s = 16kHz$.

From Fig. 3.12, the dominant bandwidth (observed from the interference pattern) of the vessel is observed to lie in $B_A = \{10, 7 \text{ kHz}\}$. From the output power spectrum, the dominant power in the lower bandwidths (about 10 Hz - 100 Hz) spans throughout the measurement. The PSD also shows the interference pattern with the bathtub curves spans throughout the dominant bandwidth $B_A = \{10, 7 \text{ kHz}\}$.

Similarly, the normalized spectrogram from Fig. 3.13 confirms that the interference pattern spans over the entire bandwidth in the measured data and is most dominant around the $07:24$ timestamp. The interference pattern from Fig. 3.12 and Fig. 3.13 suggest that the vessel is closest to the array around the $07:24$ timestamp. The dominant power in the spectrogram is not as concentrated around a single timestamp

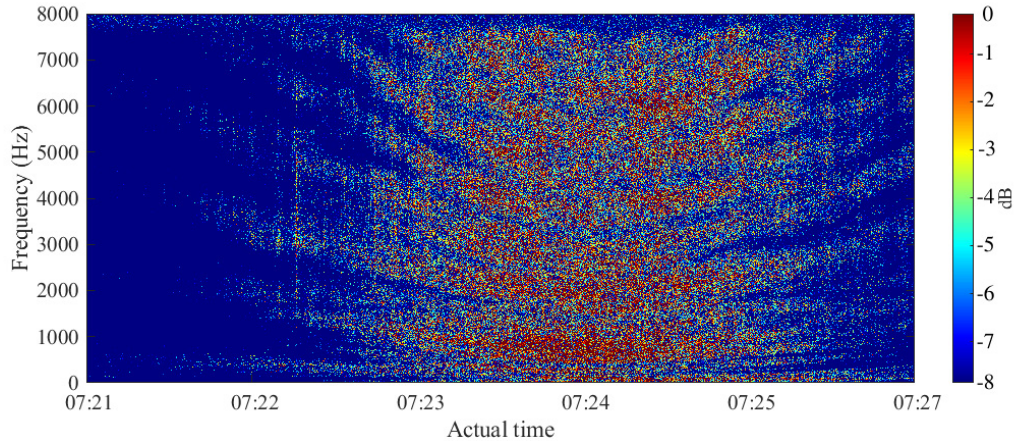

Figure 3.13: Output of the normalized spectrogram computed for $0 \leq \theta \leq 360°$, $B_A = \{10, 8 \text{ kHz}\}$ and $F_s = 16kHz$.

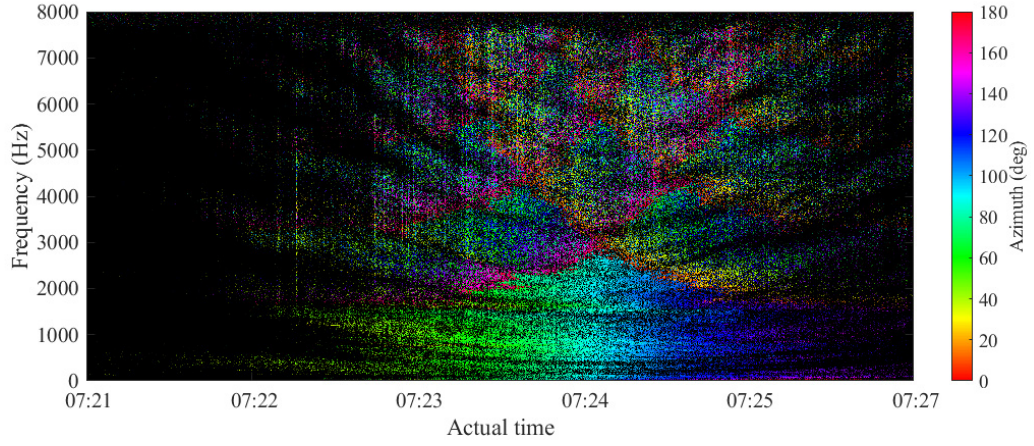

Figure 3.14: Output of the sample spectral matrix computed for $0 \leq \theta \leq 360°$, $B_A = \{10, 8 \text{ kHz}\}$ and $F_s = 16kHz$.

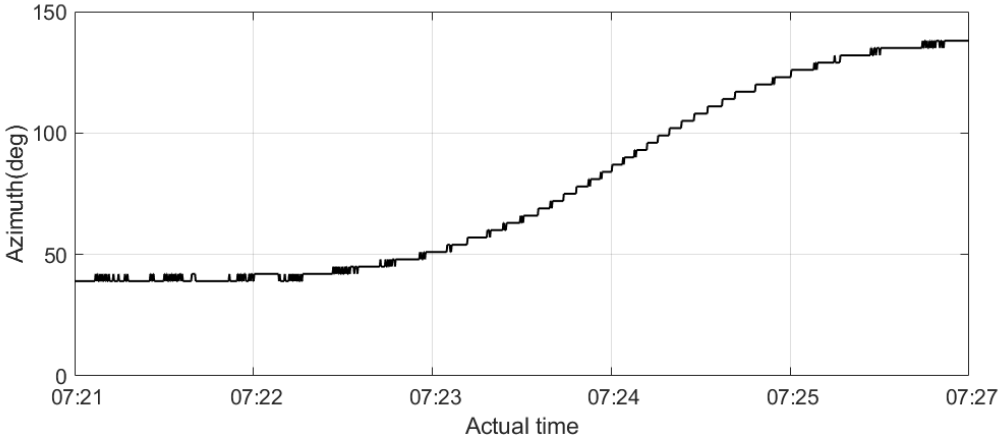

Figure 3.15: Bearings of the vessel as a function of time

as observed in CANAPE. It can therefore be implied that, although the vessel is closest to the array at the $07:24$ timestamp, it may not have passed directly above the array as in CANAPE.

Further, Fig. 3.14 represent the spectral matrix computed from (3.27) for $B_A = \{10, 8 \text{ kHz}\}$ and $\Theta \in \{0 \leq \theta \leq 360°, \phi = 3°\}$. Particularly, in the lower bandwidth (¡ 3000 Hz), the dominant azimuth gradually increases from about 40° to about 130°. However, in the higher bandwidths, this observation is less pronounced. Albeit, to estimate the source bearing, the spectra matrix in (3.27) summed over $B_A = \{10, 8 \text{ kHz}\}$ such that the θ that corresponds to the maximum energy is obtained at each observation snapshot of the time-series. Although it was observed that using any two vertically-offset elements of the array was sufficient to estimate the vessel's bearing, using all the elements of the array was found to yield results with the least error. Also, using all the elements eliminated the hard transition of the bearing when the vessel is closest to the array.

Summarily, the ML-BF has been applied to estimate the bearing of vessels from the CANAPE and ADEON data sets as they traveled in the ocean. The results from the CANAPE experiment are compared with the AIS data in Section 3.7.1. The CB-MFP algorithm that computes the range of the vessel to the array at the same discrete time intervals is described in Section 3.6.

3.6 Matched-field Processing

In this section, the CB-MFP algorithm is applied to estimate the depth and range of a source to a compact acoustic array. To this end, as described in chapter 1, the methodology used to compute the replica fields and the ambiguity surface that matches the source position is described next.

3.6.1 Computation of the Replica Fields

In an infinitely deep water column (without sediment boundaries), the displaced pressure field by a point source at $(0, z_s)$ can be evaluated using the superposition principle that yields

$$G_m(r, z) = S_w \frac{e^{ikR}}{4\pi R}. \tag{3.28}$$

In more realistic waveguides, specifically in shallow environments, the computation of the pressure field must include the boundary conditions of the reflected fields at the surface and bottom of the waveguide. To compute the pressure field at a receiver, two methods are often applied – the first, is the *image method*; and the second, is the *integral transform method*. The image method fundamentally depicts the physics of the propagation environment in an ideal waveguide. It relies on the fact that the multipath reflections due to the boundaries may be modelled by mirror effects of a perfectly reflecting boundary at the surface or at the basement (see Fig. (3.16)). Although, the method is not easily generalized to more complex propagation environments such as the Pekeris waveguide, to demonstrate the applicability of the systems design in this work, the image method is applied. The method is easy to implement and was found to reasonably capture the sound propagated by the vessels in the measurements.

The image solution describes a point source at depth z_s below the sea surface, where there are several possible reflected paths that the signals could travel before arriving at an array of receivers. For signals radiated by an acoustic source over range r to a receiver, the generalized source displacement from the integration of the Green's function for each propagated path is described in [6] by

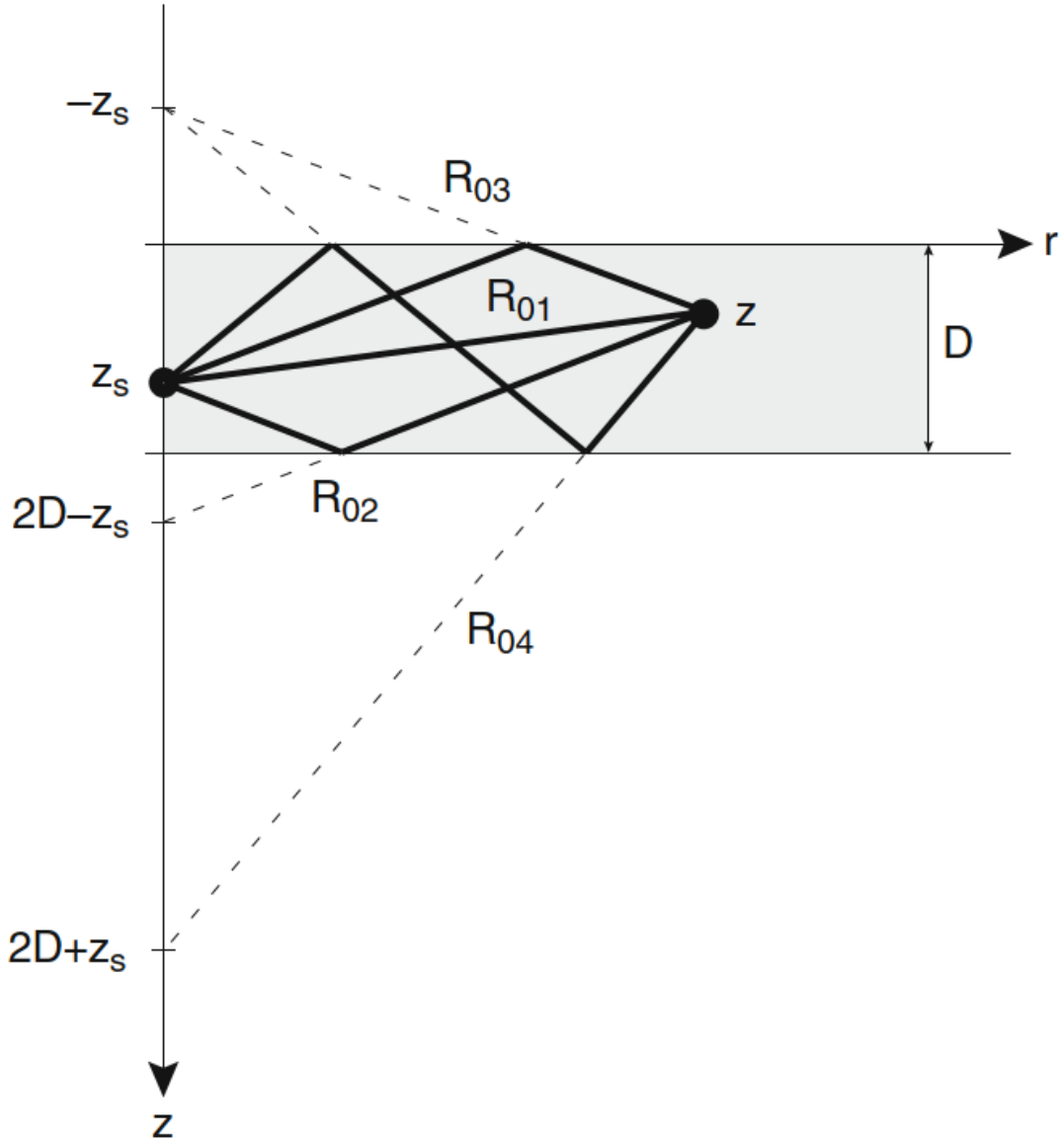

Figure 3.16: The image source solution showing the superposition of a line-of-sight path and the first three images of the source.

$$G_m(r,z) = \frac{S_w}{4\pi R}\sum_{m=0}^{\infty}\left[\frac{e^{ikR_{m1}}}{R_{m1}} - \frac{e^{ikR_{m2}}}{R_{m2}} - \frac{e^{ikR_{m3}}}{R_{m3}} + \frac{e^{ikR_{m4}}}{R_{m4}}\right], \tag{3.29}$$

where $R_{mn} = \sqrt{r^2 + z_{mn}^2}$ are the distances of the individual rays to the receiver and

$$
\begin{aligned}
z_{m1} &= 2Dm - z_s + z \\
z_{m2} &= 2D(m+1) - z_s - z \\
z_{m3} &= 2Dm + z_s + z \\
z_{m4} &= 2D(m+1) + z_s - z.
\end{aligned} \tag{3.30}
$$

D is the vertical depth of the duct and $m = 1, 2, \ldots, M$ propagation modes. Also, R_{m1} is the direct path (i.e. line-of-sight) and R_{m2}, R_{m3}, R_{m4} are the reflected paths representing the image paths at the m^{th} receiver.

In deep water columns, the model in (3.29) resolves to the well-known Lloyd's mirror solution

$$
G_m(r, z) = \frac{e^{ikR_{m1}}}{R_{m1}} - \frac{e^{ikR_{m2}}}{R_{m2}}, \tag{3.31}
$$

which represents the acoustic interference pattern created by a point source placed near a perfectly reflecting sea surface.

To estimate the source location, the usual approach in MFP is to match the spatial replicas with the measured acoustic pressure by computing the *ambiguity surface* of the propagation field.

3.6.2 The Ambiguity Surface

To estimate the source location, the general MFP approach matches the replica fields with the measured complex pressure field at the array by a generalized plane-wave beamformer. A very common approach is the Bartlett beamformer which is defined by

$$
B_{Bartlett}(s) = \mathbf{w}^H R_x \mathbf{w} \tag{3.32}
$$

where $B_{Bartlett}(s)$ is the ambiguity surface, R_x is the spatial correlation matrix and $s \in \{r, z\}$ represents the spatial domain (i.e. range and depth). The weighting vector $\mathbf{w}$ is computed as the spatial norm of the acoustic field replicas by

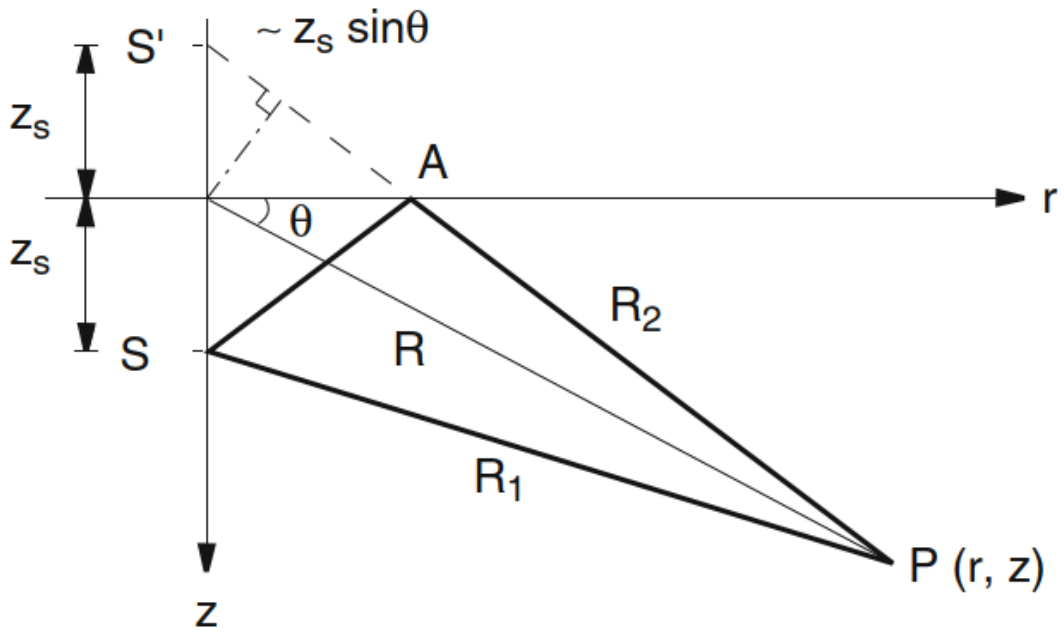

Figure 3.17: Geometry of surface image solution using the Lloyd-Mirror's interference pattern.

$$\mathbf{w} = \frac{G_m(r,z)}{|G_m(r,z)|}. \tag{3.33}$$

The peak of the ambiguity surface $B_{Bartlett}(s)$ matches the spatial position of the source. However, the ambiguity surface also contains ambiguous peaks which are similar to the sidelobes of a conventional plane-wave beamformer [6, 16]. In such scenarios, sidelobe suppression is often accomplished by using an adaptive beamformer such as the minimum variance beamformer

$$\mathbf{B}_{mvdr}(s) = [\mathbf{w}^H \mathbf{R}_x^{-1} \mathbf{w}]^{-1}. \tag{3.34}$$

There are, in fact, other beamforming methods developed to compute the ambiguity surface to match the true source position as accurately as possible. The sidelobes are majorly due to the fact that information about the ocean environment is often difficult to obtain and slight variations would lead to a mismatch of the ambiguity surface. Other factors are attributed to array tilt which introduces uncertainties in

the ambiguity surface. Different techniques have been investigated to address the mismatch problem [**?**, **?**]. In recent times, state-of-the-art deep neural-networks have been applied for localization problems with successes [**?**, **?**]. For instance, the recent work in [**?**, **?**] showed the successes of deep learning methods for ship classification and detection via acoustic signatures. More pertinently, the work in [**?**] addresses a problem similar to that in this work by applying the deep learning framework.

However, deep learning models are not robust to noisy data. Their success in computer vision is attributed to the quasi-absence of noise in the data set. In a recent work [**?**], it was recognized that noise-induced perturbation in the data set would lead to a complete failure of deep learning models.

Most efforts in literature, maintain the concept of matching the measured data to the solutions or partial solutions of the wave equation as the central theme, though different algorithms to compute the ambiguity surface are applied. The uniqueness in the MFP algorithm developed in this dissertation is in matching the spatial coherence of the measured data to the coherence of the replica fields. This approach does not generate the sidelobe problems that are often encountered in the plane-wave beamforming techniques.

3.6.3 Coherence based Matched-field Processing

The CB-MFP relies on the estimates of coherent interference pattern of signals measured at the elements of an array. The coherence-ranging method was recently applied to estimate the range of a vessel in [**?**]. This method computes the normalized CSD of the measured data and that of the spatial field replicas of the range-depth grid. The well-known generalized expression for estimating spatial coherence in OAN fields is [4]

$$\Gamma_{xy} = \frac{\overline{S_{xy}}}{\sqrt{\overline{S_{xx}}\ \overline{S_{yy}}}}, \tag{3.35}$$

where $\overline{S_{xy}}$ is the CSD between the spatially separated sensors x and y, $\overline{S_{xx}}$ and $\overline{S_{yy}}$ are the PSD at each receiver, and the overbar denotes the ensemble average. Thus, Γ_{xy} is computed from the measured acoustic data at pairs of sensors while the estimate of the coherence computed from the spatial replicas from either (3.29) or (3.31), or

any other model of the acoustic propagation field is expressed as

$$\Gamma_{xy}(r_K, z_D) = \frac{\overline{G_{xy}}(r_K, z_D)}{\sqrt{\overline{G_{xx}}(r_K, z_D)\ \overline{G_{yy}}(r_K, z_D)}}, \tag{3.36}$$

where $G_{xy}(r_K, z_D)$ represents the spatial replicas of acoustic field at sensor x, y. $\Gamma_{xy}(r_K, z_D)$ is computed with respect to the spatial dimension $s \in \{r_K, z_D\}$ and $\{K, D\}$ represent the maximum search grid points in range and depth respectively. The coherence grid that is similar to the ambiguity surface is computed at all the discrete spatial points in range and depth such that

$$\hat{\mathbf{\Gamma}}_{xy}(r, z) = \begin{bmatrix} \Gamma_{xy}(r_1, z_1) & \Gamma_{xy}(r_2, z_1) & \dots & \Gamma_{xy}(r_K, z_1) \\ \Gamma_{xy}(r_1, z_2) & \Gamma_{xy}(r_2, z_2) & \dots & \Gamma_{xy}(r_K, z_2) \\ \vdots & \vdots & \ddots & \vdots \\ \Gamma_{xy}(r_1, z_D) & \Gamma_{xy}(r_2, z_D) & \dots & \Gamma_{xy}(r_K, z_D) \end{bmatrix}. \tag{3.37}$$

It is expected that the coherence functions between adjacent pairs of the elements of an array will be the same i.e. $\hat{\mathbf{\Gamma}}_{12}(r, z) = \hat{\mathbf{\Gamma}}_{23}(r, z) =, \dots, = \hat{\mathbf{\Gamma}}_{xy}(r, z)$, such that $(M-2)\hat{\mathbf{\Gamma}}_{xy}(r, z) = \hat{\mathbf{\Gamma}}_{12}(r, z) + \hat{\mathbf{\Gamma}}_{23}(r, z) +, \dots, +\hat{\mathbf{\Gamma}}_{(M-1)M}(r, z)$ when applying the model in 4.5. Similarly, Γ_{xy} is expected to be uniform across the array. However, uncertainties due to array tilt could impact the integration of the empirical spatial coherence at pairs of the hydrophones. Thus, in this work, any pair of sensors is sufficient to estimate the spatial location of the acoustic source in CANAPE and the two-element VLA is applied in ADEON.

The estimate of the source location is obtained by computing the root-mean-square error (RMSE) between all the computed range-depth coherence functions $\hat{\mathbf{\Gamma}}_{xy}(r, z)$ and the empirical coherence Γ_{xy} at discrete spatial snapshots. Similar to the spectral matrix discussed in Section 3.5, the measured acoustic data is divided into K snapshots, so that the estimates of the range are computed over $k = 1, \dots, K$ discrete time and the snapshot at k occupies ΔT duration. This implies that Γ_{xy} is computed over K snapshots which is also equivalent to the discrete intervals in range $\{r_k \in r_1, \dots, r_K\}$ at the replica fields, so that the instantaneous range estimate is

$$r_k(\omega) = \arg\min_r \left\{ \sqrt{\frac{1}{K}\sum_{k=0}^{K}\left(\hat{\mathbf{\Gamma}}_{xy}(r,z) - \Gamma_{xy}(k)\right)^2} \right\}, \tag{3.38}$$

and the instantaneous source depth is obtained from

$$z_k(\omega) = \arg\min_z \left\{ \sqrt{\frac{1}{K}\sum_{k=0}^{K}\left(\hat{\mathbf{\Gamma}}_{xy}(r,z) - \Gamma_{xy}(k)\right)^2} \right\}, \tag{3.39}$$

where ω denotes that the estimates of the range and depth are computed over the measurement bandwidth at each snapshot k.

Note that, the source depth $z_s(\omega) \approx \frac{1}{K}\sum z_K(\omega)$, since the instantaneous depth of a vessel is relatively constant. In fact, to estimate s_z, K can be limited to a few snapshots, but the source range $r_K(\omega)$ is estimated over the K snapshots.

3.6.4 Range Estimation Results

The results shown in this section are computed from the measured acoustic pressure from the CANAPE and the ADEON measurements. The instantaneous source depth $z_k(\omega)$ is computed over a few snapshots and averaged to obtain $z_s(\omega)$. To estimate the range of the vessel with respect to time, the theoretical vertical coherence between pairs of sensors was computed from (3.36) for which the spatial replicas are modeled from the Lloyd-mirror's pattern in (3.31). The empirical coherence is computed at pairs of sensors from (3.35). It is expected that in certain environments, either (3.29) or (3.31) will be sufficient to match the interference pattern to the source position. In other environments with depth-dependent sound speed, other propagation models will be required to match the specific interference patterns of the water column.

CANAPE Range Results

Fig. 3.18 shows the real and the imaginary coherence computed from the replica fields representing CANAPE's measurement environment.

Similarly, Fig. 3.19 shows the interference pattern of the coherence computed from the acoustic measurement from the CANAPE experiment. To be able to capture the full interference pattern, the coherence is computed over $B_C = \{10, 800 \text{ kHz}\}$. The bandwidth that corresponds to the sonars is removed manually to avoid inaccurate

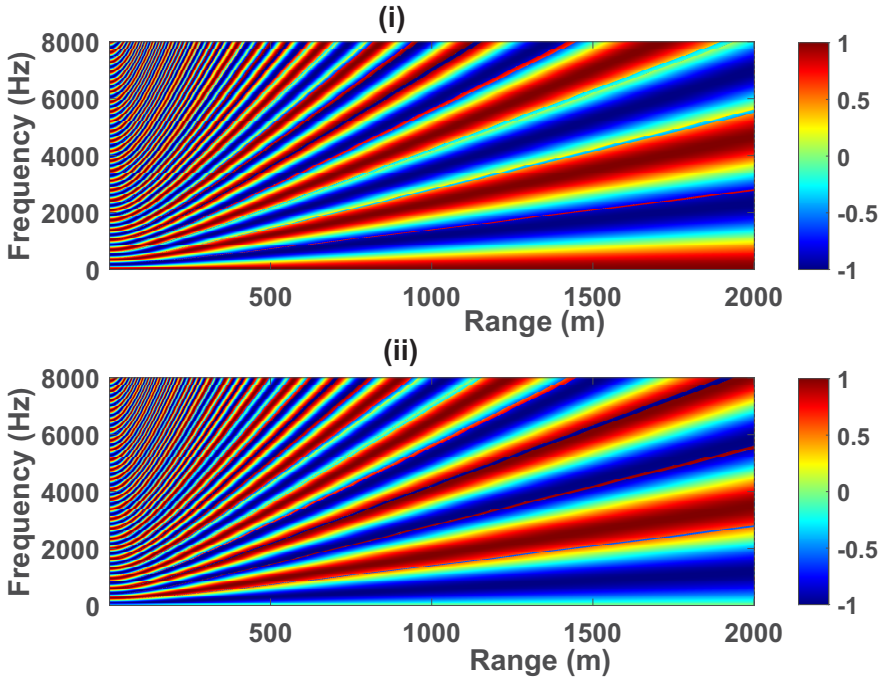

Figure 3.18: The ambiguity surface representing the coherence of the replica fields in CANAPE. (i) $\Longrightarrow$ the real coherence; (ii) $\Longrightarrow$ the imaginary coherence.

estimates of the range. Fig. 3.18 and Fig. 3.19 indicate that there is a relationship between the range of the vessel and travel time of the vessel. This is evident in that the vessel covers distance with respect to time.

Furthermore, the source depth is estimated by the depth dimension of the LUT of the ambiguity surface in (3.37). The depth dimension of the LUT simply implies that the replica fields are computed over all the possible depths of the vessel. It is observed that the average depth of the vessel was about 3.6ft.

Fig. 3.21 shows the range estimation result from (3.38). It is observed that the range of the vessel could be estimated over about 1800 meters accurately, after which the estimate deteriorates significantly. The range also compares with a 6-minute travel duration of the vessel. This suggests that the vessel travels at a moderately slow speed.

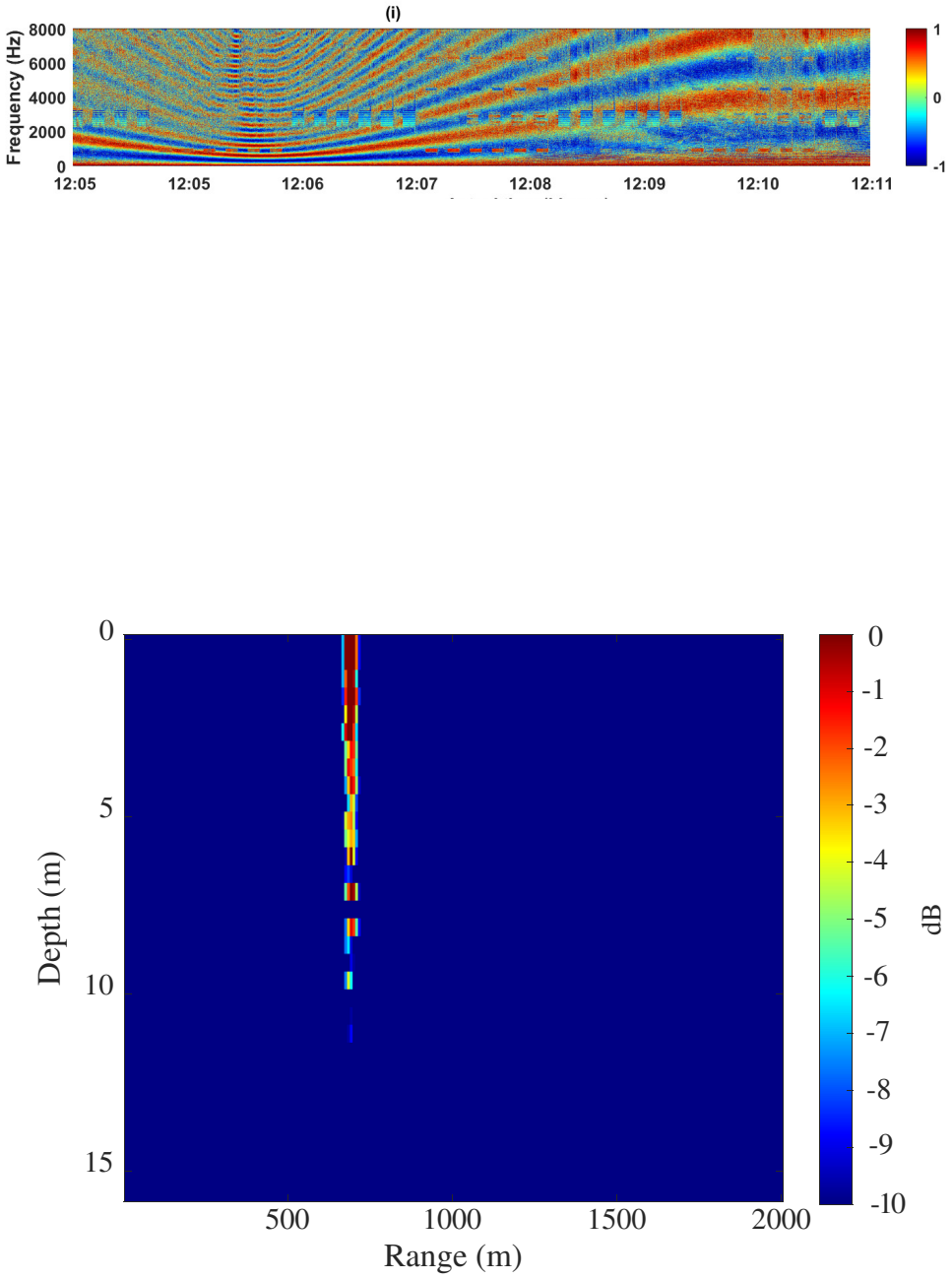

Figure 3.20: A snapshot estimate of the vessel depth computed from the coherence ambiguity surface whose look-up table is computed as a function of depth.

ADEON Range Results

The replica field is computed from the image-source model in (3.31). Different combinations of the elements of the array were used to compute the empirical coherence. It is observed that unlike the vertical elements in CANAPE, the vertical elements in

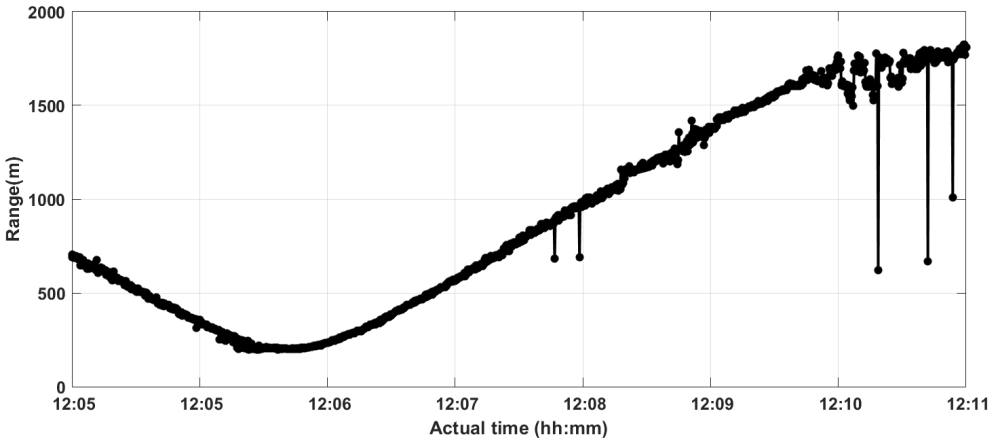

Figure 3.21: Track of the vessel with respect to time, measured from the CANAPE experiment.

ADEON do no capture a robust interference pattern. Fig. 3.22 shows the coherence estimated at the vertical elements 3 and 4 of the ADEON array.

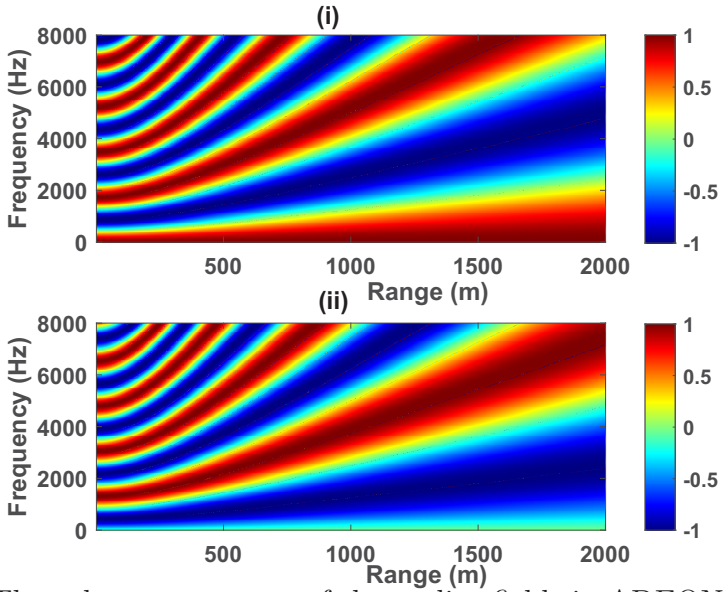

Figure 3.22: The coherence pattern of the replica fields in ADEON. (i) $\Longrightarrow$ the real coherence; (ii) $\Longrightarrow$ the imaginary coherence.

Fig. 3.23 shows the empirical coherence computed from ADEON's data set. It is observed that the coherence pattern does not capture an interference pattern that will accurately estimate the range of the vessel. Also, from Fig. 3.22 and Fig. 3.23, it is observed that the interference pattern of the replica fields do not compare with

the empirical interference pattern. This difference in the coherence based ambiguity surface limits the range estimation from the ADEON data set.

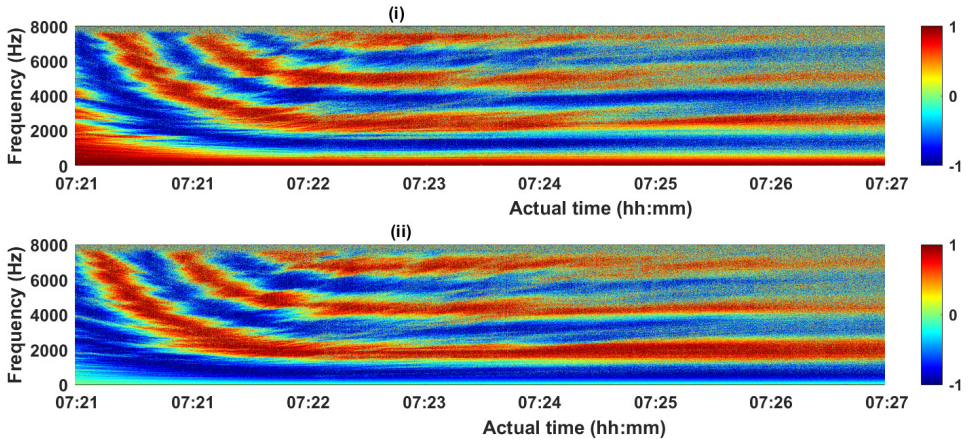

Figure 3.23: The coherence computed from the measured complex pressure field from the ADEON experiment. (i) $\Longrightarrow$ the real coherence; (ii) $\Longrightarrow$ the imaginary coherence.

From Fig. 3.24, there is more difficulty with computing the range of the vessel with great accuracy from the ADEON experiment. The range estimates from CANAPE and ADEON indicate that the accuracy of the CB-MFP depends on the accurate computation of the replica fields, as well as the interference pattern of the acoustic field measured at the array. It is also observed that the wider aperture in CANAPE captures more interference pattern than the shorter aperture in ADEON.

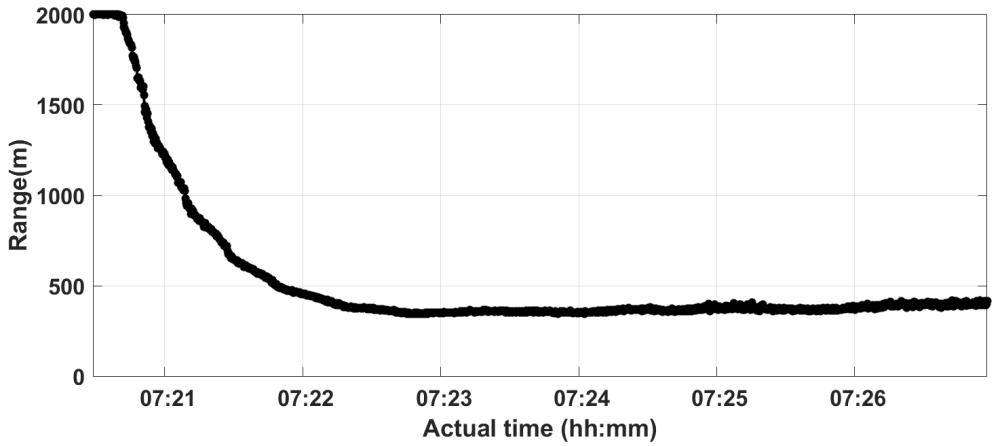

Figure 3.24: Track of the vessel with respect to time, measured from the ADEON experiment.

Having established that the ADEON array limits the range estimation described in this section, the rest of this chapter focuses strictly on the results obtained from the CANAPE experiment to characterize the position of the vessel as a function of time.

Just as in most source tracking algorithms, the implementation of the algorithms described thus far shows some estimation noise, although minimal, for both the directionality from Section 3.5 and the range estimates from the coherence MFP in Section 3.6. To estimate the position of the vessel accurately, a Kalman filter discussed in Section 3.7 is implemented to mitigate the estimation noise.

3.7 Kalman Filtering

In this section, the Kalman filter is demonstrated as a solution to remove the estimation noise in the vessel's position.

The Kalman filter (KF) algorithm is a unique case of the optimal linear filter that has been applied extensively in aerospace [**?**] and navigation [**?**], where a signal trajectory must be well defined. The KF uses a set of dynamic state-space model of a system to recursively update the input data that contains random errors or uncertainties [2]. The recursive equations make the KF suitable for online applications where the actual state of a system needs to be accurately predicted by observations that are measured sequentially.

The equation of motion that relates the current position X_t with the prior state X_{t-1} of the vessel can be expressed as

$$X_t = X_{t-1} + v_{t-1}t + \frac{1}{2}a_t t^2. \tag{3.40}$$

where a_t and v_t are the instantaneous acceleration and velocity of the vessel respectively, at time index t. Note that X_t is the vector that contains vessel's state which is different from the spatially sampled signal $\mathbf{X}_k(\omega)$ used in Section 3.5.

It is noteworthy that (3.40) is an equation in the Cartesian coordinate, however, the measured state of the vessel (characterized by the range and bearing) is defined in the polar coordinate. There are several conversion methods that have been proposed in literature to convert the state of a system from polar to the Cartesian coordinate

so that the KF equations can be applied. A conventional conversion technique [**?**] is applied in this work. Hence, the measured position of the vessel in the polar coordinates can be transformed into the Cartesian coordinates by

$$\begin{aligned} x_t &= r_t \cos\theta_t \\ y_t &= r_t \sin\theta_t. \end{aligned} \tag{3.41}$$

The equations that describe the KF are described in [2, **?**]. There are two important aspects of the KF: 1) the theoretical prediction of the state of the system or process; and 2) the measurement update which involves the correction of the measured state of the system.

The recursive matrix equation that characterizes the KF prediction update is [2]

$$X_t = \mathbf{A}X_{t-1} + \mathbf{B}u_{t-1} + \phi, \tag{3.42}$$

where $\mathbf{A}$ is the state transition matrix applied to the previous state matrix X_{t-1}, $\mathbf{B}$ is the control input matrix applied to the state control matrix U_{t-1}, and Φ is the error term in the state prediction with a known covariance matrix whose elements are computed from

$$\begin{aligned} \Phi^{11} &= r_t^2\sigma_\theta^2 \sin^2\theta_t + \sigma_r^2 \cos\theta_t \\ \Phi^{22} &= r_t^2\sigma_\theta^2 \cos^2\theta_t + \sigma_r^2 \sin^2\theta_t \\ \Phi^{12} &= \Phi^{21} = (\sigma_r^2 - r_t^2\sigma_\theta^2)\sin\theta_t\cos\theta_t, \end{aligned} \tag{3.43}$$

where σ_r and σ_θ are the variances in range and in bearing, respectively. The update for the error covariance matrix in the prediction state is expressed as

$$P_t = AP_{t-1}A^T + Q_t, \tag{3.44}$$

where Q_t is the noise covariance matrix introduced at each state of the prediction. Q_t is assumed to be of constant values at all the states.

In the measurement update portion of the KF process, the measured (or the

computed) state of the vessel $S_t = [x_t, y_t]^T$ in the Cartesian coordinate is related to the predicted state estimate by

$$V_t = S_t - HX_t. \tag{3.45}$$

The KF update relies on the efficient computation of the KF gain

$$K_t = P_t H^T (HP_t H^T + \Phi)^{-1}. \tag{3.46}$$

Also, the measurement update that weighs the level of accuracy in the predicted state estimate X_t and compares it with the sensor prediction is

$$\hat{S}_t = X_t + K_t V_t, \tag{3.47}$$

where H, C are the adaptation matrices introduced to ensure the dimensions of the state matrices are consistent. Thus, $\hat{S}_t$ is the true state estimate of the vessel from the KF filtering.

Finally, the estimate of the true position of the vessel can be converted back to the polar domain, so that r'_K and θ'_K are the estimated true range and bearing of the vessel.A methodology is described in Section 3.7.1 to represent the range and the bearing of the vessel in longitude and latitude values.

Kalman Filtered Results and Discussion

Fig. 3.25 and Fig. 3.26 show that the uncertainties introduced in the bearing and range from the system design in this work can be filtered using a KF. Although other robust particle filtering algorithms have been derived in literature, the KF used in this work is a sufficient solution to track the vessel for demonstration purposes. It is suggested that in other harsh environments with more estimation noise, other particle filtering methods may be explored.

Finally, in order to compare the instantaneous position of the vessel measured at the acoustic array with the AIS data reported on the vessel, a methodology is described in Section 3.7.1 to represent these distances in longitude and latitude values.

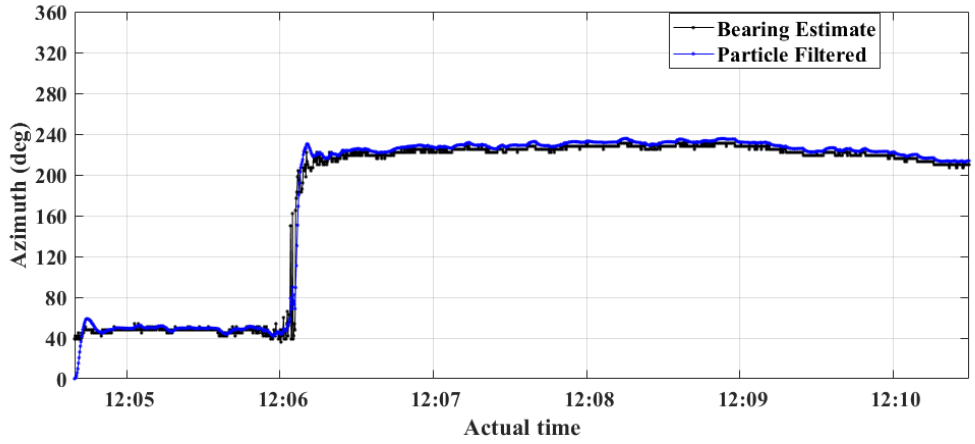

Figure 3.25: Particle filtered bearing versus travel time of the vessel measured from the CANAPE experiment.

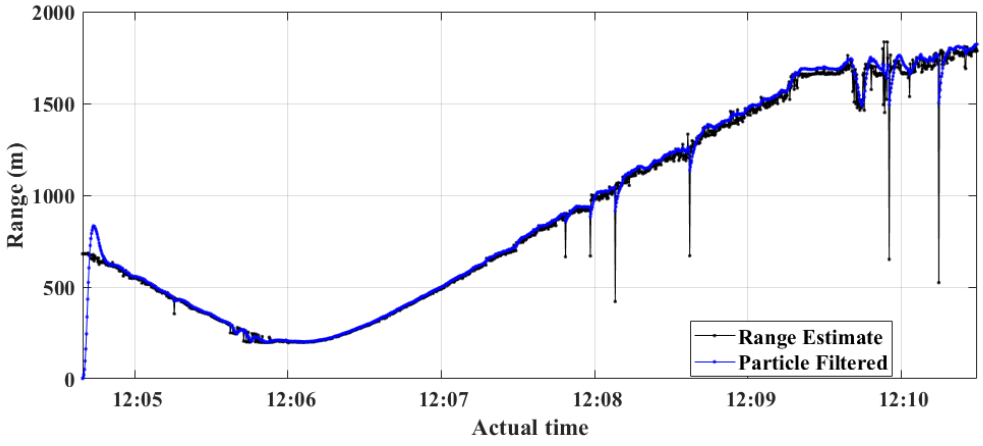

Figure 3.26: Particle filtered range of the vessel computed from the CB-MFP for the measured data from the CANAPE experiment.

3.7.1 Estimation of Source Position

In this section, the estimates of the range r'_K and bearing θ'_K of vessel at the spatial snapshots are converted to distances on the great circle so that the vessel's position can be represented on a geographical map. The determination of great circle distances are often applied in great-circle navigation problems [2], which also computes the azimuths and intermediate way-points. The goal of this section is to be able to represent the instantaneous position of the vessel in latitude and longitude values.

First, the range estimates are converted to arc lengths on a great circle from

$$d_K = \frac{180 r'_K}{\pi R} \tag{3.48}$$

where $R = 6371000$ meters is the radius of the earth. To estimate the position i.e. the latitude γ and longitude λ of the vessel to the array at position $\{\gamma_0, \lambda_0\}$, the expression that relates the source bearing θ to a given arc distance [**?**] yields

$$\lambda_K = \lambda_0 + \arctan\left[\frac{\sin d_K \sin \theta'_K}{(\cos\gamma_0 \cos d_K - \sin\gamma_0 \sin d_K \cos\theta'_K)}\right] \tag{3.49}$$

and

$$\gamma_K = \arcsin(\sin\gamma_0 \cos d_K + \cos\gamma_0 \sin d_K \cos\theta'_K). \tag{3.50}$$

In this design, the estimates of $\{\lambda_K, \gamma_K\}$ are computed over the K snapshots and compared to historical AIS data obtained from Marine Traffic[3] for the same vessel in the CANAPE measurement. Note that (3.49) and (3.50) can be inverted so that if the source position is given in latitude and longitude, the values can be converted to distances in meters. A detailed derivation is developed in [**?**].

Using the historical AIS data, the reported vessel that was tracked is confirmed to be the Sikulaq, a research vessel with AIS ID number 400622. Three timestamps at TS_1 = 11h19, TS_2 11h21 and TS_3 = 11h24 on October 24, 2016 are depicted in Fig. 3.27. The AIS and the acoustic estimates are interpolated over about a 40 minutes interval i.e 11h24 (from the AIS) and 12h05 (from the acoustics measurement). Note

[2] Great-circle navigation or orthodromic navigation is the practice of navigating a vessel or aircraft along a great circle. These routes yield the shortest possible distance between two points on the globe.

[3] www.marinetraffic.com

that the start and stop time of the acoustic estimate are 12h05 and 12h11 respectively.

Using the AIS information, the approximate range of the vessel at the three timestamps are respectively $R_1 = 8.2$ km, $R_2 =$ 7.6 km, and $R_3 = 6.9$ km. This suggests that the vessel traveled an average of 1km within the 3-minute interval. Similarly, the range estimates from Fig. 3.26 shows that the vessel traveled over about 2km in the 6-minute duration of the acoustic measurement.

Unfortunately, there is not enough AIS data to confirm the resolution of the localization algorithm. Nonetheless, from the geographical plot, it is observed that the vessel indeed travels in close proximity to the array around the 12h06 timestamp. At close proximity, the bearing estimates from the acoustic measurement become inaccurate due to the hard transition in the bearing estimates, and an optimization technique needs to be developed to achieve beamforming accuracy.

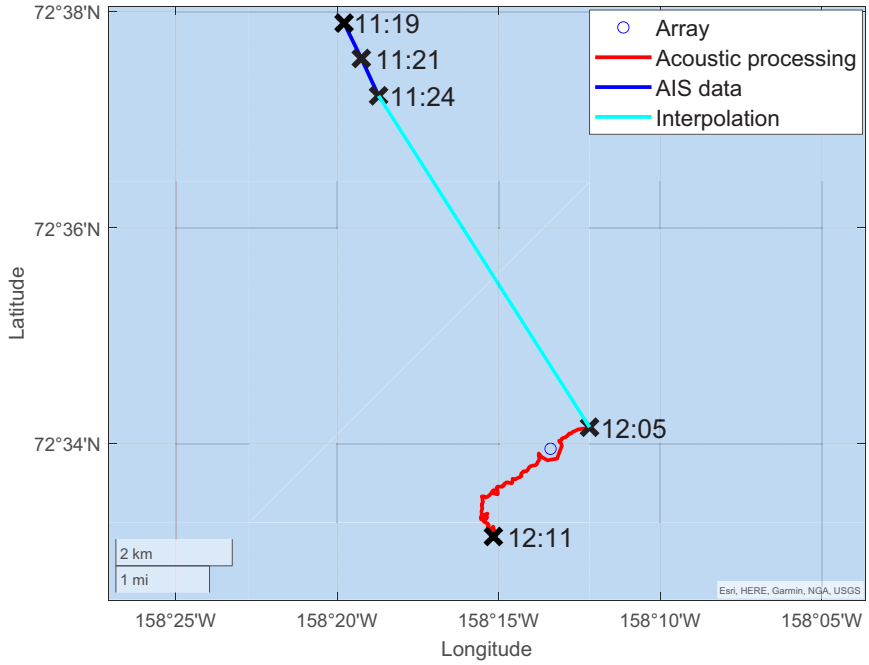

Figure 3.27: The geographical plot of the position of the vessel, compared with the AIS data for the vessel detected during the CANAPE experiment.

To summarize this chapter, first, the acoustic signature can be used on a passive sensor array to track a vessel, and in this work, a stable bearing and range estimate was obtained over relatively long ranges up to about 2 km. The performance of the

algorithm depends on the array geometry and deployment depth. The array aperture must capture multiple wavelengths in the dominant bandwidth to achieve accuracy in the CB-MFP. Second, vessel noise is directional and can be used to track a moving platform.

The bearing and range estimation algorithms described in this chapter can be optimized for varying ocean conditions using more accurate models of the propagation environment, especially in layered media. Because the sensor array geometry is relatively compact, it can be deployed on autonomous platforms for real time tracking of vessels within a few kilometers for different use cases.

Conclusively, this chapter has focused on characterizing the directionality of transient vessel noise, and in Chapter 4 models of directional noise will be developed. While this demonstrates that shipping noise is directional, the impact of such directional noise sources on the communication link will be shown in Chapter 5.

Chapter 4

Space-time Synthesis of Ocean Ambient Noise

In this chapter, the space-time characteristics of naturally occurring OAN are discussed. In the design of acoustic receivers, the white Gaussian noise assumption may be attributed to the fact that existing noise models are either too involved and often not developed for engineering applications, or they are not particularly representative of the environment of interest. Therefore, it is desirable to develop a low-complexity model that generates synthetic space-time ambient noise and that is applicable for signal detection underwater. To achieve this objective, first, a methodology is described for modeling space-time OAN process measured at a compact array of hydrophones over wide bandwidths and validated against well established ambient noise models.

To this end, first, a step-wise implementation for two different methodologies that characterize the spatial properties of ambient noise processes over a multi-element compact VLA is presented. Second, an AR model that characterizes the temporal property is also presented. Third, the unique properties of ambient noise in narrowband conditions are characterized and compared with the usual white Gaussian noise assumption about OAN in UWAC.

The contributions in this chapter are in two folds. First, noise models are developed that are able to match the specific properties of a noise measurement environment. Second, the unique spectrum of ambient noise even in narrowband conditions is demonstrated.

Therefore, in Section 4.1, some fundamental work in modeling OAN is briefly reviewed. In Section 4.2, the noise measurements that are used to validate the properties of the noise models developed in this chapter are described. In Section 4.3, the two methodologies that are developed for synthesizing the spatial properties of OAN are described. In Section 4.4, the spectral properties of the synthetic ambient noise process are developed. In Section 4.5, the unique characteristic of ambient noise

in over a narrow bandwidth is demonstrated. Finally, in Section 4.6, the instantaneous temporal variability in the directionality of naturally occurring ambient noise is described.

4.1 Background of Ambient Noise Modeling

In pioneering work on OAN [5, 4], analytical expressions were presented to characterize the spatial correlation function for isotropic (volume) and surface noise sources. In [5], the authors noted that for isotropic noise characterized by point sources with invariant power over all distribution angles, as the noise sphere radius approaches infinity, the normalized cross-spectral density (CSD), or the coherence Γ_{yz} between two sensors $\{y, z\}$ physically separated by a distance d, can be expressed as

$$\Gamma_{yz} = \frac{\sin(kd)}{kd} \tag{4.1}$$

where k is the wavenumber of the incoming plane waves. A closed form expression was found for the vertical coherence of surface noise sources due to wind generated breaking waves, which are represented as directional point sources distributed over the planar surface. For a two-element vertical array in an infinitely deep isovelocity ocean, the correlation was described as

$$\Gamma_{yz} = 2\left[\frac{\sin(kd)}{kd} + \frac{\cos(kd)}{kd}\right]. \tag{4.2}$$

Cox [4] characterized these noise fields in terms of a directionality function, by placing angular dependent weighting factors over the plane waves arriving from all directions. For a noise field measured at sensors y and z, the coherence is computed from (3.35).

In [**?**], a generalized model for surface generated noise which characterizes the CSD (using the Green's function) between the noise sources and the receiver is described. The coherence expression for vertically separated sensors in surface generated noise is

$$\Gamma_{yz} = \frac{\int_0^\infty q\ G_{yq}G_{zq}^* dq}{[\int_0^\infty q|G_{yq}|^2 dq \int_0^\infty q|G_{zq}|^2 dq]^{1/2}} \tag{4.3}$$

where G_{yq} and G_{zq} are the Hankle transformed Green's functions and the solutions to the depth-dependent wave equation between a source placed at a depth z_s and the two receivers, respectively, and q is the complex horizontal wavenumber. This expression allows the vertical noise coherence in an arbitrary environment to be computed, so long as the Green's function itself may be computed.

To evaluate the integral in (4.3) for the case of the two receivers in an isovelocity water column overlying a homogeneous bottom boundary (a Pekeris waveguide), a closed form integral solution can be utilized to numerically evaluate the transformed Green's function at the m^{th} (where m is equal to y or z) sensor as

$$G_{mq} = C\frac{\sin\eta_1 z_s}{\eta_1}\left\{\frac{(\eta_1+b\eta_2)\exp[j\eta_1 z_m]+(\eta_1-b\eta_2)\exp[j\eta_1(2h-z_m)]}{(\eta_1+b\eta_2)+(\eta_1-b\eta_2)\exp[2j\eta_1 h]}\right\}, \tag{4.4}$$

where C is a scaling constant, h is the depth of the water column, z_m is the depth of the m^{th} sensor, η_1 and η_2 are the vertical wave numbers in water and sediment, respectively, c_1 and c_2 represent the sound speed of water and the sound speed of the sediment, respectively, and b is the ratio of densities in the seabed and water column.

In an infinitely deep water column, the noise field can be evaluated directly by first computing the (untransformed) Green's function between a single surface point source and receiver using the image source method [6]

$$G_m = \frac{e^{ikR_{m_1}}}{R_{m_1}} - \frac{e^{ikR_{m_2}}}{R_{m_2}}, \tag{4.5}$$

where R_{m_1} is the direct path and R_{m_2} is the surface reflected waves arriving at the m^{th} receiver. Assuming azimuthal symmetry with the receivers placed at the origin, the noise CSD and PSD are then computed by integrating over the infinite sheet of surface sources, giving an expression for the vertical noise coherence

$$\Gamma_{yz} = \frac{\int_0^\infty r\ G_y G_z^* dr}{[\int_0^\infty r|G_y|^2 dr \int_0^\infty q|G_z|^2 dr]^{1/2}} \tag{4.6}$$

where r is the horizontal coordinate. The result is exactly consistent with Cron & Sherman's expression given in (4.2). The well-known background knowledge about ambient noise fields have been described thus far in this section.

In more recent times, several authors have demonstrated the impact of impulsive

OAN on underwater acoustic receivers while some authors have suggested that even the non-impulsive sources need to be investigated. Generally, these authors have simply represent these noise sources as being of a colored spectrum. Although it has been showed that OAN is generally of a colored spectrum [1], this representation is still far from accurately capturing all the characteristics of OAN. To the best of the author's knowledge, there is no work in literature that has strictly examined the impact of naturally occurring OAN on an underwater acoustic receiver neither are there models that can easily be applied to characterize OAN in the design of UWAC receivers. This chapter describes a model for OAN by describing its spatial and spectral characteristics and compares them with actual ambient noise measurements. The noise measurement scenarios are described next.

4.2 Noise Measurement Scenarios

In this section, two measurement scenarios are presented and used to characterize the noise in an underwater communication link.

In the Summer of 2017, a 3-day sea trial (Dalcomm1) was run 10 kilometers off the coast of Nova Scotia between the entrances to Halifax harbour and St. Margaret's Bay in a water depth of 80 meters. A multichannel autonomous recorder (Turbulent Research ORCA) with a five-element vertical line array (VLA) consisting of omnidirectional hydrophones with an acoustic bandwidth of 1 Hz-120 kHz was at mid-column - about 40 m below the surface as depicted in Fig. 4.2. The receiver sampling frequency was 10.24 kHz.

Recall that some results detailing the CIR from DalComm1 were briefly introduced in Chapter 2. The specific objectives of DalComm1 are in two folds. The first objective was to characterize the propagation channel for medium to ling-range UWAC in a point-to-point link and correlate the channel with oceanographic conditions. The second objective was to evaluate the reliability of some novel acoustic communication techniques.

A database of the communication waveforms were stored on a transmit laptop. The waveforms were amplified to the appropriate levels and applied to the transmit projector. The transmit signals were OFDM modulated symbols, frequency shift keying (FSK) symbols and a chirp signal.

During this period, the acoustic data were recorded and various communication experiments were run to characterize the channel and estimate the performance of a narrowband acoustic communication link with a center frequency of 2 kHz. The data transmission during these experiments were measured at 1 km, 2 km, 4 km, 8 km, 10 km, so that the propagation channel can be characterized by post-processing the data.

Four different experimental setup were completed in DalComm1 to achieve the aforementioned objectives. First, the time-varying UWA channel properties were characterized. Second, a spread-spectrum modulation technique was evaluated using a chirp signal. Third, the Doppler compensation was also evaluated in coherent communication systems. Finally, the performance of an adaptive equalization algorithm was evaluated. The evaluation of the adaptive equalization algorithm is applicable to this dissertation and discussed in greater details in the rest of this chapter.

To evaluate the CIR as a function of time, two types of acoustic waveforms were transmitted – a linear FM sweep (or chirp) used to characterize the channel even in the presence of Doppler, and a maximum length (ML) sequence which is often used in spread-spectrum communication.

The chirp signal spans over a 300 Hz bandwidth and a duration of 0.5 seconds. To extract multiple successive CIR, 1024 successive chirps were transmitted to last a duration of 8:30 minutes. Also, the ML sequence consisting of 512 bits were transmitted at a rate of $R - b = 240$ symbols per second, to allow the characterization of the channel with a maximum excess delay of 2.1 seconds and a processing gain of 24 dB. At the transmission rate R_b, the path arrival resolution is $1/R_b = 4.1$ms. In each sound file, multiple ML sequences are concatenated to extract 256 successive CIR, so that each sound file lasts 9:06 minutes.

The ambiguity functions representing the chirp and the maximum length sequence are depicted in Fig. 4.1. Although the ML sequence cross-correlation deteriorates even at very low Doppler shifts, the sequence is chosen because it is representative of constant envelop coherent modulation schemes, and as such, is a natural fit for the data frame.

While the chirp ambiguity function decays with delay to values on the order of 40 dB, that of the ML-sequence remains at a much higher noise floor on the order

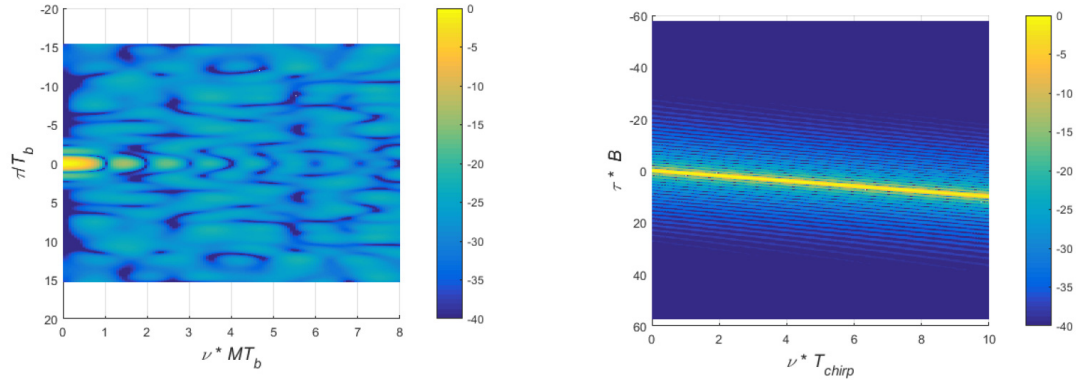

(a) A 320 Hz, 0.4 second chirp. (b) A 512 psuedo-random noise sequence.

Figure 4.1: Ambiguity functions for channel characterization in DalComm1.

of -25 dB below the maximum peak. One disadvantage of the chirp is that the auto-correlation as a function of delay contains ripples with high amplitude close to the main tap delay. This can introduce imprecision in the CIR. For this purpose, the channel statistics obtained using the two signatures are analyzed carefully to obtain complementary information. After post-processing, the CIR obtained from the ML sequence were shown and discussed earlier in Fig. 2.6, while readers are referred to [**?**] for the CIR from the chirp signal as well as other post-processing results.

Further, the ambient noise was measured throughout the experiment to accurately characterize the communication links. Details of the acoustic source, the receivers, the water column and some initial post-processed results are described in [19, 20, **?**].

The geoacoustic parameters of the DalComm1's measurement site were derived from the bottom composition provided by the Canadian Hydrographic Services (CHS) [21] at the Department of Fisheries and Oceans Canada using a survey of previously published data [7]. The DalComm1 site's bottom is characterized by a rocky and coarse sand with a sound-speed of 1560 m/s and a mean column sound speed of 1482 m/s [**?**].

The second data set used to characterize the properties of ambient noise in this chapter are derived from the CANAPE measurements described in Section3.3. Specifically, the acoustic pressure measured at the 3-element VLA during the open water (ice free) period, in the month of October, were selected for analysis. Also, there were no vessels present in the portion of the data analyzed in this section, such that it can be assumed that the overall noise is surface generated. The geoacoustic values

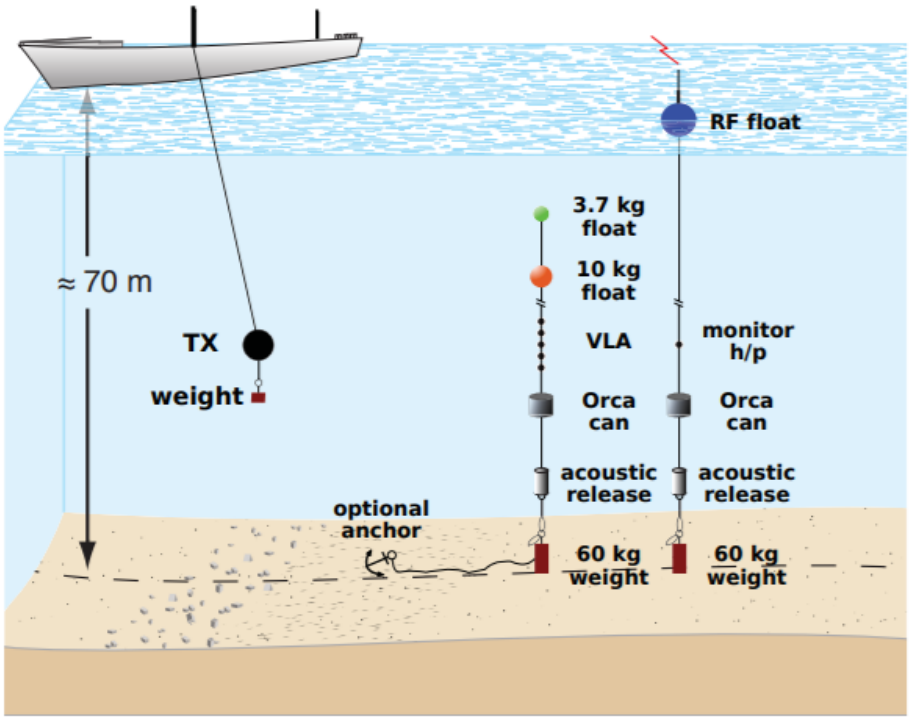

Figure 4.2: DalComm1 deployment scenario.

of the sediment were provided by JASCO and agreed with the results determined by searching for the best match, in a root-mean square error sense, between the measured and modelled noise coherence given by (4.4). The derived geoacoustic parameters for both experiments are summarized in Table 4.1.

Measurement location	**DalComm1**	**Canape**
Position (Latitude, Longitude)	$44°30'00.0"N, 63°24'00.0"W$	$72°33'57.2"N, 158°13'23.9"W$
Water depth (m)	80	149
Sediment type	Coarse sand	Clayey silt
Sediment sound speed, (m/s)	1560	1550
Sediment density, (kg/m^3)	3705	1429
Column sound speed, (m/s)	1482	1453
Mean sensor depth (m)	40	125.25
Loss tangent $\beta = 1/2Q$[1]	0.0156	0.0156

Table 4.1: Environmental parameters at the DalComm1 and Canape measurement sites

From Fig. 4.3, it is observed that both DalComm1 and CANAPE mean noise PSDs over the array have significant contributions from about $500 - 4000$ Hz which are representative of surface generated noise. In DalComm1, noise is relatively strong

at low frequency, and as will be demonstrated in Section 4.3 it has low correlation over space. Further discussions about the coherence analysis and its importance in generating a synthetic ambient noise process is described in Section 4.3.

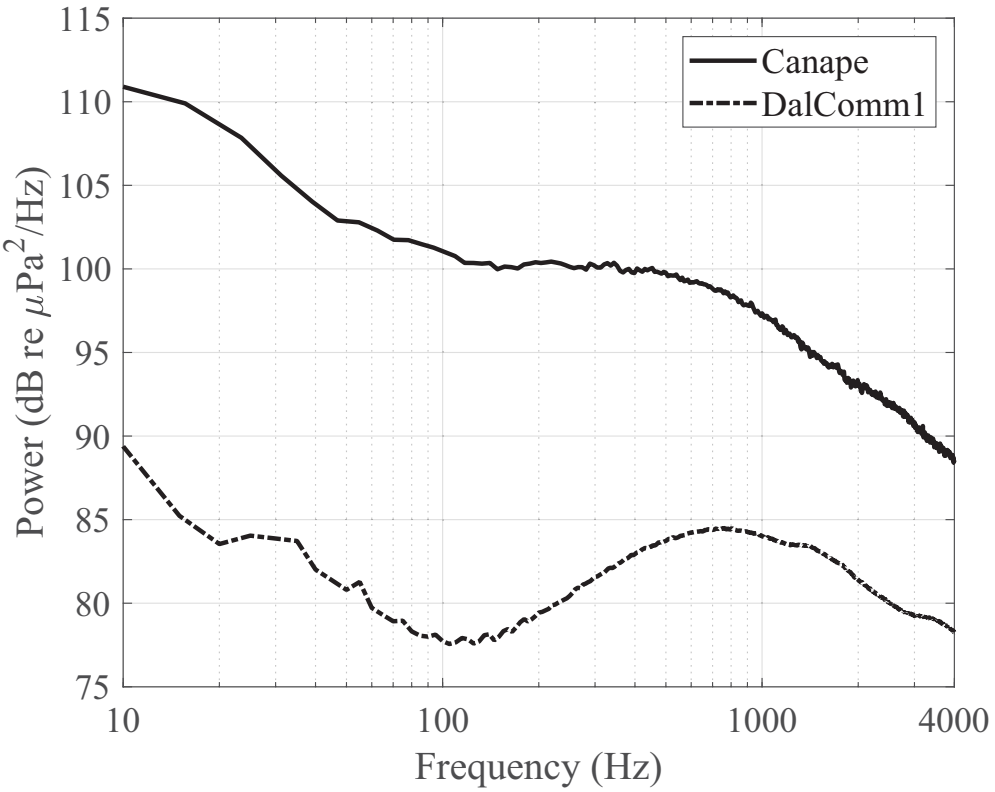

Figure 4.3: PSD of the ambient noise conditions during the DalComm1 and Canape experiments. Both noise processes were re-sampled at 10240 Hz and an FFT window of size 2048.

The empirical histogram was computed for the measured noise pressure time series and fit with the Normal distribution function whose probability density function (PDF) is defined as

$$f(x) = \frac{1}{\sigma\sqrt{2\pi}} e^{-\frac{1}{2}(\frac{x-\mu}{\sigma})^2}, \tag{4.7}$$

where the parameters μ and σ are the mean and standard deviation of the measured noise process, respectively, and $f(x)$ is calculated directly from the measured noise processes at both experiments.

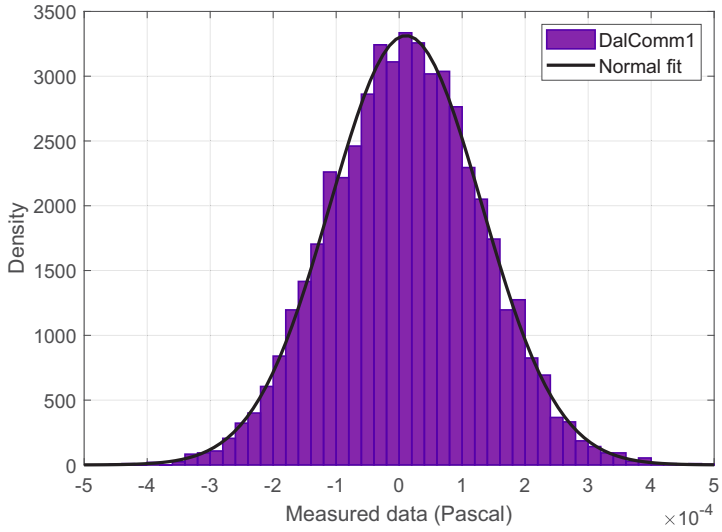

Figure 4.4: DalComm1 noise PDF using one-second duration

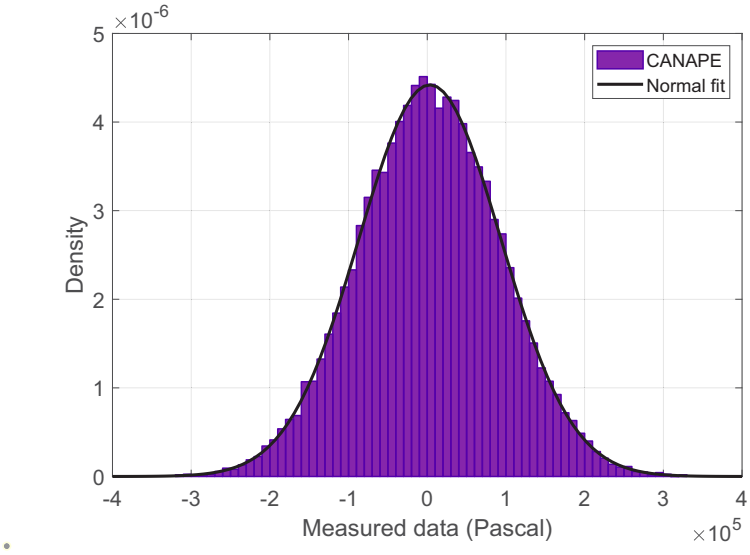

Figure 4.5: Canape noise PDF using one-second duration

From Fig. 4.4 and Fig. 4.5, it is observed that for a one-second duration, the normal distribution closely fits the data from both DalComm1 and CANAPE respectively. Since the normal distribution fits the empirical histograms with the least deviation over the short duration of a few seconds, for consistency and simplicity, the normal distribution was fit with the measured data for both measurements.

Note that the noise processes from both experiments were re-sampled throughout the rest of this work at 10240 Hz, which is the sampling frequency of the communication system which is discussed in Chapter 5. It should be noted that the signal at the output of DalComm1 recorder has a DC offset, which was cancelled prior to the analysis by calculating the long term average amplitude on each sensor output.

It is noteworthy that since the early days of underwater acoustic research, it has been shown that the distribution of OAN is not always consistent with the classical normal distribution [**?**, **?**]. For instance, in [**?**], it was shown that vessel and biological noise sources have kurtoses [2] that are markedly different from the Gaussian distribution, thus exhibiting non-Gaussianity. Similarly in [11], it was demonstrated that shipping noise sources exhibit non-Gaussianity when compared with background ocean noise which is predominantly Gaussian.

It has also been demonstrated that the performance of statistical signal detection algorithms depend on the distribution of the background noise [**?**]. In fact, in [**?**], it was shown through simulations that for signals transmitted in OAN, the BER is worse even at higher input SNR compared to signals in AWGN. Overall, the noise distribution can significantly impact the BER, and must be considered in the design of UWAC receivers. However, to limit the scope of the BER analysis developed in chapter 5, the OAN is assumed to be predominantly surface generated (also shown empirically in this Section), such that the normal distribution is a good fit for the data set.

Finally, on the pre-processing analysis of the noise measurements, the coherogram that represents the spatial coherence of the noise over windows spanning about 1-second each is presented. Fig. 4.6 and Fig. 4.7 represent the coherogram of DalComm1 and CANAPE noise measurements, respectively.

From Fig. 4.6, it is observed that the dominant coherent energies in DalComm1 time-series are in the lower bandwidths up to about 800Hz. The imaginary component also shows a minimum in these lower bandwidths. Also, from Fig. 4.7, the dominant coherent energies in the noise are in the lower bandwiths up to about 800Hz. It is evident that the variations in the coherence levels span throughout the measurement bandwidth. When compared to the well-known results in Fig. 2.4, the

[2] Kurtosis is a measure of the tailedness of the distribution from which a dataset is generated.

dominant bandwidths in the measured noise suggest that the dominant noise sources are primarily surface generated.

Although sonar transmissions are observed in the measured CANAPE noise, the sonar interference is avoided by selecting segments of the data set where there were no sonar transmissions. However, Fig. 4.7 shows the presence of the sonars since the full bandwidth of the noise is processed to show the dominant bandwidths. Therefore, the rest of the analysis in this chapter focuses on ambient noise sources that do not contain impulsive sources.

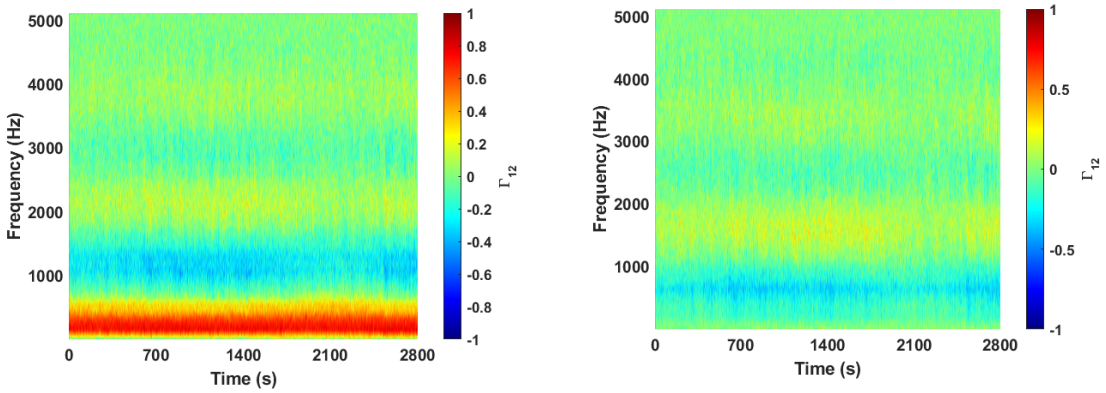

(a) Real coherogram

(b) Imaginary coherogram

Figure 4.6: Coherogram of DalComm1 noise computed over about 21 minute durations. $F_s = 10240$ Hz, $B_D \in \{0, Fs/2\}$.

4.3 Spatial Characteristics

The spatial characteristics of synthetic OAN is described in this section. Two distinct methodologies that model the spatial attribute of OAN over a wide bandwidth are described next.

4.3.1 Directionality Based Model (DBM)

A first method that relies on the knowledge of the directionality function of the noise field to generate the synthetic ambient noise process representing a measurement environment is presented in this section. In this method, the model presented by [4]

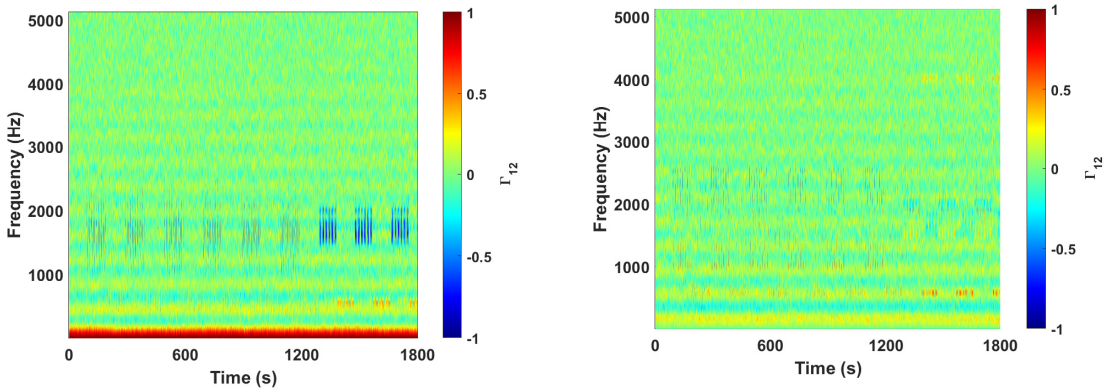

(a) Real coherogram

(b) Imaginary coherogram

Figure 4.7: Coherogram of CANAPE noise over a 20-minute duration. The data is resampled at $F_s = 10240$ Hz and $B_C \in \{0, Fs/2\}$.

for isotropic and surface noise over vertically spaced pairs of sensors, is enhanced to generate the noise time series at a five-element VLA using a three-step process. The procedure is described as follows:

Step 1. Computation of the directionality function.

The polar angle θ for random incident plane waves is taken with reference to the zenith and the directionality function for the noise field is computed. For example, for isotropic noise, the directionality function $\mathrm{F}(\theta)$ is

$$\mathrm{F}(\theta) = 1; \tag{4.8}$$

while for a surface noise field, the directionality function $\mathrm{F}(\theta)$ is

$$\mathrm{F}(\theta) = \cos^m \theta, \quad \text{for } 0 \leq \theta \leq \pi/2; \quad . \tag{4.9}$$

The noise directionality from (4.8) and (4.9) are shown in Fig. 4.8 in which the isotropic noise has a unit power with respect to all azimuthal angles while the surface noise has peak power in the upper hemisphere. From (4.9), $\mathrm{F}(\theta) = \cos^m \theta$, where $m = 1/30$ is obtained from [5]. Note that $\mathrm{F}(\theta)$ is a vector which could be of an arbitrary length. This model is representative of any desired noise field with a defined directional density function.

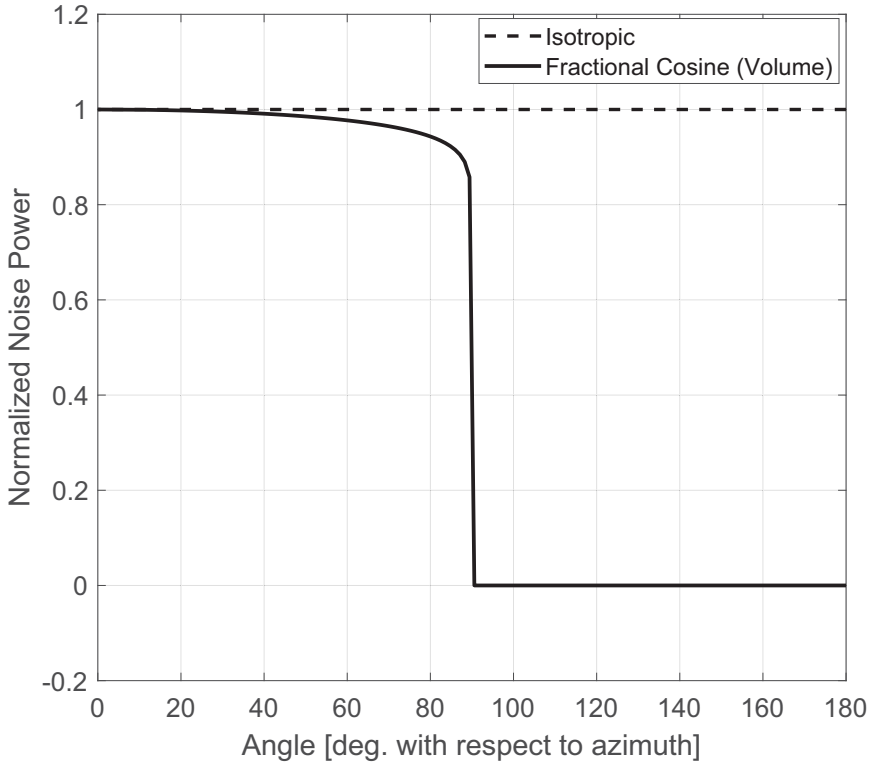

Figure 4.8: Directionality function for isotropic and volume noise fields.

Step 2. Computation of the noise process

In this step, first a random white Gaussian noise process $\mathbf{x}_m$ is generated with dimension $1 \times l$ at sensor m. Initially, when $\theta = 0$, the noise samples $X_m(\omega)$ with dimension $1 \times l$ are initialized with zeros, where $m = 1, 2 \ldots, M$; and M is the last element of the array, while l is the length of the discrete Fourier transform (DFT) window. The noise at each element of the array is computed from the expression

$$\mathbf{X}_m(\omega) = \int_{\theta=0}^{\pi} \left\{ \mathrm{F}(\theta) \mathbf{x}_m e^{-jd\frac{\omega}{c}\cos\theta} \right\} d\theta \tag{4.10}$$

where d is the distance between adjacent sensors, $\omega = 2\pi\ f$, and c is the local sound speed. Eq.(4.10) shows that at discrete directional angle θ, the random sources (or plane waves) are superimposed, such that these sources are integrated to yield the overall volume noise.

Step 3. Representation as a function of time

Signal $\mathbf{X}(\omega)$ across the array is transformed to the time domain by $\mathbf{X}[n] = \mathscr{F}^{-1}(\mathbf{X}(\omega))$

to represent the noise process over the array at discrete time n, such that $\mathbf{X}[n] = [\mathbf{X}_1[n], \ldots, \mathbf{X}_M[n]]^T$.

The normalized cross spectral density for pairs of sensors on the array are calculated from (3.35). For the isotropic noise field in (4.8), the coherence between adjacent pairs of sensors closely matches the analytical result given by (4.1) as shown in Fig. 4.9a. Similarly, from Fig. 4.9b, for the surface noise with a fractional cosine directional function in (4.9), the coherence of the noise process matches the analytical result given by Cron and Sherman in (4.2).

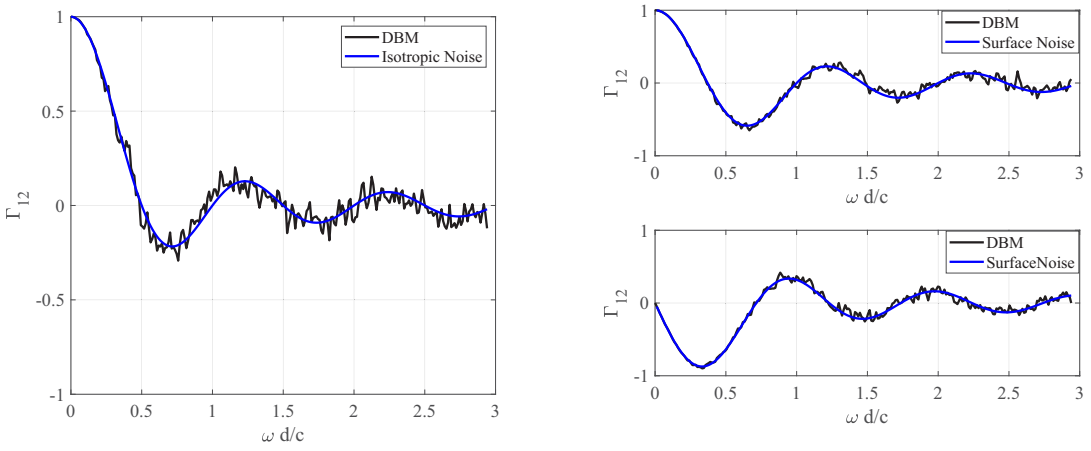

(a) Isotropic noise field

(b) Surface noise field

Figure 4.9: Coherence function from; (a) an isotropic noise field, and (b) surface noise field, validated against the coherence of synthetic noise from DBM.

Finally, to validate the noise model further, the directionality functions that generate noise processes that match the two measurement scenarios (DalComm1 and CANAPE) are computed. Although there are methods in literature that can be developed to compute the directionality function for the two sites computationally, for simplicity sake, a brute force approach was applied by guessing the value of m in (4.9) to generate a noise process whose coherence function estimates match DalComm1 and CANAPE's coherence.

From Fig. 4.10, it is observed that the coherence function of the synthetic noise reasonably matches the coherence from measured DalComm1 noise. The same is observed in CANAPE's coherence.

The model described thus far is applicable for any defined directional density

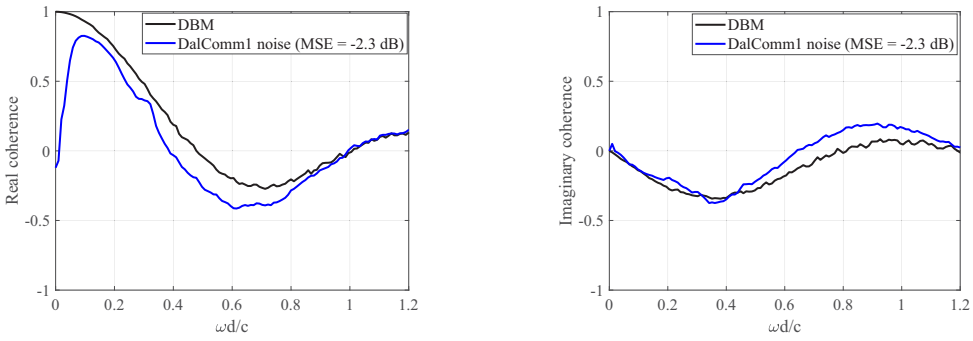

(a) Real vertical coherence (b) Imaginary vertical coherence

Figure 4.10: Real and imaginary vertical coherence using the the DBM model and validated against DalComm1 noise for sensors separated by 0.36m, sampled at $F_s = 10240$ Hz

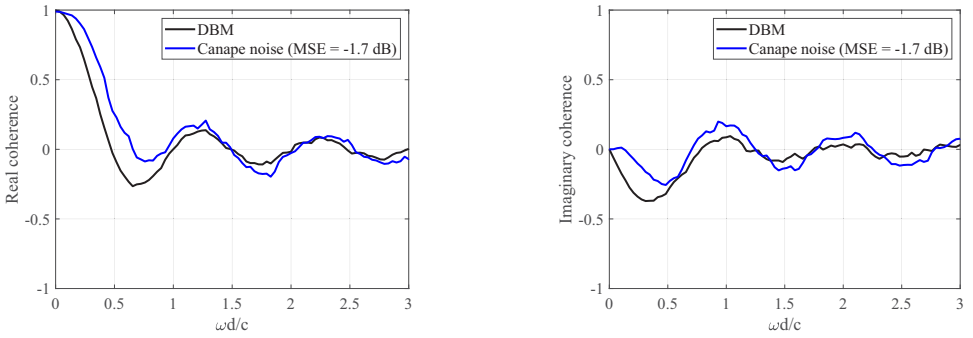

(a) Real vertical coherence (b) Imaginary vertical coherence

Figure 4.11: Real and imaginary vertical coherence using the DBM model and validated against CANAPE noise for sensors separated by 2.5m, sampled at $F_s = 10240$ Hz

function and would accurately generate the synthetic noise processes in the time or frequency domain that could be applied in characterizing the spatial performance of an underwater acoustic communication receiver.

4.3.2 Coherence Based Model (CBM)

A second model that generates the noise process from known spatial coherence function is described in this section. Cox's expression relates the vertical coherence for arrays in planar noise fields with the directionality function [4]. Although it is desirable to invert the integral expression to develop unique noise directionality functions from the spatial coherence, this approach could yield expressions that may not have unique numerical solutions. Instead, a method developed in [**?**], hereafter referred to as CBM, generates a noise process from a predetermined spatial coherence.

A five-step procedure is described to generate the noise process as follows.

1. A matrix $\mathbf{\Gamma}(\omega_n)$ that contains all the coherence functions and PSDs across the array, is computed for all discrete points of the angular frequency (ω_n), so that

$$\mathbf{\Gamma}(\omega_n) = \begin{bmatrix} \Gamma_{11}(\omega_n) & \Gamma_{12}(\omega_n) & \dots & \Gamma_{1M}(\omega_n) \\ \Gamma_{21}(\omega_n) & \Gamma_{22}(\omega_n) & \dots & \Gamma_{2M}(\omega_n) \\ \vdots & \vdots & \ddots & \vdots \\ \Gamma_{M1}(\omega_n) & \Gamma_{M2}(\omega_n) & \dots & \Gamma_{MM}(\omega_n) \end{bmatrix}. \tag{4.11}$$

   The elements of $\mathbf{\Gamma}(\omega_n)$ are the modeled spatial coherence, which may be obtained from (4.3). For the shallow water Pekeris waveguide case, the Green's function at each hydrophone is derived from (4.4) using the geoacoustic parameters in Table 4.1.

2. The eigenvalue decomposition of the coherence matrix is computed from $\mathbf{\Gamma}(\omega_n) = \mathbf{V}(\omega_n)\mathbf{\Lambda}(\omega_n)\mathbf{V}(\omega_n)$ and the mixing matrix $\mathbf{C}(\omega_n) = \sqrt{\mathbf{\Lambda}(\omega_n)}\mathbf{V}^H(\omega_n)$, where $\mathbf{\Lambda}(\omega_n)$ is the diagonal matrix that contains the eigenvalues, and $\mathbf{V}(\omega_n)$ is the matrix of the eigenvectors.

3. Random white Gaussian noise vector $\mathbf{N}(l, \omega_n)$ is generated, where l is the frame index at each element of the array of length M.

4. For all l and ω_n,
   compute $\mathbf{X}(l, \omega_n) = \mathbf{C}(\omega_n)\mathbf{N}(l, \omega_n)$, where $\mathbf{X}(l, \omega_n) = [X_1(l, \omega_n), \dots, X_M(l, \omega_n)]$ and $\mathbf{N}(l, \omega_n) = [N_1(l, \omega_n), \dots, N_M(l, \omega_n)]$.

5. Compute, the time-domain signal at each sensor m from the inverse short-time Fourier transform of $X_m(l, \omega_n)$ for $m = 1, \ldots, M$; i.e $\mathbf{X}[n] = \mathscr{F}^{-1}\{\mathbf{X}(l, \omega_n)\}$.

To compare the measured noise and the modeled noise, the error between the spatial coherence of the generated noise process from the CBM and the analytical model is computed from the normalized mean square error (MSE) and can be obtained from

$$\text{MSE} = \frac{\sum_{n=0}^{N/2} \left(\hat{\Gamma}_{yz}(\omega_n) - \Gamma_{yz}(\omega_n) \right)^2}{\sum_{n=0}^{N/2} (\Gamma_{yz}(\omega_n))^2}, \tag{4.12}$$

where N is the size of the fast Fourier transform (FFT) window, $\hat{\Gamma}_{yz}$ and Γ_{yz} are the estimated spatial coherence from the CBM, and the analytical spatial coherence from (4.3), respectively. The geoacoustic values are obtained from the geoacoustic parameters of the bottom summarized in Table 4.1. The MSE is presented in decibels (dB) by computing $10 \log_{10}(\text{MSE})$. This procedure generates the noise process from the coherence function that is computed from known geoacoustic parameters, but in fact, could be used for any coherence function.

To validate the noise model, three scenarios of the coherence are compared: 1) from the analytical model in (4.3); 2) from the noise process generated from the CBM; and 3) from the noise measured from DalComm1 and the CANAPE experiments. In both measurement scenarios, the coherence is compared for adjacent pairs of sensors.

From Fig. 4.12, there is a reasonable match between the analytical coherence obtained using (4.3), the synthetic noise generated using the CBM model, and the measured coherence from DalComm1. The roll-off at low frequency is due to the uncorrelated flow noise on the vertical line array [22], which was observed by inspecting the noise PSD. These lower bandwidths were excluded to avoid bias in the computation of the MSE.

Fig. 4.13 shows the comparison between the coherence obtained using (4.3), the coherence obtained using the CBM model, and the measured coherence from CANAPE. The observed deviation in the real (Fig. 4.13a) and imaginary (Fig. 4.13b) coherence may be attributed to the presence of horizontally propagating sounds during the measurement. This may be attributed to the sonar transmissions (discussed in Section

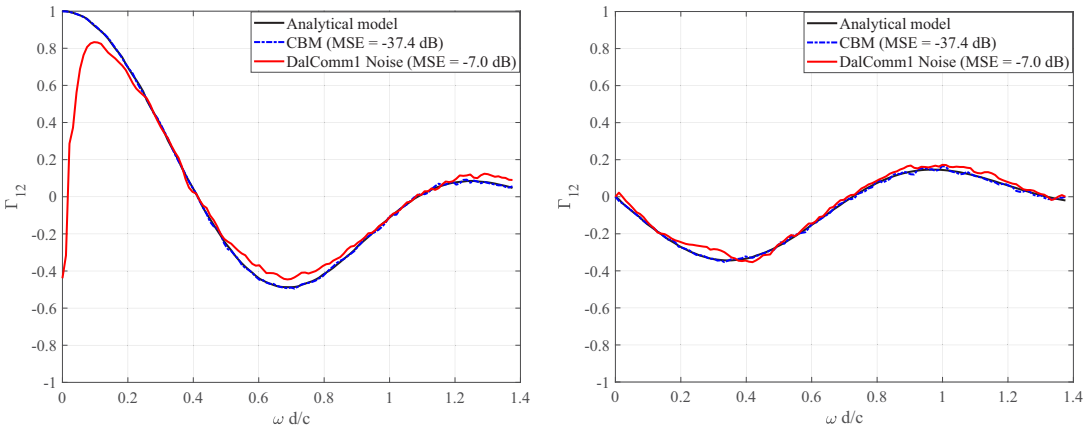

(a) Real vertical coherence (b) Imaginary vertical coherence

Figure 4.12: Real and imaginary vertical coherence computed using the analytical surface noise model (black), the CBM (blue dashed), and the DalComm1 data (red) against dimensionless frequency, for sensors separated by 0.38m, sampled at $F_s = 10240$ Hz

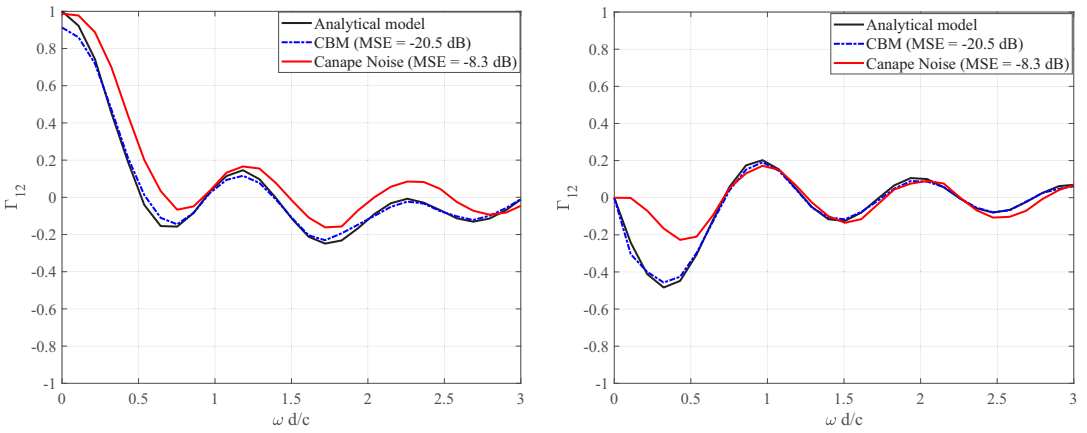

(a) Real vertical coherence (b) Imaginary vertical coherence

Figure 4.13: Real and imaginary vertical coherence using the analytical surface noise model, the CBM model, and validated against the empirical coherence from CANAPE noise for sensors separated by 0.38m, sampled at $F_s = 10240$ Hz

3.3) which may have partially overlapped on the noise measurement. The difference in the imaginary coherence at low frequency indicates that the models are not returning enough energy from the seabed, either due to incorrectly estimated geoacoustic parameters, or due to a layered, inhomogeneous basement [**?**]. It is noteworthy that the model in (4.3) requires a long computational time since the coherence is computed

over discrete frequency points. Very short DFT windows are used in this computation, which smooths the coherence curves.

In this section, two distinct methods – the DBM and the CBM have been presented to simulate the spatial property of an ambient noise process.

The slight differences in the coherence plots from DBM are primarily due to the method applied for computing the directionality functions. Hence, in practical applications, it is suggested that a computationally efficient method be applied to compute the directionality function of the noise fields. However, the method applied [**?**] for computing the theoretical coherence in the CBM is shown to be efficient. Consequently, the choice of the model used for generating the ambient noise time series would depend on the ease of obtaining or computing either a directionality function or a coherence function representing the noise fields.

4.4 Spectral Characteristics

The spectral signature of the synthetic space-time ambient noise can be described using an AR model. The AR parameters are extracted from the measured OAN from both experiments. The minimum order that minimizes the error output of the AR process was found to be 6. The AR coefficients define the all-pole filter whose magnitude response when applied to white noise as a low-pass filter, produces a coloured noise spectrum representative of ocean noise.

A procedure that characterizes the AR parameters from the PSD is described in [23]. The empirical expression [1] that characterizes the frequency dependent PSD of ambient noise due to breaking surface waves in units of dB re 1μPa is

$$10\log S_{yy} = 50 + 7.5w^{1/2} + 20\log(f) - 40\log(f + 0.4) \tag{4.13}$$

where w is the wind speed in m/s. The autocorrelation function may be obtained as the inverse Fourier transform (IFFT) of the PSD on a linear scale. Finally, the AR parameters may be obtained by solving the Yule-Walker equation. The AR parameters are computed by using the Levinson-Durbin recursion on the input estimate of the autocorrelation, via the built-in Matlab function *aryule* [**?**]. Each signal at the elements of the array may be filtered by the same all-pole filter, since the noise is

homogeneous across the array.

The synthetic noise processes generated from both the DBM and the CBM, together with the enforced spectral characteristics are compared with the measured noise process in Chapter 5. Next, the narrowband spectrum of OAN is discussed.

4.5 Ambient Noise in Narrowband Conditions

In this section, the PSD of ambient noise is verified over a narrowband spectrum. To this end, the measured ambient noise is downsampled at a center frequency $f_c = 2048$ Hz while the transmitted signal is band-limited using a raised-cosine filter to 240 Hz, matching the baseband receiver specifications[3] described in greater details in Section 5.

From Fig. 4.14, it is observed that the spectral power for the noise scenarios do not compare with that in Fig. 4.3 because Fig. 4.3 and Fig. 4.14 are evaluated in passband and baseband, respectively. Also, it can be noted that the measured noise PSD from both experiments are frequency dependent (with a defined trend) over a 240 Hz bandwidth. This observation is contrary to the spectrum of uncorrelated white noise samples which is known to be frequency flat and without a defined trend.

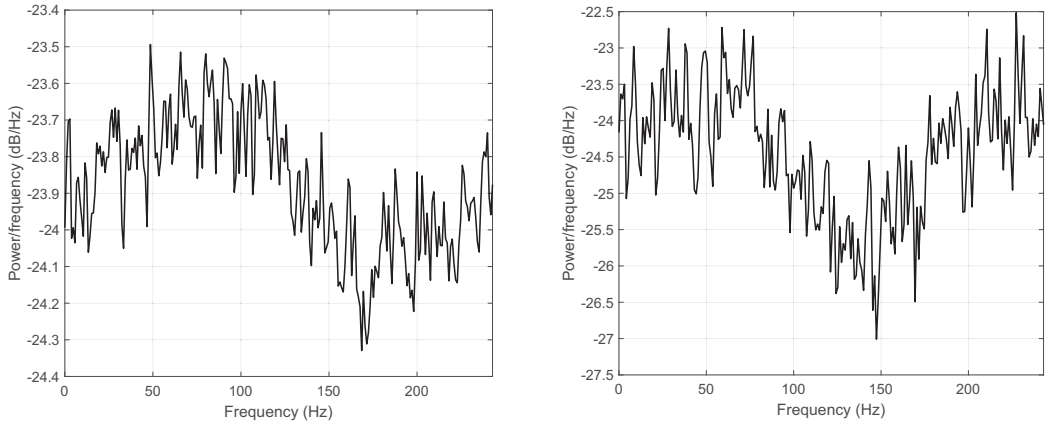

(a) DalComm1 (b) Canape

Figure 4.14: Baseband representation of PSD for measured noise centered at 2048 Hz with a bandwidth of 240 Hz for (a) DalComm1 and (b) Canape noise.

To confirm the spectral variability of the synthetic noise processes generated from

[3]The specification for the communication link is provided in response to the project sponsored by Ultra Electronics, Nova Scotia, under the The Atlantic Innovation Fund (AIF).

both CBM and DBM, representing DalComm1 and CANAPE's measurement locations, the PSDs were computed over a 240Hz bandwidth. The spatial characteristic of the synthetic noise process was generated as described in Section 4.3, while the spectral characteristics were obtained from Section 4.4.

From Fig. 4.15, it is observed that the spectrum in the synthetic noise computed from the CBM, representing both DalComm1 and CANAPE reasonably compare with the measured noise.

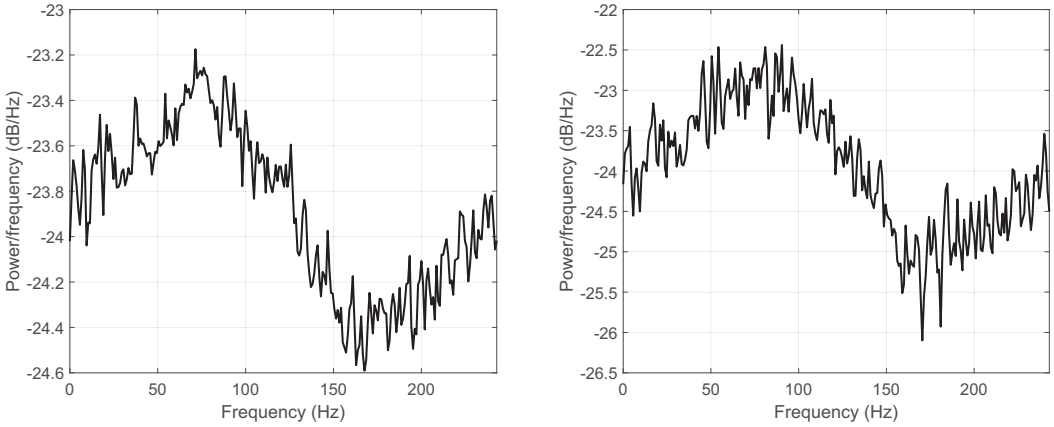

(a) DalComm1 (b) Canape

Figure 4.15: Baseband representation of PSD for synthetic noise (computed from the CBM) centered at 2048 Hz with a bandwidth of 240 Hz for (a) DalComm1 and (b) Canape noise.

Further, the PSD of the synthetic noise process generated from the DBM in Section 4.3.1 was computed over a 240Hz bandwidth. It is observed that by enforcing the spectral characteristic described in Section 4.4 on either synthetic isotropic or surface noise process, the spectrum over a 240Hz bandwidth are exactly the same. The spectrum of the space-time surface noise – with spatial attributes computed from the DBM and an enforced spectral attribute – over 240Hz bandwidth is showed in Fig 4.16. It is observed that the narrowband spectrum from DBM and CBM are similar. Thus, it can be concluded that the spatial and spectral content of OAN can be perceived as independent of each other.

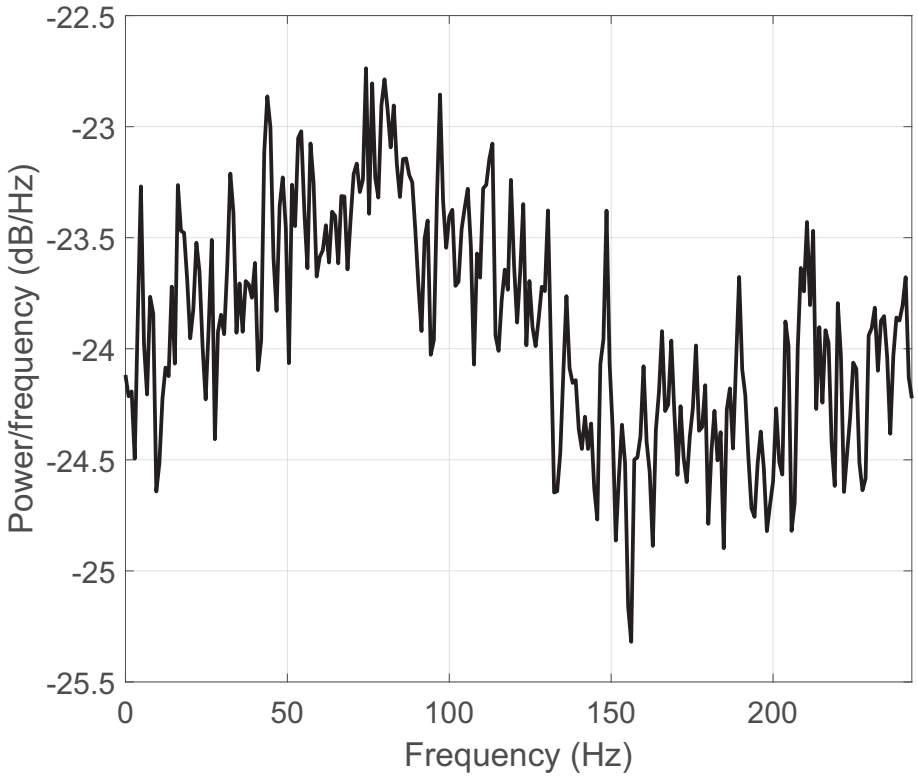

Figure 4.16: PSD of baseband surface noise (computed from the DBM) centered at 2048 Hz with a bandwidth of 240 Hz.

4.6 Temporal characteristics of Ocean Ambient Noise

In Chapter 3, the time varying characteristics of directional noise emanating from a vessel's propeller was demonstrated. This was achieved by implementing a ML-BF that estimated the TDOA of the acoustic noise pressure at a compact array of hydrophones. In this chapter, the temporal variability of naturally occurring OAN is demonstrated using the beamformer developed in Section 3.5 with the same system parameters. Thus, this section only focuses on the results obtained by applying the beamformer to the measured noise from DalComm1 and the VLA elements from the CANAPE experiment.

The measured broadband noise in both DalComm1 and CANAPE are sampled at $10,240$ Hz. The zero degree elevation represents broadside, while 90° and -90° represent the surface and the ocean bottom, respectively. The directionality results are computed from the kernel density estimates [4] of the elevation angles. The kernel

[4]Kernel density estimation is a method applied to estimate the unknown probability density

density estimates are computed at each point of the elevation angle and summed to produce the mean density of the directionality of the noise sources. Each point of the kernel density is depicted by a scatter plot so that the instantaneous change in the directionality of the noise can be observed. The intricate details about kernel density estimation goes beyond the scope of this dissertation, but there is an abundance of resources in literature on this topic [**?**].

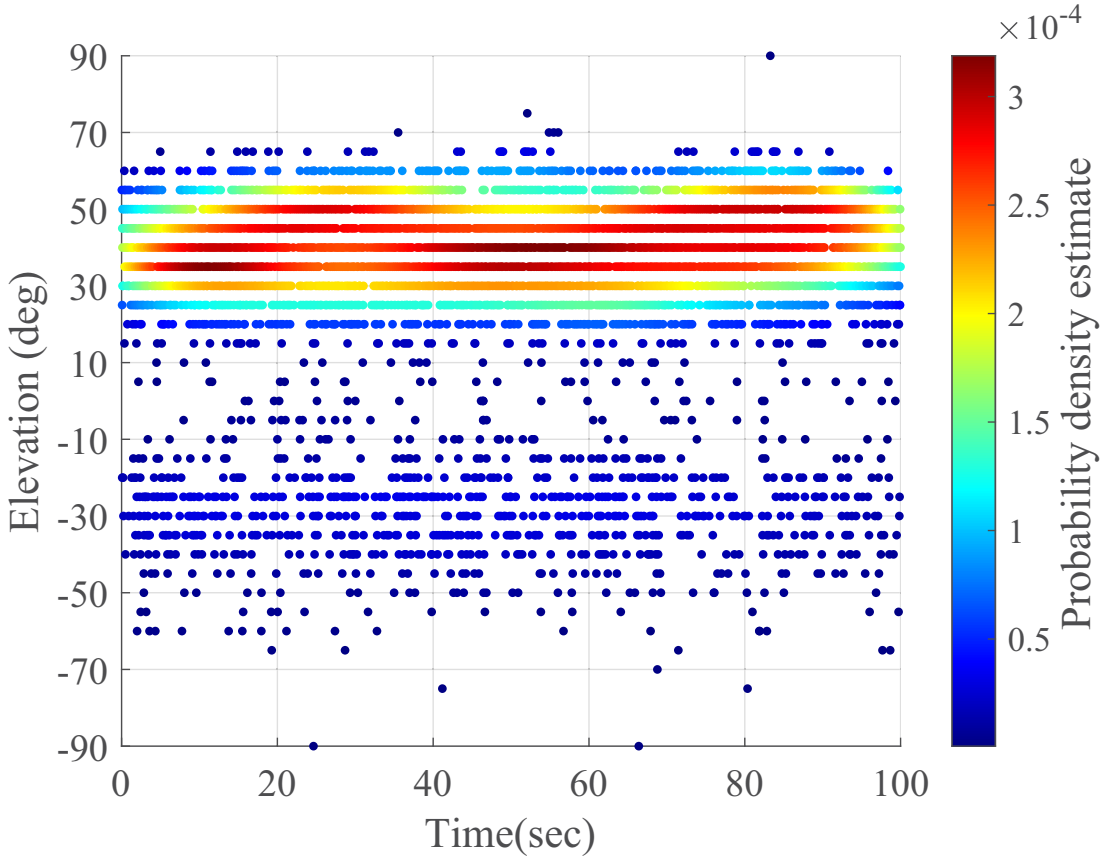

Figure 4.17: Beamformer directionality computed for windows spanning 0.01 second for measured DalComm1. The time axis represents the measurement duration.

From Fig 4.17, it is observed that the energy of DalComm1 noise propagates over elevation angles between 25° and 55°. It is found that the mean energy arrives from an elevation angle of 40° with a secondary peak at −30° relative the plane of the VLA. This suggests that DalComm1 noise peak energy arrives from a cone above the

function of some data. It defines a kernel function centered on each data point and summed together to generate the density function of the data.

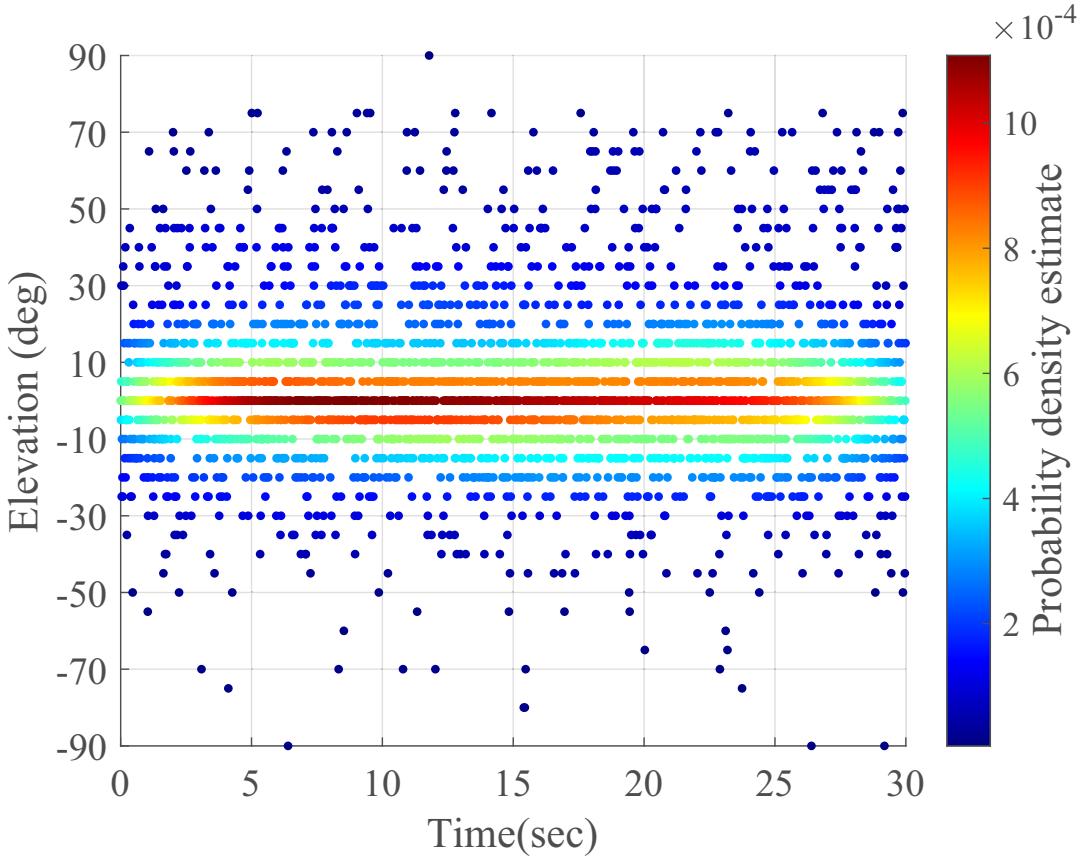

Figure 4.18: Beamformer directionality computed for windows spanning 0.01 second for CANAPE. The time axis represents the measurement duration.

array, while some reflected energy is observed from the seabed. This accords with the directionality expectation for an array deployed in relatively shallow water at mid-column. It is also observed that the directionality of OAN varies spatially and as a function of time. This property is expected to impact the array gain measured at the output of a spatial filter as will be demonstrated in Section 5.1.3.

The directionality of CANAPE's noise power in Fig 4.18 shows that most of the noise power arrives over elevation angles that span $-10°$ to $+10°$. The mean directionality also has a peak at $0°$ i.e. broadside. Although this observation is surprising, knowing fully that the spectrogram of CANAPE noise shows that the noise is predominantly surface generated, the directionality can be attributed to the reflected noise from the basement of the ocean considering that the array was deployed at a 1.5 meter offset from the bottom of the ocean.

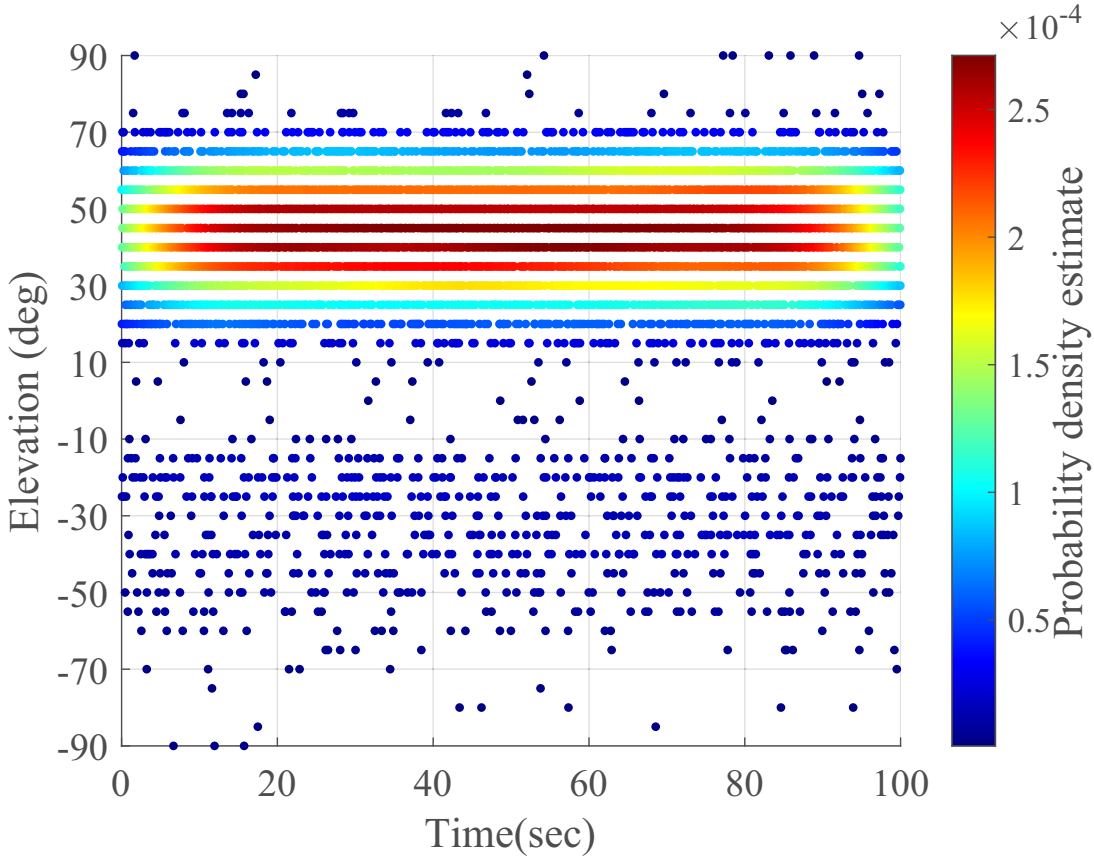

Figure 4.19: Beamformer directionality computed for windows spanning 0.01 second for the synthetic noise process representing DalComm1 measurement environment. The time axis represents the simulation duration.

To confirm the measured noise directionality, the mean noise directionality was computed from the synthetically generated ambient noise from the CBM, for both the DalComm1 and CANAPE cases. From Fig. 4.19, there is a good match in the beamformer directionality obtained from the synthetic DalComm1 noise and that of the actual measurements. However, the instantaneous variations in the directionality observed in the actual measurements are not present in the synthetic noise. Note that the low energies in the instantaneous directionality at the start and end of the duration are attributed to the averaging of the kernel density estimates. Furthermore, the directionality observed in the synthetic noise representing the CANAPE environment reasonably matches the actual measurement. Also, the instantaneous variations in the noise directionality is not as pronounced in CANAPE noise as in the DalComm1

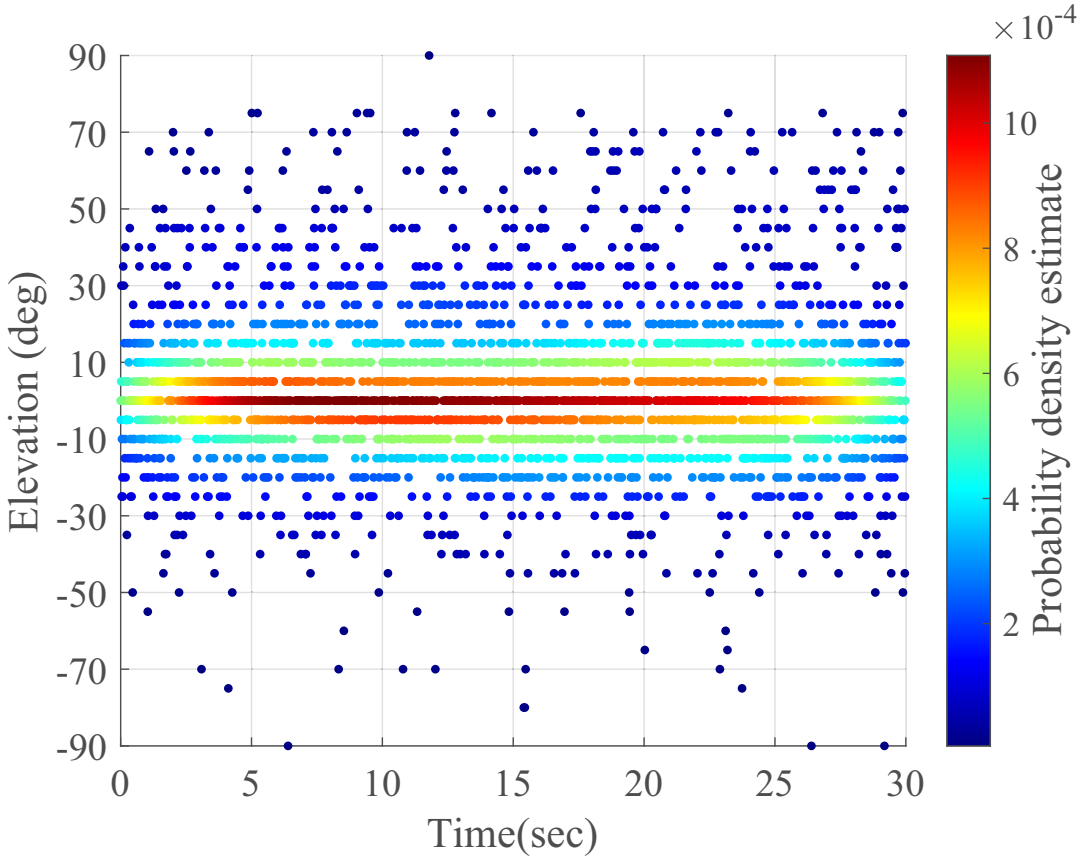

Figure 4.20: Beamformer directionality computed for windows spanning 0.01 second for the synthetic noise process representing CANAPE measurement environment. The time axis represents the simulation duration.

noise. This suggests that the sea state may be relatively stable in CANAPE more than in DalComm1 noise measurement. These instantaneous variations in directionality are expected to change the statistics of the noise process and in turn impact the frame structure of an underwater acoustic receiver. This phenomenon is investigated in Chapter 5, where the impact of the directional properties of ambient noise on the communication system is described.

Thus far in this chapter, the spatial and spectral characteristics of synthetic OAN have been described. The temporal characteristics of OAN have also been demonstrated from the measured ambient noise process. It can be concluded that OAN has three dimensions that characterize its properties – spatial, spectral and temporal. Finally, to be able to estimate the impact of OAN on the design of acoustic receivers,

it is desirable to estimate the coherence-time of the noise channel.

To summarize, in this chapter, two methods have been presented to generate an ambient noise process with unique spatial properties over a compact array. The first approach, the DBM, relies on the knowledge of the directionality of the noise field, while the CBM relies on knowledge of the coherence function between pairs of sensors on a compact array. The DBM generates non-stationary noise process whose spatial characteristic is defined from the coherence function [**?**]. The DBM also compares to the measured noise scenarios (DalComm1 and CANAPE), since the coherence functions can be easily computed numerically from the geoacoustic profile of the environments. Further, by enforcing the spectral characteristic from DalComm1 noise on the synthetic noise process from the DBM, the narrowband spectrum becomes frequency-dependent. Thus, the spectral content of OAN is not only important over broad bandwidths, but even over a narrow bandwidth, the spectrum is still frequency dependent. It is also noteworthy that the spectral shape of the noise does not depend on the spatial coherence of the noise process i.e. the spatial and spectral domain of OAN may be perceived as independent of each other.

The integral inversion that relates the directionality of noise fields and spatial coherence of two vertically aligned sensors was derived in [4]. Thus, under the assumption of a plane wave noise field, there is a relationship between the DBM and the CBM, or between the noise directionality function and the vertical noise coherence. Although it is desirable to invert the integral expression to develop unique noise directionality functions from the spatial coherence, the methods applied by the author showed that the inversion approach could yield expressions that may not have unique numerical solutions.

Finally, an AR model was used to superimpose the time-varying spectral signature on the spatially correlated synthetic noise. The spatial and spectral characteristics of measured ocean noise have been validated against the synthetically generated noise processes. The results indicate both long-term and short-term variations in directionality are expected to change the statistics of the noise process and in turn impact the frame structure of an underwater acoustic receiver. Next, in Section 5, the impact of the directional properties of ambient noise on the communication system is described.

Chapter 5

Impact of Ambient Noise on Space-time Equalizers

In this chapter, space-time equalizers are presented to optimize the communication performance in the presence of ambient noise and in a multipath propagation channel. In Section 5.1 the impact of ambient noise on an UWAC link is evaluated assuming linear equalizers in a controlled environment. Then, in Section 5.2, a space-time decision feedback equalizer is utilized to mitigate multipath distortion for a shallow water long range communication link subject to real ambient noise. Finally, in Section 5.4, a beamforming technique is described for mitigating vessel noise in an UWAC link.

5.1 The Impact of Ocean Ambient Noise in UWAC

In this section, to demonstrate the impact of ambient noise on an UWAC link, a linear space-time filter (STF) structure is used to optimize the communication reliability. This objective is approached by isolating the impact of OAN (i.e. a frequency-flat channel) on the acoustic link.

The rest of this section is organized as follows: in Section 5.1.1, the parameters of communication link are described; in Section 5.1.2, a linear space-time filter is analyzed and the recursive least square (RLS) is presented to obtain the space-time weights using adaptive algorithms; in Section 5.1.3, the impact of ambient noise on the array gain is analyzed analytically; in Section 5.1.4, the impact of ambient noise on the gain is computed through simulations; in Section 5.1.5, the BER is analyzed; in Section 5.1.6, the optimal training duration and payload duration of signals processed in OAN are analyzed. Note that the information symbols are processed in OAN in this section and the impacts of multipath reflections are excluded.

5.1.1 Model of the Communication Link

In this work, the UWAC link is modelled at baseband to characterize the impact of ambient noise. The binary information is modulated using phase shift-keying (PSK).

PSK is chosen because of its simplicity and its recognized reliability, even at relatively high data rates for PSK modulated signals [**?**] and in frequency shift-keying signals [24, 25].

The effect of ambient noise on a long-range communication system is evaluated, and to be able to achieve a long-range communication (up to several tens of kilometers), the acoustic receiver is centered at 2048 Hz while the transmitted signal is band-limited using a raised-cosine filter to 240 Hz. The measured ambient noise is down converted to baseband and bandlimited to the channel bandwidth (240 Hz). The VLA structure from DalComm1 is utilized to evaluate the BER in the presence of ambient noise and compared when AWGN is added so that the impact of OAN on the UWAC link can be evaluated. To further justify the importance of an accurate model of the ambient noise process, the BER is also evaluated when the signal is processed in synthetic ambient noise described in Section 4.3.

5.1.2 The Linear Space-time Filter

Similar to the model of the space-time linear system described in Section 2.4, the $M \times 1$ vector of the received signal $\mathbf{x}[n]$ at time n spatially sampled at the M elements of the array is

$$\mathbf{x}[n] = s[n] * \mathbf{h}[n] + \mathbf{n}[n], \tag{5.1}$$

where $s[n]$ is the information symbols, $\mathbf{h}[n]$ is a matrix of $M \times p$ CIRs between the transmitter and the M receive elements, where p is the length of the multipath taps, and $\mathbf{n}[n]$ is an $M \times 1$ vector of ambient noise at the array. Note that in free-space, $\mathbf{h}[n]$ is of unity gain and of $M \times 1$ dimension. Also, note that the operator $*$ is a convolution.

At the output of each sensor m, the signal is sampled at the symbol rate T_s as shown in Fig. 5.1, and a time-domain equalizer that consists of K weighted multiple tap delays is applied to the window of received samples $\mathbf{x}_m[n] = [x_{m,0}\ x_{m,1}\ \ldots\ x_{m,(K-1)}]^T$ to mitigate the impact of the channel distortion on the signal. Then, the weighting vector $\mathbf{a}_m = [a_{m,0}\ a_{m,1}\ \ldots\ a_{m,(K-1)}]^T$ optimizes the MMSE between $s[n]$ and $\mathbf{x}_m[n]$. Also, the MMSE filter is augmented to process an array of M sensors, such that the filter output at time n is

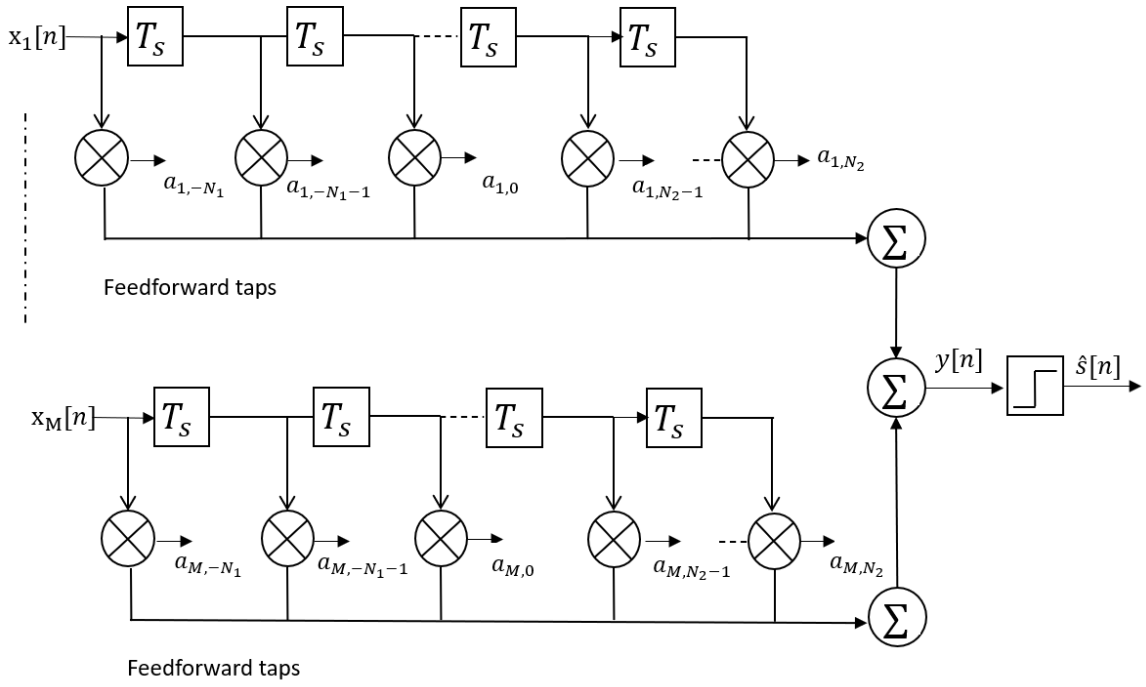

Figure 5.1: Tapped delay line filter structure with feedforward taps.

$$\mathrm{y}[n] = \sum_{m=0}^{M-1} \sum_{k=-N_1}^{N_2-1} \mathbf{x}_{m,k}[n]\mathbf{a}_{m,k}^{*} \tag{5.2}$$

where * denotes the complex conjugate, the feedforward taps has a total length $K = N_1 + N_2 + 1$, and the received signal is delayed by N_1 samples to maintain causality [9]. To obtain the weights for the STF, the weighting vectors at the elements of the array can be organized in a $MK \times 1$ vector such that $\mathbf{a}_{st} = [\mathbf{a}_0^T \ \mathbf{a}_1^T \ \ldots \ \mathbf{a}_{(M-1)}^T]^T$. Also, the $MK \times 1$ input vector to the filter is defined as $\mathbf{x}_{st} = [\mathbf{x}_0^T \ \mathbf{x}_1^T \ \ldots \ \mathbf{x}_{(M-1)}^T]^T$, such that

$$\mathrm{y}[n] = \mathbf{a}_{st}^H \mathbf{x}_{st}, \tag{5.3}$$

where the superscript ^{H} denotes the hermitian transpose.

Eq. 5.2 represents the output of a finite-impulse-response (FIR) space-time filter with a linear structure. The linear FIR filter (also referred to as the feedforward filter) is the simplest adaptive equalizer structure whose current and past values of the received signal are linearly weighted by the filter coefficient $\mathbf{a}_m$ and summed to

produce the output. The filter output (sometime referred to as the soft decision) can be demodulated (also referred to as the hard decision) so that the information bits can be recovered at the receiver.

The ability of this array of filters to reliably receive the transmit signal depends on the efficient computation of the space-time weights (or filter coefficients). Several algorithms have been developed to compute these weights and the choice of an appropriate algorithm depends on the application of the STF. Also, various space-time filters have been described to resolve signal directionality and to combat frequency selectivity in multipath channels [26, 27, 28], one of which is discussed in Section 5.2.

Two types of the algorithms that were applied to compute the feedforward weights $\mathbf{a}_{st}$ are succinctly described next.

The Matrix Inversion Solution

The optimum weights $\mathbf{a}_{st}$ can be obtained by using the matrix inversion solution otherwise known as the Wiener-Hopf's filter defined as

$$\mathbf{a}_{st} = \mathbf{R}_{st}^{-1}\mathbf{p}, \tag{5.4}$$

where the space-time covariance matrix $\mathbf{R}_{st}$ of the filter's tap input vector can be computed using

$$\mathbf{R}_{st} = \mathbb{E}[\mathbf{x}_{st}\mathbf{x}_{st}^{H}], \tag{5.5}$$

and the correlation vector $\mathbf{p}$ between the filter input and transmit symbol $s[n]$ at discrete time n is defined as $\mathbf{p} = \mathbb{E}[\mathbf{x}_{st}\mathbf{s}^{*}[n]]$. Eq. 5.4 is the optimum matrix solution for the linear filtering problem [2]. It should be noted that the matrix inversion in (5.4) is computationally expensive, hence not often a desirable solution for hardware implementation, it however remains a preferred solution to compute the optimal weights of an equalizer.

The RLS Filter

In a more realistic system design (with hardware implementation in mind), the optimum weights $\mathbf{a}_{st}$ are computed using stochastic gradient descent techniques. Using

these techniques, the filter is adapted based on the error between the transmitted and the received signal at the current time. There are several algorithms developed based on the gradient descent technique. However, the RLS algorithm is described in this work due to its fast convergence time [2]. The weights are updated at each snapshot of time to maximize the receive power for all the symbols measured at the array by

$$\mathbf{a}_{st}[n] = \mathbf{a}_{st}[n-1] + \mathbf{k}[n]\xi^*[n]. \tag{5.6}$$

The weighting vector computed at the previous iteration is denoted as $\mathbf{a}_{st}[n-1]$ and the predicted error at time n is

$$\xi^*[n] = \mathbf{s}^*[n] - \mathbf{a}_{st}[n-1]\mathbf{x}_{st}[n], \tag{5.7}$$

which is the difference between the desired response $\mathbf{s}^*[n]$ and weighted tap input vector $\mathbf{x}_{st}[n]$. From (5.6), the gain vector $\mathbf{k}[n]$ penalizes the predicted error by using the expression

$$\mathbf{k}[n] = \mathbf{P}[n-1]\mathbf{x}_{st}[n]\{\lambda + \mathbf{x}_{st}^H[n]\mathbf{P}[n-1]\mathbf{x}_{st}[n]\}^{-1}, \tag{5.8}$$

where λ is the forgetting factor and the inverse correlation matrix $\mathbf{P}[n]$ is updated recursively from

$$\mathbf{P}[n] = \lambda^{-1}\mathbf{P}[n-1] - \lambda^{-1}\mathbf{k}[n]\mathbf{x}_{st}^H[n]\mathbf{P}[n-1]. \tag{5.9}$$

Both algorithms – the matrix inversion and RLS, although introduced for computing the space-time weights, can be reduced to either the spatial or temporal dimensions to compute $\mathbf{a}_s$ or $\mathbf{a}_t$ respectively. There are other algorithms that are well known in literature to compute the weighting vectors. A classical solution for spatial filtering is the MVDR filter which was briefly introduced in Chapter 3 and will be further discussed in Section 5.4.

Overall, the goal of a filter – spatial or temporal, is to mitigate the impact of the impairments due to multipath bounces, interference, noise and/or synchronization errors on the transmit signal. The array gain (AG), which represents the SNR at the ouput of the filter divided by the SNR at the filter inputs, is a figure of merit often

used to quantify the signal power relative the noise power, while the BER is used to determine the number of information bits that have been altered by the sources of distortion in the communication link. Both AG and BER are used as the figures of merit to evaluate the impact of OAN on an UAWC link in this work. Therefore, in Section 5.1.3 an analytical approach is taken to examine the impact of ambient noise on the AG.

5.1.3 Impact of Noise Spatial Correlation on the Array Gain – An Analytical Approach

In this section, the impact of the spatial correlation property of OAN on the AG measured at a spatial array is demonstrated analytically. The analysis developed in this section relies on (5.1), and assumes that the signal of interest is subject to a single path arrival. Based on this assumption, the impact of ambient noise on the communication signal at the receiver can be analyzed in a controlled setting.

At the receiver, a spatial filter with a single memory element is used to reliably detect the information symbols. An array of sensors at the receiver is typically used to provide SNR gain in the received signal. The exact value of gain depends on the desired signal correlation $\mathbf{R}_s$ as well as the noise correlation $\mathbf{R}_n$ between the elements [1].

From (5.1), having assumed that $\mathbf{h}[n] = 1$, the filter output spatial correlation across the elements of the array can be expressed as

$$\mathbf{R}_{xx} = \mathbf{R}_s + \mathbf{R}_n. \tag{5.10}$$

Recall that from (3.23), the output of a spatial beamformer was defined. Similar to the frequency domain expressions in (3.23), but this time at discrete snapshots of time, by substituting (5.1) into (5.10), the spatial correlation can be expanded into

$$\mathbf{R}_{xx} = \mathbb{E}\{\mathbf{x}\mathbf{x}^H\} = \mathbb{E}\Big\{ \big(\mathbf{v}(\theta)s[n] + \mathbf{n}[n]\big)\ \big(\mathbf{s}^H[n]\mathbf{v}^H(\theta) + \mathbf{n}[n]\big) \Big\}, \tag{5.11}$$

where $\mathbf{v}(\theta)$, $s[n]$, $\mathbf{n}$, $\mathbb{E}$, H are the steering vector, the signal of interest, the additive noise, the expectation operator and hermitian operator respectively. Without losing generality, let $\mathbf{a}$ represent the spatial weights at the array elements which can be

computed using any spatial filtering technique. Hence, the array gain at the output of the beamformer, which is ratio of the weighted signal correlation to the weighted noise correlation can be expressed in terms of the correlation matrices as

$$\mathrm{AG} = 10\log\frac{\mathbf{a}^H\mathbf{R}_s\mathbf{a}}{\mathbf{a}^H\mathbf{R}_n\mathbf{a}}. \tag{5.12}$$

From (5.12), it is evident that an accurate assessment for the AG depends on the estimates of $\mathbf{R}_s$ and $\mathbf{R}_n$. For signals in uncorrelated noise with variance σ_n^2, the noise covariance matrix $\mathbf{R}_n^u = \sigma_n^2\mathrm{I}$, and (5.11) resolves to

$$\mathbf{R}_{xx}^u = \mathbf{v}(\theta)\mathbb{E}\big\{s[n]\mathbf{s}^H[n]\big\}\mathbf{v}^H(\theta) + \sigma^2\mathrm{I}, \tag{5.13}$$

where the superscript ^{u} denotes uncorrelated noise.

However in correlated ambient noise, the directionality of the noise cannot be ignored. Hence, the steering vector is applicable to the noise as well as the signal. Thus, similar to (5.1), the equation for the received signal can be expressed as

$$\mathbf{x}[n] = \mathbf{v}(\theta)s[n] + \mathbf{v}_n(\theta)\mathbf{n}[n], \tag{5.14}$$

where the subscript n differentiates the steering vector $\mathbf{v}_n(\theta)$ of the correlated noise from that of the desired signal. Thus, for correlated noise

$$\mathbf{R}_{xx}^c = \mathbb{E}\{\mathbf{x}\mathbf{x}^H\} = \mathbb{E}\Big\{\big(\mathbf{v}(\theta)s[n] + \mathbf{v}_n(\theta)\mathbf{n}[n]\big)\ \big(\mathbf{s}^H[n]\mathbf{v}^H(\theta) + \mathbf{v}_n^H(\theta)\mathbf{n}[n]\big)\Big\}. \tag{5.15}$$

where the subscript ^{c} denotes correlated noise. Following the same derivation in (5.13), Eq.(5.15) can be resolved into

$$\mathbf{R}_{xx}^c = \mathbf{v}(\theta)\mathbb{E}\big\{s[n]\mathbf{s}^H[n]\big\}\mathbf{v}^H(\theta) + \mathbf{v}_n(\theta)\mathbf{A}\mathbf{v}_n^H(\theta)\sigma^2, \tag{5.16}$$

where $\mathbf{A}$ is a square matrix of the spatial correlation values, such that $\mathbf{A} \to \mathrm{I}$ for uncorrelated noise. In (5.16), we can write $\mathbf{R}_n^c = \mathbf{v}_n(\theta)\mathbf{v}_n^H(\theta)\mathbf{A}\sigma^2$, while $\mathbf{R}_s = \mathbf{v}(\theta)\mathbb{E}\big\{s[n]\mathbf{s}^H[n]\big\}\mathbf{v}^H(\theta)$ in (5.13) and (5.16).

From (5.16), it can be implied that the received signal at an array depends on the steered response of the signal as well as the steered response of the correlated noise.

Note that it was established in Section 4.6, that the instantaneous directionality of the noise could vary as a function of time. This also suggests that the AG may vary temporally. Therefore, the instantaneous AG in (5.12) for signals in uncorrelated noise expands into

$$\mathrm{AG}^{u} = 10\log\frac{\mathbf{a}^{H}\mathbf{v}(\theta)\mathbb{E}\big\{s[n]\mathbf{s}^{H}[n]\big\}\mathbf{v}^{H}(\theta)\mathbf{a}}{\mathbf{a}^{H}\mathbf{a}\sigma^{2}\mathrm{I}}, \tag{5.17}$$

while for signals in correlated ambient noise,

$$\mathrm{AG}^{c} = 10\log\frac{\mathbf{a}^{H}\mathbf{v}(\theta)\mathbb{E}\big\{s[n]\mathbf{s}^{H}[n]\big\}\mathbf{v}^{H}(\theta)\mathbf{a}}{\mathbf{a}^{H}\mathbf{v}_{n}(\theta)\mathbf{A}\mathbf{v}_{n}^{H}(\theta)\sigma^{2}\mathbf{a}}. \tag{5.18}$$

Eq. (5.17) and (5.18) can be further resolved by computing the eigen-value decomposition (EVD) of $\mathbf{R}_{xx}^{u}$ in (5.13) and $\mathbf{R}_{xx}^{c}$ in (5.16), so that insights can be provided about the impact of the correlated matrix $\mathbf{A}$ on the AG.

From (5.13) and (5.16), the EVD of matrix $\mathbf{R}_{s}$ can be expressed as $\mathbf{R}_{s}\vec{\mathbf{v}}_{s} = \lambda_{m}\vec{\mathbf{v}}_{s}$, where $\vec{\mathbf{v}}_{s}$ and λ_{s} are the eigenvectors and the corresponding eigenvalues of $\mathbf{R}_{s}$ respectively. From the properties of EVD [**?**], the eigenvalues of $\mathbf{R}_{xx}^{u}$ in (5.13) are $\lambda_{n} + \sigma^{2}$ and the eigenvectors remain unchanged across the elements of the array. However, from (5.16), the EVD of $\mathbf{R}_{xx}^{c}$ depends largely on the EVD of matrix $\mathbf{A}$. The eigen-decomposition of $\mathbf{A}$ may be written as $\mathbf{A}\vec{\mathbf{v}}_{n} = \lambda_{n}\vec{\mathbf{v}}_{n}$. The eigenvalues λ_{n} of $\mathbf{A}$ are unique acrosss the array elements, and for an M-element array, there are M independent eigenvectors whose directions are unique. In fact, as indicated in [**?**], λ_{n} will take on large values at some noise observations, while the values will be smaller at other observations. The author also demonstrated that the SNR of correlated isotropic noise differs from that of uncorrelated noise and the signal processing requires a different approach.

The comparison between OAN and uncorrelated AWGN stems from the fact that noise in UWAC systems are often assumed to be AWGN. As discussed in chapter1 and 2, this assumption underestimates the impact of OAN on the UWAC system. Hence, the rest of the analysis developed in this chapter, compares OAN with uncorrelated AWGN samples.

In summary, since the directionality of OAN varies spatially and as a function of time, the AG will also varies as a function of time. This is primarily due to the spatial

correlation property of the noise, which is related to the change in the instantaneous directionality of the noise [4]. Also, the correlation property of OAN impacts the AG measured at spatial arrays. This observation contradicts the assumption that ambient noise impacts the performance of an UWAC link similarly to AWGN. To further strengthen this analysis, the AG of measured and synthetic ambient noise is evaluated computationally in Section 5.1.4.

5.1.4 Impact of Noise Spatial Correlation on the Array Gain – A Computational Approach

In the previous section, the impact of the spatial correlation on the AG was demonstrated analytically. Also, knowing fully that the correlation property of OAN is related to the directionality of the noise samples, it is important to closely examine the impact of noise directionality on the AG. Therefore, the impact of noise directionality on the AG is demonstrated computationally in this section. To this end, the communication link described in Section 5.1.1 is applied.

The binary information signal is modulated using the binary phase-shift keying (BPSK) and transmitted over a single tap channel. At the receiver, OAN is added. The impinging angle of the received signal is assumed to be known at the receiver, so that the array response is calculated from (3.17) where $0^\circ \leq \theta \leq 180^\circ$. The spatial weighting vector $\mathbf{a}_s$ that maximizes the AG in the direction of the impinging signal is computed from the RLS algorithm described in Section 5.1.2 using the linear FIR structure.

At the output of the spatial receiver, the symbols are demodulated. The error vector magnitude (EVM) between the soft decision and the demodulated signal is calculated and the output SNR is obtained from $\text{SNR}_{\text{out}} = -20\log(\text{EVM}/100)$. The AG is obtained by subtracting the input SNR (SNR_{in}) from th SNR_{out} i.e. $\text{AG} = \text{SNR}_{\text{in}} - \text{SNR}_{\text{out}}$. Through simulation, the input SNR is set to 3 dB to assess the effect of noise on the signal at a relatively low SNR.

The AG is computed when the signal of interest is processed in AWGN, in measured noise as well as using synthetically generated ambient noise from DBM and CBM. It is expected that in AWGN, the AG is approximately equal to $10\log n \approx 7$ dB $\forall\ \theta$ since the directionality of AWGN is the same in all look directions.

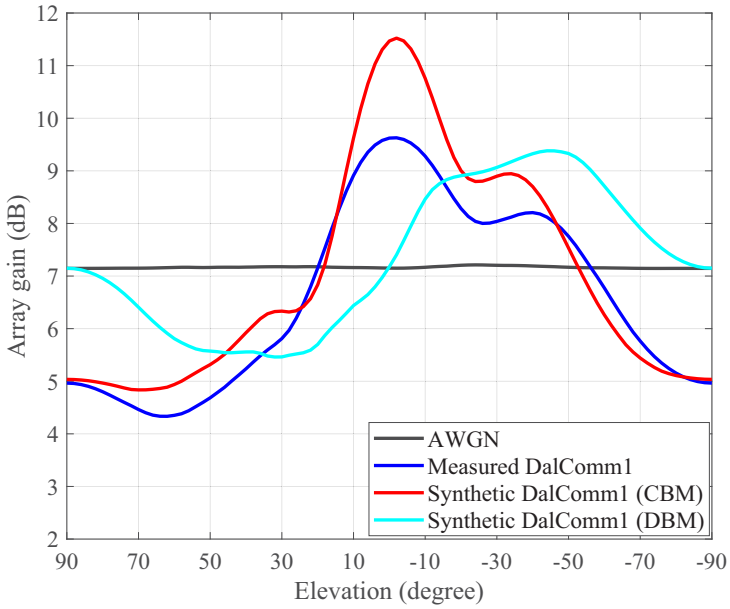

Figure 5.2: Array gain of signals processed in AWGN and DalComm1 noise. The bandwidth is 240 Hz and $f_c = 2048$ Hz.

The elevation angles are represented with respect to the center of the array, such that the negative angles are measured from the center of the array to the seabed, and the positive elevation angles are measured from the center of the array to the sea surface.

The following observations are made about the computed AG shown in Fig. 5.2:

- The AG ≈ 7.0 dB $\forall\ \theta$ when the information signal is processed in AWGN. Note that the smoothness in the flat spectrum of AWGN is related to the FFT averaging window. Similarly, the moderate variations in the value of the AG in AWGN are attributed to the frame duration used to in the simulation setup in Fig. 5.2. In comparison, in presence of measured DalComm1 noise, the AG of the STF varies over about 8 dB as a function of the elevation angles.

- The AG in DalComm1 noise is maximum at broadside (i.e 0°) and minimum between 30° and 70°. This observation is expected since the directionality of DalComm1 noise shows that the noise power is maximum between 30° and 70° and minimum at broadside, as in Fig. 4.17. It is also observed that the AG at broadside is about 2.7 dB greater than in AWGN.

- For synthetic DalComm1 noise computed from the CBM, the AG moderately deviates with about 2 dB gain at broadside.

- A more drastic deviation of the AG is observed from the synthetic DalComm1 noise computed from the DBM.

There are two different conclusions from this section. First, the AG computed for signals in CBM generated noise closely compare with the measured ambient noise from the DalComm1 experiment. The deviation observed in the AG of DBM generated ambient noise is associated with the brute force approach that was used to validate the directionality of the noise fields as discussed in Section 4.3.1. It is expected that the AG will closely compare with the empirical noise if a more refined methodology is used to match the directionality of the noise field in the DBM method. Second, the assumption that the spatial property of OAN compares with that of an AWGN has been further verified as inaccurate by evaluating the spatial AG at a VLA. It is established that the AG of OAN depends on the noise directionality which varies spatially and temporally. The impact of ambient noise on the BER is discussed in Section 5.1.5.

5.1.5 Impact of Ambient Noise on BER

Having established in Section 5.1.3 and Section 5.1.4 that the directionality of OAN has an impact on the spatial AG, in this section, first, the impact of the directionality of OAN on the BER is described, and second, a frame structure that optimizes the BER of an UWAC link is characterized through simulations.

The same model of the communication link described in Section 5.1.1 is applied in this section. The BER is computed in the different noise scenarios – AWGN, measured and empirical DalComm1. The optimum space-time weighting vector $\mathbf{a}_{st}$ is computed from the matrix inversion algorithm for the linear FIR STF structure. The matrix inversion algorithm is preferred in the simulations in this section, so that the optimum weights that mitigate the noise can be computed across the elements of the array.

The filter is trained for a sufficiently long period using a subset of the noise frame. Then the the rest of the frame is applied as payload symbols over which the BER

is computed. The BER is computed after the entire noise (measured or synthetic DalComm1) time-series is processed. The filter is re-trained at each repetition of the received frame so that an optimum weight is obtained for each transmitted frame. The filter performance is evaluated at quite low SNR values because of the gain provided by applying multiple sensors at the receiver.

BER in a Noise Corrupted Channel

First, to confirm the accuracy of the simulated STF, the BER is computed for signals processed in a free-space environment and in the presence of AWGN. The BER is compared with standard theoretical values for BER in AWGN for BPSK modulated signals obtained from the analytical expression $0.5\text{erfc}(\sqrt{M\ 10^{(\text{SNR}_{\text{in}}/10)}})$. To allow convergence, the training sequence is 1024 symbols, while the payload sequence is 1024 symbols. From Fig. 5.3 [15], it observed that the simulated BER values closely compare with the theoretical values.

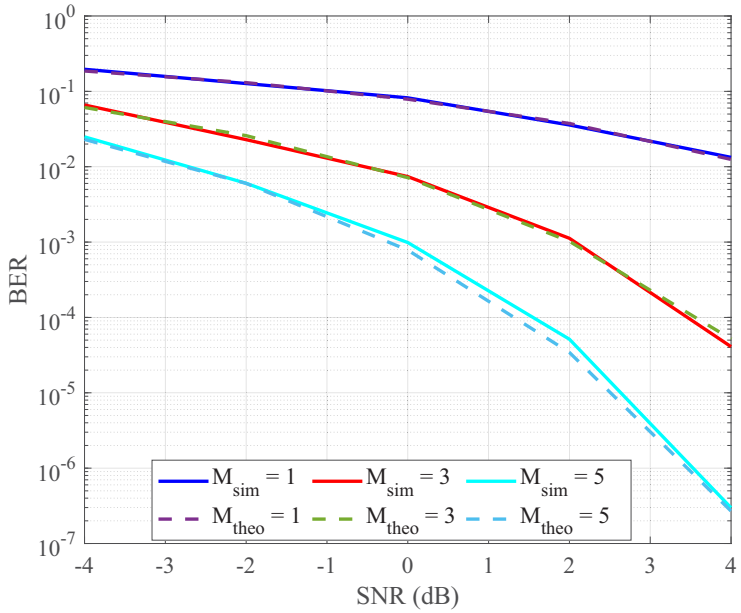

Figure 5.3: BER of signals processed in AWGN (i.e. sim) and compared with theoretical BER values for BPSK modulated signals in AWGN.

Further, the BER values were obtained for signals processed in measured DalComm1 noise as well as the synthetic noise processes computed from DBM and CBM. From Fig. 5.4, it is observed that the BER values for a single receiver element in measured DalComm1 compare closely with theoretical values in the low

SNR regime. However, when multiple elements are combined, a BER improvement is observed at low SNR: specifically for $M = 3$, the SNR is improved by 1.2 dB to obtain a BER of 10^{-3}, while for $M = 5$, the SNR is lower by about 2.0 dB to obtain a BER of 10^{-3}. The BER worsens significantly at higher SNR values (greater than 0 dB), albeit at a low BER of about 10^{-5}. The BER deterioration is attributed to the changes in the noise process, since the received frames are repeated multiple times so that a set error threshold is achieved before computing the BER. Frame repetition is a well-known method for evaluating the BER of a communication link [15]. Unlike the stationary noise process in AWGN, OAN process yields properties which are may only be stationary within certain durations [**?**].

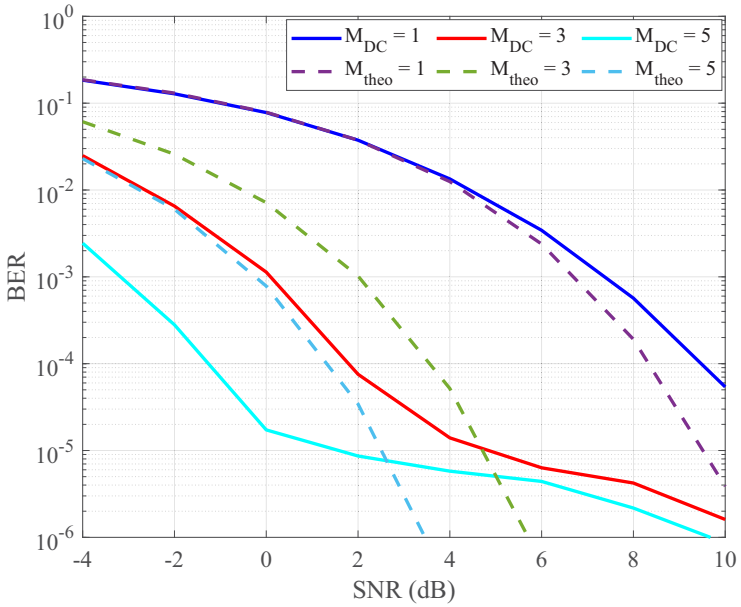

Figure 5.4: BER of signals processed in measured DalComm1 noise and compared with theoretical BER values for BPSK signals in AWGN. The bandwidth is 240 Hz and $f_c = 2048$Hz

From Fig. 5.5b, for signals processed in synthetic DalComm1, a close match is observed in the BER for the noise process obtained from the CBM in the low SNR regime. However, contrary to the BER deterioration observed in empirical DalComm1 noise, the BER in CBM-generated noise converges. This suggests that the noise statistics does not temporally vary as in the measured DalComm1 noise. Hence, the BER does not fully compare with the measured DalComm1 noise. It is also observed that the BER in DBM-generated noise does not compare with that of the empirical

noise.

Although different properties of the synthetically generated noise (from DBM and CBM) described in this work have been validated against measured noise, the deviation in the BER is attributed to the temporal variations in the measured OAN which is attributed to the variations produced by events at the sea surface due to wind.

These results demonstrate the limitations of the CBM to represent time-varying noise. Although the time-varying noise properties of OAN is not modeled in this work, the approach described in [**?**] for generating wind noise with defined temporal statistics in mobile communication devices is suggested to further improve the CBM for generating OAN.

Having established that the statistics of OAN varies temporally and has an impact on the BER, next, an optimum frame structure is defined for signals processed in measured DalComm1 noise. Also, note that the rest of the analysis in this chapter are based on the measured DalComm1 noise and compared with AWGN.

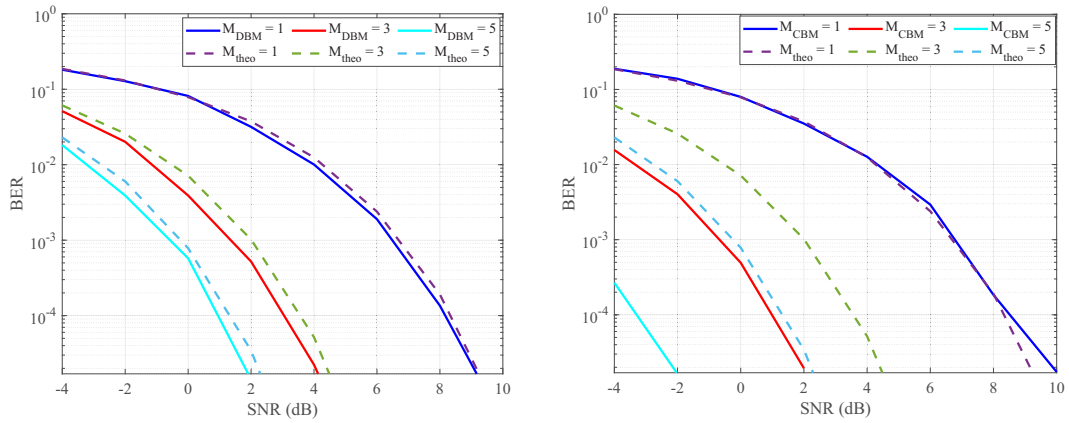

(a) DalComm1 from DBM (b) DalComm1 from CBM

Figure 5.5: BER simulation scenarios for signals processed in synthetic DalComm1 noise process using: (a) The DBM, and (b) The CBM. The bandwidth is 240 Hz and $f_c = 2048$Hz.

5.1.6 An Optimum Frame Structure in OAN

In this section, a frame structure that maximizes the BER in measured OAN is defined computationally.

Having shown that the BER in OAN diverges when multiple frames of the communication signal are averaged over time, it is desirable to establish a time constant over which the BER of the communication link can be optimized. To define a frame structure that optimizes the BER in an UWAC link, frames containing the information signals with varying training lengths, and varying payload lengths are transmitted in a simple free space channel. As will be demonstrated, both the training length and the payload length can be optimized when processed in OAN.

First, the input SNR is set at 2 dB to ensure the impact of ambient noise can be assessed by the STF. The filter is trained at different intervals equal to 2, 3, 4, and 5 seconds, and the minimum payload duration is one second which is equivalent to 240 symbols. Using the training sequence, at the receiver, the weights $\mathbf{a}_{st}$ are obtained by using the Wiener-Hopf's filter, as described in (5.4). Then, the payload is applied to the STF weights obtained during the training. To ensure consistency in the simulation scenarios, the BER is computed after the entire measured noise time-series is processed and a maximum number of errors equal to 1000 is achieved.

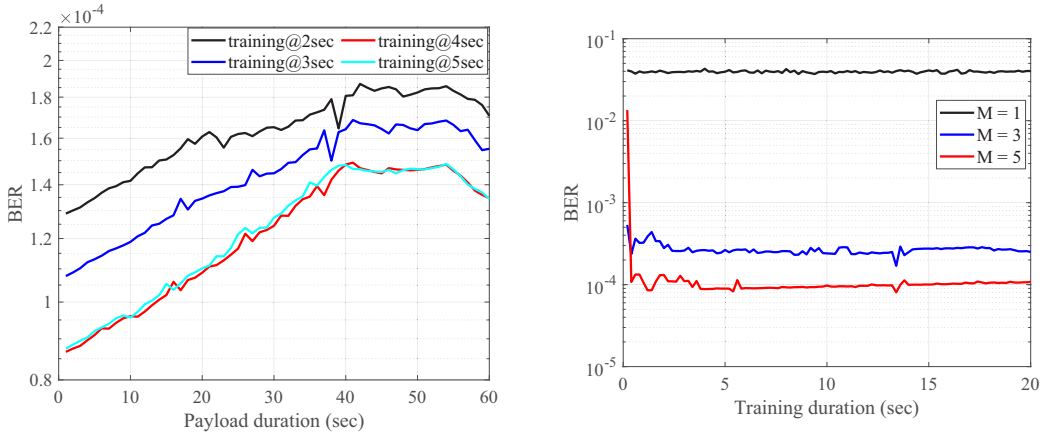

(a) (b)

Figure 5.6: (a) BER as a function of payload duration using the STF in measured DalComm1 noise. (b) BER as a function of training lengths for a fixed payload length at 3 seconds. The bandwidth is 240 Hz, $f_c = 2048$ and the input SNR is 2 dB.

Fig. 5.6a shows the BER as a function of payload duration for the different training lengths. It can also be observed that increasing the payload duration produces a small degradation in the BER. The degradation is attributed to the fact that the noise spatial statistics changes over this short time period. Also, from Fig. 5.6b, it

is observed that the filter must be trained for at least 4 seconds to converge to a reasonable BER. This is expected, since a longer training period will allow a better averaging, and it should be noted that 4 seconds corresponds to 960 training symbols (recall that the transmit signal is band-limited to 240 Hz). As the training length increases beyond 4 seconds, the BER stays relatively constant or even suffers a small degradation. Hence, it is suggested that the training length be set at 4 seconds and the filter should be retrained after about 4 seconds to optimize the BER.

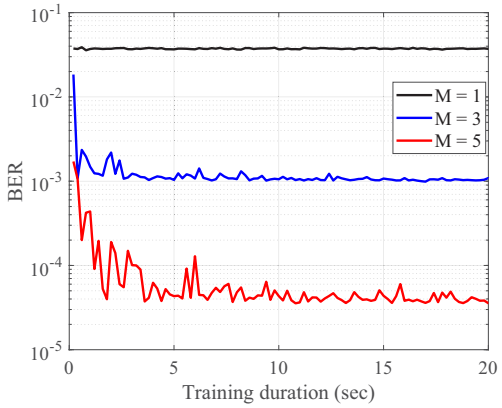

Figure 5.7: BER in AWGN using a Wiener-Hopf STF for different array size M. The bandwidth is 240 Hz and the SNR of 2 dB with five receivers.

To validate the impact of the ambient noise process, the BER is also evaluated in AWGN. From Fig. 5.7, it is observed that contrary to the observations in measured DalComm1 noise, the BER converges after about 7 seconds of training sequence and stays relatively constant at a mean value of 3.4303×10^{-5} at an input SNR of 2 dB. This is the expected value from the theoretical BER expression $0.5\text{erfc}(\sqrt{M10^{(\text{SNR}/10)}})$ in BPSK, where $M = 5$ and SNR $= 2$dB.

5.2 A Space-time Filter in Realistic Deployment Conditions

In the previous section, the impact of noise has been demonstrated assuming an ideal signal. The analyses that have been presented thus far also exclude the impact of the multipath reflections in the propagation channel. In this section, the impact of OAN as well as that of the multipath channel is analyzed by using a robust coherent

receiver. The STF structure is enhanced with a decision-feedback and a robust space-time filter with hypothesis testing is developed in this section.

5.2.1 The Decision Feedback Equalizer

Recall that the equations that characterize the STF with a linear structure have been discussed in Section 5.1.2 and the same have been used to evaluate the impact of noise in an UWAC link. The computational complexity of the linear SFT increases in severe multipath conditions, because the number of filter taps becomes excessively large. As such, in this section, alternative filter structures are applied for a reliable signal detection.

The decision feedback equalizer (DFE) is a well know filter structure. Using the DFE, once an information symbol has been detected and a hard decision has been made, the ISI that it induces on the future symbols can be estimated and subtracted out before the detection of future symbols. Thus, the DFE is a great solution for estimating the equivalent impulse response of a channel. The DFE can be realized either in the transversal form or as a lattice filter [9]. The direct form of filtering consists of a feedforward filter and a feedback filter, where the feedback filter is driven by the symbol decisions at the output of the feedforward filter. Thus, the feedback coefficients can be adjusted to cancel out the ISI in the current symbol at the DFE i.e. the past detected symbols from the feedforward filter.

Following the same derivation in Section 5.1.2, the DFE has K' feedback filter taps and the output of the combined filter structure can be expressed as

$$\mathrm{y}[n] = \sum_{m=0}^{M-1} \sum_{k=-N_1}^{N_2-1} \mathbf{x}_{m,k}[n-k]\mathbf{a}^*_{m,k} + \sum_{m=0}^{M-1} \sum_{k'=0}^{K'-1} \mathbf{b}^*_{m,k'}\mathrm{y}[n-k'], \tag{5.19}$$

where $\mathbf{b}^*_{m,k'}$ represents the feedback weights of length K' at sensor m. The filter structure depicted in Fig. 5.8 combines the feedforward taps with length $K = N_1 + N_2 + 1$ and feedback taps with length K' at the symbol rate, for a single receiver. Note that this filter structure is extended for an array of multiple elements yielding a space-time DFE.

Following a similar description as in the feedforward weights, the weighting vector of the feedback filter at sensor m is $\mathbf{b}_m = [b_{m,0}\ b_{m,1}\ \ldots\ b_{m,(K'-1)}]^T$ and the space-time

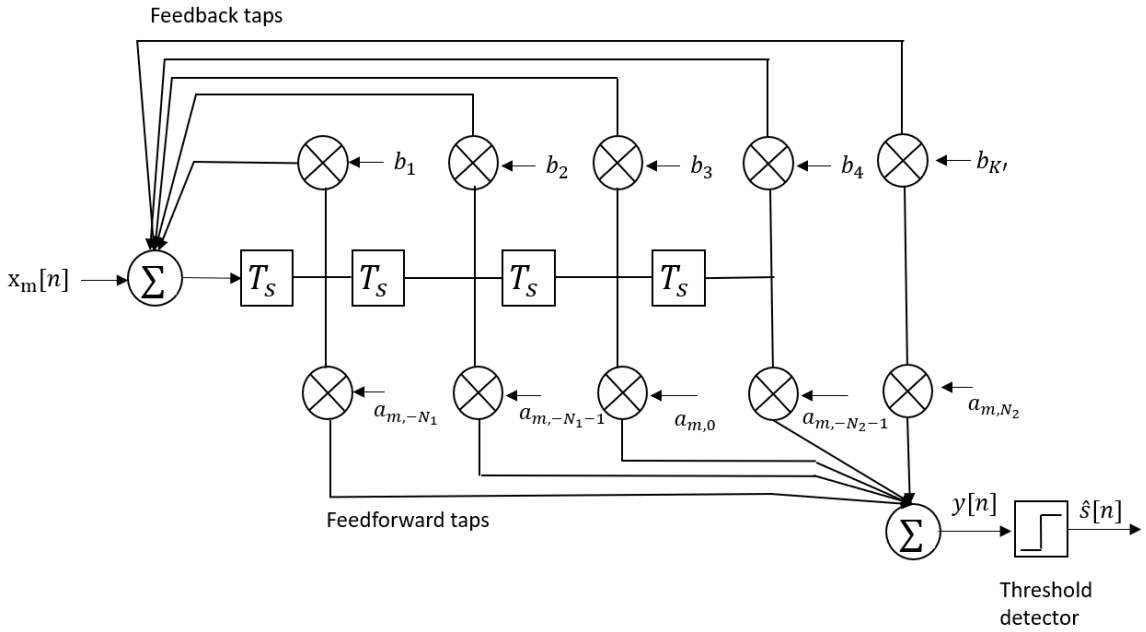

Figure 5.8: Tapped delay line filter structure with both feedforward and feedback taps.

weights across the elements of the array is $\mathbf{b}_{st} = [\mathbf{b}_0^T \ \mathbf{b}_1^T \ \ldots \ \mathbf{b}_{(M-1)}^T]^T$. The DFE is incorporated into a coded coherent filter which is described next.

5.2.2 Decision Feedback Equalizer with Hypothesis Feedback

A DFE for coherent UWAC was first described in [29] to implement coherent transmission. Direct-sequence spread spectrum was added to the communication link in [30], so that a similar code division multiple-access (CDMA) technique that has been used in RF communication is applicable for an UWAC link. The enhanced system with spread spectrum technology was later applied for low-SNR regimes in [31].

In a direct-sequence spread spectrum system, the signals from different spreading codes are considered to be transmitted from different users. Typically, a single-user scheme is used at the receiver due to its low complexity. A single-user receiver uses the knowledge of the spreading code at the transmitter to detect only the desired user's signal. It is typically comprised of a de-spreader that is matched to the spreading code, followed by a decision device. Adaptive single-user receivers have also been shown to be robust against multipath ISI. Therefore, the DFE receiver applied in this section is

robust in mitigating ISI, and because the equalizer weights are continuously adapted, it can track variations of the channel as well as the noise variations as a function of time. The spread spectrum added to the communication system also helps to improve the tracking ability in presence of multipath and noise [15].

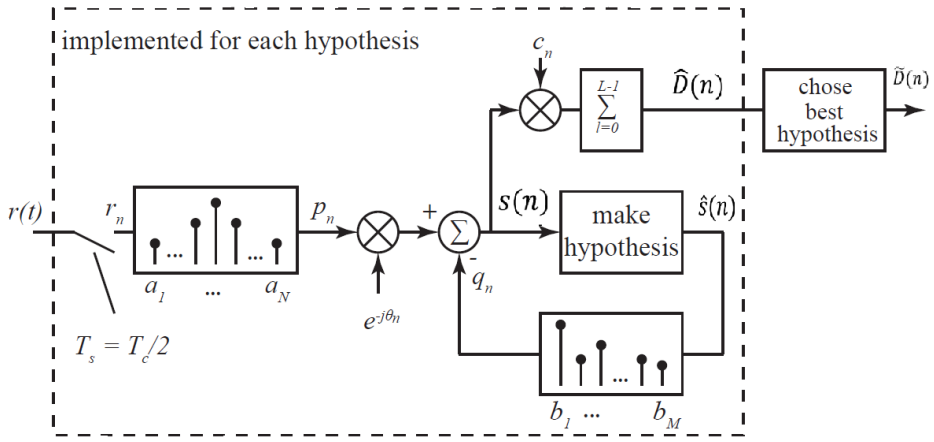

Figure 5.9: Fractionally spaced DFE enhanced with a spread spectrum code.

The same model of the communication link described in Section 5.1.1 is used in this section. The acoustic receiver is centered at 2048Hz, while the transmit signal is bandlimited to 240Hz.

5.2.3 The Single-element Hypothesis Feedback Equalizer

The equalizer structure that is applied for a single receiver element is shown in Fig. 5.9. A detailed development for the filter is described in [30], while a succinct description of the equations that characterize the filter is provided in this section.

At the transmitter, a baseband equivalent Quadrature Phase-Shift Keying (QPSK) modulated symbols is generated. There are four possible hypotheses: $1, +1j, -1, -1j$ for the QPSK modulation. At user $i = 1, \ldots, I$, the spread spectrum duration is $T = LT_c$, where L is the processing gain of the system, $R_c = 1/T_c$ is the chip rate and $R = 1/T$ is the symbol rate. The spread information sequence at the i-th user is $d_i(k)$ such that

$$u_i(t) = \sum_k d_i(k) g(t - kT_c). \tag{5.20}$$

where $g(t)$ is the transmitter pulse, $k = nL + l$ and $l = 0, \ldots, L-1$. Let the information symbol transmitted at time nT be denoted by $D_i(n)$ and the codeword at the i-th user be $p_i(l)$. Then, the spread sequence at the i-th user is

$$d_i(k) = D_i(n)p_i(l). \tag{5.21}$$

The signal $u_i(t)$ is passed through a multipath channel and the received signal from all the users combined with the the additive noise is

$$\mathbf{r}(t) = \sum_{i=1}^{I} h_i(t)u_i(t-\tau_i)e^{j\theta(t)} + \mathbf{n}(t), \tag{5.22}$$

where $h(t)$ is the CIR and $\mathbf{n}(t)$ is the additive noise, and the boldface n distinguishes the noise from the time index.

The DFE in Fig. 5.9 relies on a feedforward equalizer that cancels the post-cursor ISI and a feedback equalizer that cancels the pre-cursor ISI i.e. the ISI in the past detected symbol from the feedforward filter. The feedforward filter's sample rate T_s is twice the signature chip rate T_c, i.e. $T_s = T_c/2$. A phased correction can then be applied before the filtering operation at the receiver. In the application described in this work, a coherent detection is assumed such that the phase correction can be excluded. To maintain causality, the received signal is delayed by N_1 samples, such that at time index n, the feedforward filter input is

$$\mathbf{r}(n) = [r(nT_c + N_1T_s) \cdots r(nT_c - N_2T_s)]^T, \tag{5.23}$$

The feedforward weighting coefficients can be arranged in a vector $\mathbf{a} = [a_{-N2} \cdots a_{N1}]^T$, so that the output produced at each symbol interval excluding the carrier phase update is

$$p_n = \mathbf{a} \cdot \mathbf{r}^T. \tag{5.24}$$

Similarly, the feedback filter input consists of the K' previously detected symbol decisions, i.e. $\hat{\boldsymbol{s}} = [s_1 \cdots s_{n-K'}]$ and its weighting coefficients are $\mathbf{b} = [b_1 \cdots b_{K'}]$. The output of the feedback filter can therefore be expressed as

$$q_n = \mathbf{b} \cdot \hat{\boldsymbol{s}}^T, \tag{5.25}$$

and the combined filter coefficient $\mathbf{w} = [a^T b^T]^T$ is obtained jointly by using an RLS filter. The RLS algorithm that updates the filter coefficients was described in Section 5.1.2. The RLS forgetting factor that accommodates the time variations in the channel is set to $\lambda = 0.98$. Also, the equations that describe the phase detector and its update mechanism that tracks the channel phase fluctuations have been presented in [29].

A hypothesis is made on the transmitted information symbols. For QPSK demodulation, four tracking hypotheses are implemented – one for each possible symbol. The reference for each spreading code is the spread spectrum signature at the transmitter, weighed by the symbol hypothesis. For each hypothesis value of $D_i(n)$, the corresponding chips are fed back into the filter, and an estimate of the current chip is made. The chip estimates are used for de-spreading and a symbol decision is made after integration over all the signature chips. A minimum Euclidean distance detector is used to make the best decision. The filter coefficients that lead to the symbol decision are retained to initiate the detection of the next symbol.

5.2.4 An Enhanced Multi-element Receiver Structure

In this Section, the DFE is enhanced to account for multiple elements at the receiver to improve the reliability of the UWAC link. The advantage of using multiple elements at the receiver is two-fold – power gain and diversity gain.

The architecture of the space-time receiver is shown in Fig 5.10. The multi-element DFE is an enhanced structure of Fig. 5.9 which includes a feedforward equalizer, a decision feedback filter (described in Fig. 5.8) as well as a phase-locked loop (which is excluded in this work). Thus, the output of the filter are regulated by the same equations as described in Section 5.2.3. However, the feedforward filter inputs are organized to include the input window from multiple hydrophones. The output from each of the four hypotheses is integrated at all the elements of the receiver before the chip decision is made. As indicated in Section 5.2.1, the DFE is useful for time-varying environments. For, this purpose, the DFE updates the weights at the convergence rate of the RLS filter, while a phase-locked loop can be used to maintain carrier and

clock recovery.

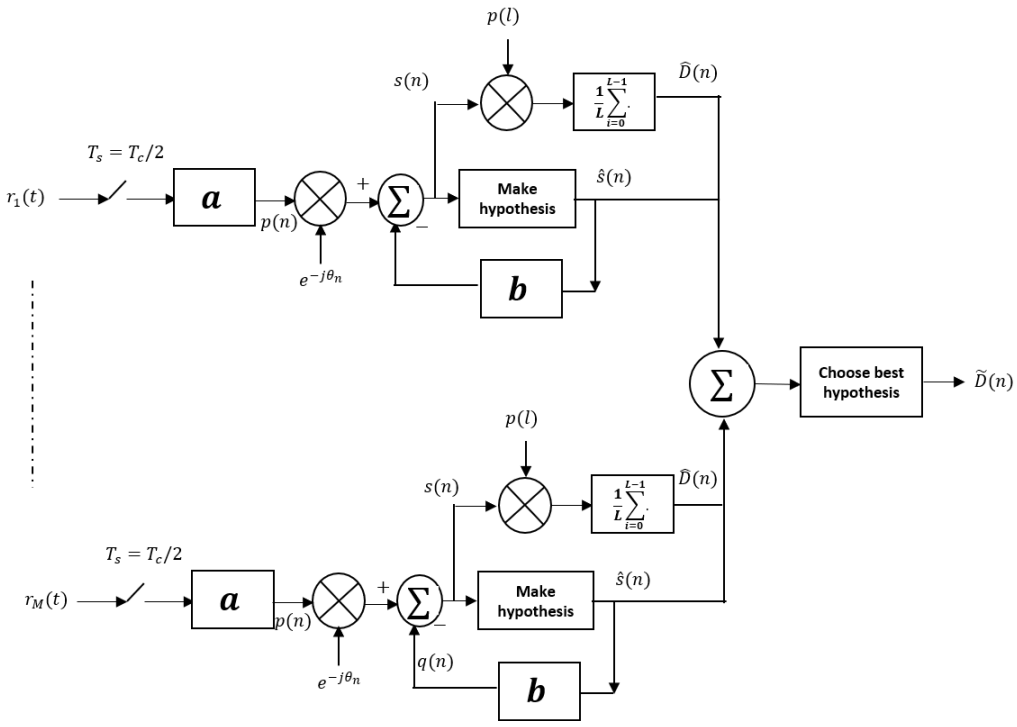

Figure 5.10: A space-time equalizer using multiple hydrophones at the receiver.

Receiver Performance in a Realistic Environment

The performance of the hypothesis DFE using an array of sensors is characterized for signals processed in a frequency flat channel and in multipath conditions. To this end, the QPSK signal is transmitted over a five-tap time-invariant channel with $h[n] = [1\ 0.7\ 0.5\ 0.1\ 0]$, and its BER is compared in the presence of AWGN and measured DalComm1 noise. The feedforward filter size is $N_1 + N_2 + 1 = 9$ taps, the feedback filter is of length $K' = 4$ and the processing gain $L = 2$ throughout the simulations.

Fig. 5.11 shows the simulation scenario in which the communications signals are processed in a flat fading channel. Fig. 5.11a shows the computed feedforward and feedback weights for the first 10,000 symbols, while Fig. 5.11b shows the BER for $M = 4$ computed when the signals are processed in AWGN and empirical DalComm1 noise. From Fig. 5.11a, by updating the filter coefficients at each symbol, it is observed that the filter weights converge quickly so that the BER can be evaluated.

Also, it is observed that the BER improves compared to the theoretical AWGN values for BPSK signals. The comparison between the simulated BER in AWGN and the theoretical values also confirm that the multi-element DFE with hypothesis testing is able to provide diversity gain. For signals processed in measured DalComm1, compared to the BER in Fig. 5.4 where the BER diverges at higher SNR values, the hypothesis testing DFE is able to converge the BER to reasonably lower values at higher SNR.

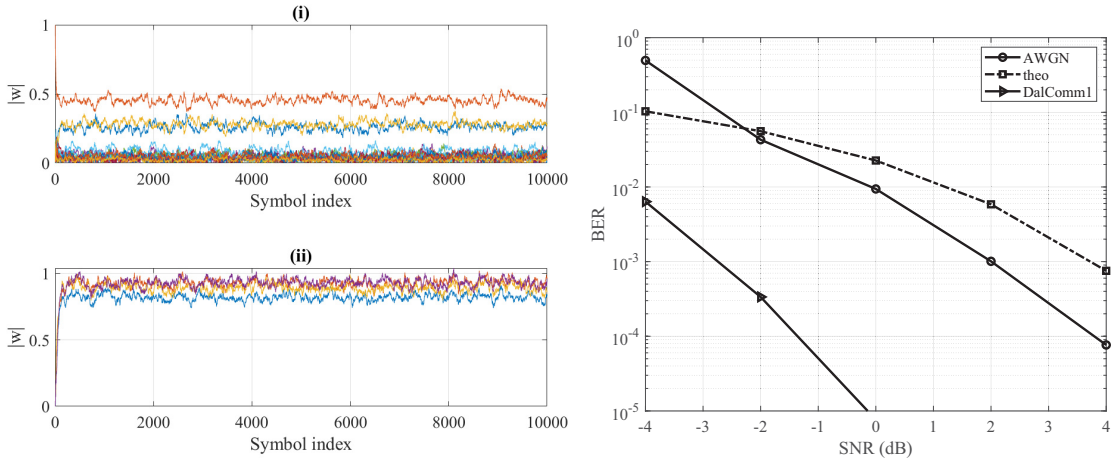

(a) DFE weights (b) BER in AWGN

Figure 5.11: a(i) $\Longrightarrow$ the feedforward weights, and a(ii) $\Longrightarrow$ feedback weights; computed for a four-element array (i.e $M = 4$) in a frequency flat channel. (b) $\Longrightarrow$ the SNR versus BER of the hypothesis testing DFE for signals in measured DalComm1 noise and in AWGN.

Fig. 5.12 shows the second simulation scenario in which the signal of interest is transmitted through a multipath channel and noise is added at the receiver. Fig. 5.12a shows the weights computed for the DFE, while Fig. 5.12b shows the BER for signals processed in a multipath channel and the additive noise is AWGN and empirical DalComm1 noise.

Just as in the single tap channel (i.e frequency-flat), it is observed that the hypothesis testing DFE provides diversity gain even in multipath conditions. It is also observed that the feedback weights provide an equivalent estimate of the channel tap gains. Further, the filter structure is able to make the BER converge at higher SNR values.

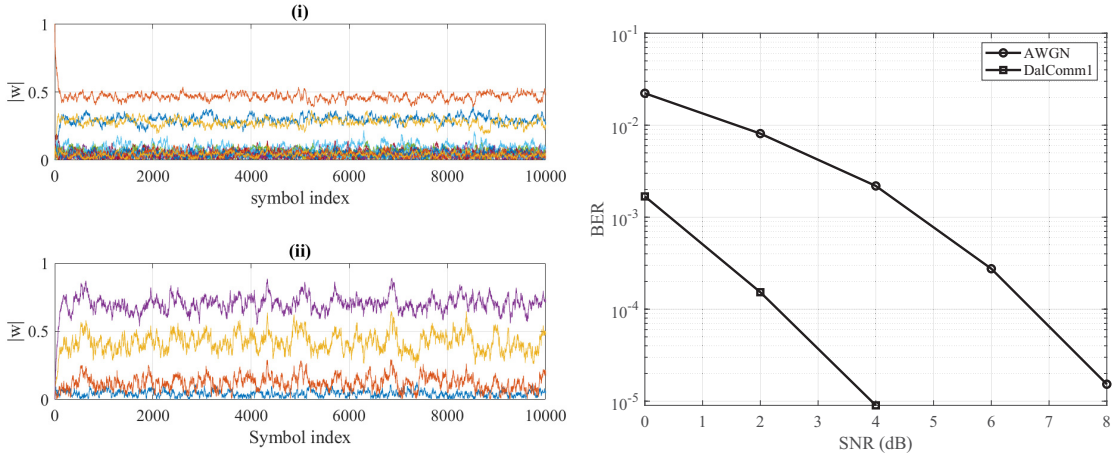

(a) Adaptive weights in multipath channel (b) BER in multipath channel

Figure 5.12: a(i) $\Longrightarrow$ the feedforward weights, and a(ii) $\Longrightarrow$ feedback weights; computed for a four-element array (i.e $M = 4$) in a time-invariant multipath channel. (b) $\Longrightarrow$ the SNR versus BER of the hypothesis testing DFE for signals propagated through a multipath channel and processed in measured DalComm1 noise and AWGN.

It is noteworthy that the multi-element DFE with hypothesis testing is tested by constantly updating the filter coefficients at the symbol rate. The constant update maximizes the link performance against the temporary variations in the noise channel. Not shown, but it is expected that the filter will also provide an improved performance in time-varying multipath channels.

From these observations about OAN compared with AWGN, it can be concluded that the performance of an UWA receiver in OAN is different when compared in the presence of uncorrelated white Gaussian noise. In fact, both metrics – the AG and the BER, which are the most commonly used figure of metrics for characterizing UWA receivers do not agree with the usual assumption that noise in an UWA receiver is uncorrelated in space and/or time. To optimize the UWAC link in the presence of OAN, the filter weights must be re-trained to adapt to the temporal variations in the statistics of OAN.

5.3 Mitigating the Impact of Ambient Noise in a Measured Channel

In this section, the impact of measured OAN is evaluated for communication signals in measured DalComm1 channel. The CIR is obtained from the post-processing of the

propagation channel measurements described in Section 4.2. Recall that the channel profiles for DalComm1 were shown in Section 2.3. Particularly, the channel profile over the 10 km range depicted in Fig. 2.5 is applied in this section.

To this end, the communication signal is simulated as described in Section 5.1.1. The signal is propagated through a snapshot of the 10 km CIR, such that the CIR is time-invariant. The measured OAN from DalComm1 is added artificially at the receiver such that the communication link is representative of a realistic environment. The DFE characterized by (5.19) is applied to mitigate the impact of the channel distortion and noise.

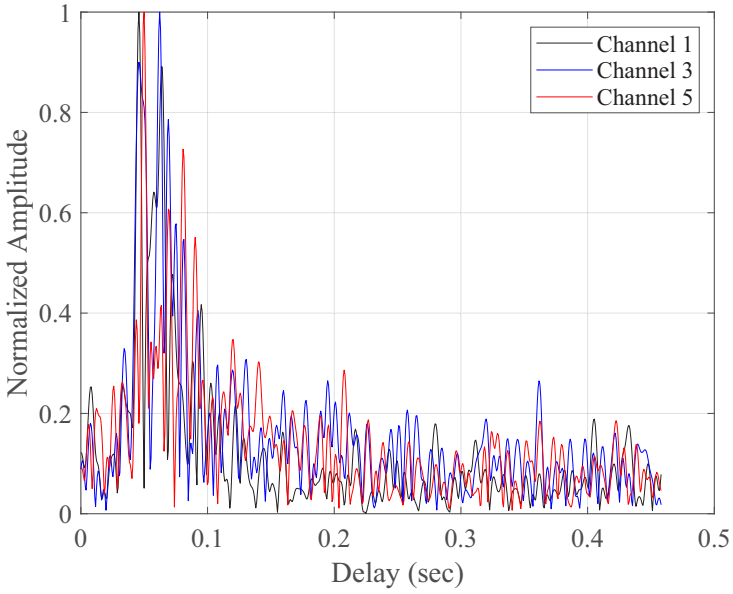

Figure 5.13: A snapshot of the CIR for a 10 km propagation range, obtained from the DalComm1 measurements.

A snapshot of the CIR is depicted in Fig. 5.13. It is observed that the rms delay spread is about 63 ms. The CIR is normalized so that there are six tap gains with significant energies. Across the M-element array, it is also noteworthy the channel is sparse with zero values in the channel profile across the array elements. This observation is typical in the UWAC channel, making it more challenging to mitigate the impact of the channel on the information symbols.

To compare the BER performance of the multipath signal in the presence of

measured noise and AWGN, the DFE is trained using 1024 symbols and the payload length is also 1024 which is approximate a 4 second duration. A total of 10^6 payload symbols are transmitted and the BER is computed at each input SNR value. Note that the simulation conditions are exactly the same when the multipath signal is processed in measured DalComm1 noise and in AWGN.

From Fig. 5.14, similar to the observation in Fig. 5.4, the BER computed by using one receive element closely compare for signals in AWGN and DalComm1 noise. However, for $M = 3$, the SNR is improved by 1.2 dB to obtain a BER of 10^{-1}, while for $M = 5$, the SNR is lower by 2 dB to obtain a BER of 10^{-1}. Also, the BER worsens significantly at input SNR values greater than 16 dB. This also confirms that the statistics of OAN changes when averaged over time and can impact the BER performance of an UWAC receiver even in multipath conditions.

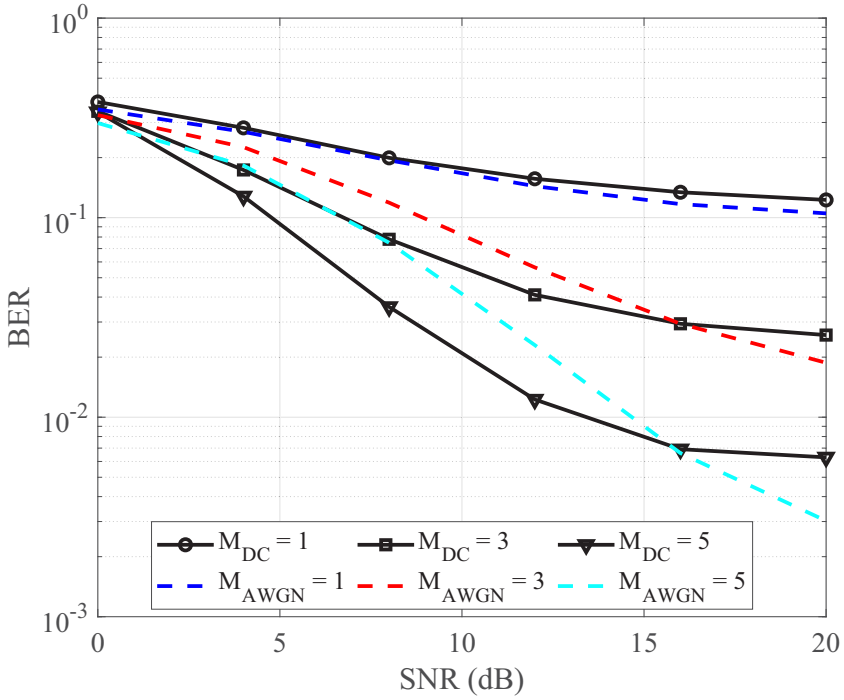

Figure 5.14: The BER of signals processed in DalComm1 propagation conditions. The CIR is computed from the 10 km range and measured DalComm1 noise (DC) is applied.

In summary, the assertion that OAN impacts the performance of an acoustic receiver differently compared to AWGN has been further strengthened even when the signal is propagated through a sparse multipath channel. In fact, just as stated in

[?], an UWA channel model that excludes the impact of ambient noise can be highly inaccurate. It is suggested that the discrepancy between UWAC systems performance in actual ocean deployments compared to the models can be attributed to the bias introduced by a wrong assumption that the OAN channel is uncorrelated noise in space and time.

Thus far, the impacts of noise that excludes impulsive or transient sources (due to vessel) have been described. In Section 5.4, the impact of vessel noise on the spatial AG is discussed.

5.4 Mitigating the Impact of Vessel Noise in UWAC

Noise interference emanating from vessels are often present during underwater acoustic measurements especially with the increase in shipping activities in recent times. Vessel noise overwhelms communication signals and make the decoding quite cumbersome or impossible. This problem is particularly apparent in harbours, and near the littoral, where communication link may be corrupted for example by fleets of vessels, and fishing boats passing in close proximity of the sensor.

In a recent work [?], deep learning was applied to mitigate shipping noise in an UWA OFDM system. The results showed that the deep learning framework is more efficient in lower bandwidths where shipping noise samples are more correlated than in the higher bandwidths. Also, in [?], it was noted that most algorithms that have been developed for mitigating transient noise (particularly shipping noise) rely on the statistical knowledge of the noise process to achieve accurate estimation of the noise. The author also noted that there are currently little or no work available in literature on mitigating impulsive noise interference emanating from nearby shipping activity.

Several authors [3, ?, ?, ?] have demonstrated the impact of impulsive noise on UWAC links, but developing robust receivers that are able to mitigate vessel noise remains an arduous task. Hence, mitigating the impact of shipping noise in UWAC cannot be overemphasized, even in OFDM systems as demonstrated in [?, ?].

Thus far in this chapter, the communication link has been modelled as narrowband, so that the impact of OAN can be evaluated pertinently over a narrow spectrum of 240 Hz. However, since the spectrum of vessel noise could extend over a very wide

bandwidth, the communication system discussed in this section is modelled as wideband. Therefore, in this section, the signal of interest is modeled by a chirp signal. The chirp signal is representative of a broadband signal which has been proposed for UWAC applications. In some wideband UWA applications, chirp signals are desirable because they exploit the low Doppler sensitivity as well as their great autocorrelation properties especially in applications where either the source or the receiver are in motion [**?**, **?**]. In fact, recently, Orthogonal Chirp Division Multiplexing has been studied as an alternative to OFDM, because of its resilience to Doppler shift [**?**].

The chirp signal is simulated such that it's duration can be approximated to the spatial snapshot duration of the ML-BF in Section 3.5. Recall that the each spatial snapshot of the measured acoustic pressure from CANAPE and ADEON occupies 4096 points and the original sampling frequency is 1.6 kHz. However, in this section, the noise recording is bandlimited to 1000 Hz and at a centre frequency of 1000 Hz. Hence, the chirp signal occupies a bandwidth of 1 kHz and duration of 0.25 seconds.

As discussed in Chapter 3, narrowband beamformers can be applied in wideband applications by dividing the system's bandwidth into sub-bands in which beamforming algorithms can be applied. In fact, in Chapter 3, the ML-BF was applied for estimating the bearing of vessels that within a few hundreds of meters to an acoustic array. In this section, the MVDR beamformer is developed as a viable algorithm applied to reduce the noise contribution emanating from a vessel, by placing nulls in the direction of the interferer (vessel) even in wideband conditions in an UWAC link.

Hence, three simulation scenarios are defined to demonstrate that the wideband beamformer can be applied to mitigate vessel noise in wideband UWAC systems. Note that the methodology developed in this section is for demonstration purposes only.

Simulation Scenarios

To demonstrate the beamforming approach, first, an MVDR beamformer is applied to mitigate a narrowband interference source depicted through simulation by a single tone at 2.25 kHz arriving from a direction $d(\theta, \phi) = [56°, 0°]$, where θ is the azimuth and ϕ is the elevation.

In a second scenario, the MVDR beamformer is applied for mitigating multiple interfering sources received as plane waves from three different impinging angles $d_1(\theta, \phi) = [64°, 0°]$, $d_2(\theta, \phi) = [32°, 0°]$ and $d_3(\theta, \phi) = [10°, 0°]$ at the receiver. In these simulation scenarios, the chirp signal is normalized to a unit power.

In a third scenario, the MVDR beamformer is applied over a wide bandwidth to mitigate the noise emanating from ADEON's vessel. The noise recording is bandlimited to 1000 Hz at a centre frequency of 1000 Hz and added to the chirp signal which is the synthetic signal of interest with an impinging angle of 90° with respect to the plane of the array. The vessel is treated as a directional source of interference with a known bearing, since the directionality of the vessel was already estimated in Chapter 3. Hence, the instantaneous bearing of the vessel computed in Chapter 3 is applied in this simulation. This section is limited to the ADEON array since the sonar interference in CANAPE significantly distorts the accuracy of the beamformer. The four spatial elements of the ADEON array are applied in this section. This is primarily due to the fact that the same elements were used to compute the directionality of the vessel in Chapter 3.

At the beamformer, the system bandwidth is divided into 64 equal sub-bands and the MVDR was applied in each sub-band. The spatial weights are computed using the sub-band MVDR such that nulls are placed in the estimated direction of the vessel. The simulation was developed using the Phased Array toolbox in Matlab. The array gain of the MVDR beamformer is computed from [17]

$$\mathrm{AG} = \mathbf{v}^H \boldsymbol{\rho}_x^{-1} \mathbf{v}, \tag{5.26}$$

where $\mathbf{v}$ is the steering vector, the normalized spectral matrix $\boldsymbol{\rho}_x = \mathbf{R}_{xx} P_n$, the superscript H is the hermitian operator, $\mathbf{R}_{xx}$ is the covariance matrix of the received signal and P_n is the input noise power.

Demonstration of the Wideband Beamforming Technique

In the first simulation scenario, the beamformer nulls a single tone interference with frequency 2.25 kHz arriving from $d(\theta, \phi) = [56°, 0°]$. Fig. 5.15b depicts the first simulation scenario with a single tone interference which was combined with an input noise at -7 dB. The signal power is normalized to unity. It can be observed from Fig. 5.15b

that the beamformer nulls the interferer whose bearing is from 56°. Similarly, the chirp signal was recovered with an output AG of 11.7 dB as shown in Fig. 5.15a.

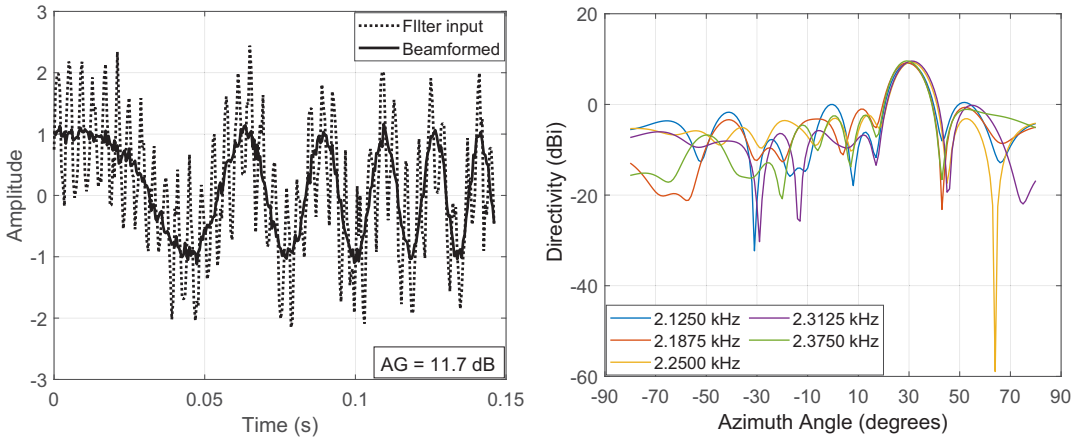

(a) (b)

Figure 5.15: (a) The input and output of the MVDR beamformer for signals processed in AWGN. (b) The beam pattern at the output of the MVDR beamformer showing that a null was placed at a single tone 2.25kHz interference sine wave impinging at $[56°, 0°]$ for a signal processed in AWGN.

In the second simulation scenario, the chirp signal is received alongside three sources of interference combined with noise at an input SNR of -30 dB as depicted in Fig. 5.16b. It is observed that the sources of interference measured as plane waves at the array are nulled in the 10°, 32° and 64° respectively. Similarly in Fig. 5.16a, the signal of interest is recovered with an AG of 18 dB. This observation shows that the wideband MVDR beamformer is able to mitigate multiple sources of interference in wideband conditions. Note that the array response showed in Fig. 5.15b and Fig. 5.16b depict just five frequency bands out of the full system bandwidth. This is done to avoid cluttered plots which makes the results harder to interpret. These frequency bins are rendered in the rest of the results discussed in this section.

Beamforming Application for Vessel Noise Mitigation

In the third simulation scenario, the wideband MVDR is applied to process the chirp signal while the source of interference is the measured vessel noise from the ADEON experiment. The four elements of the ADEON array are applied in this section to

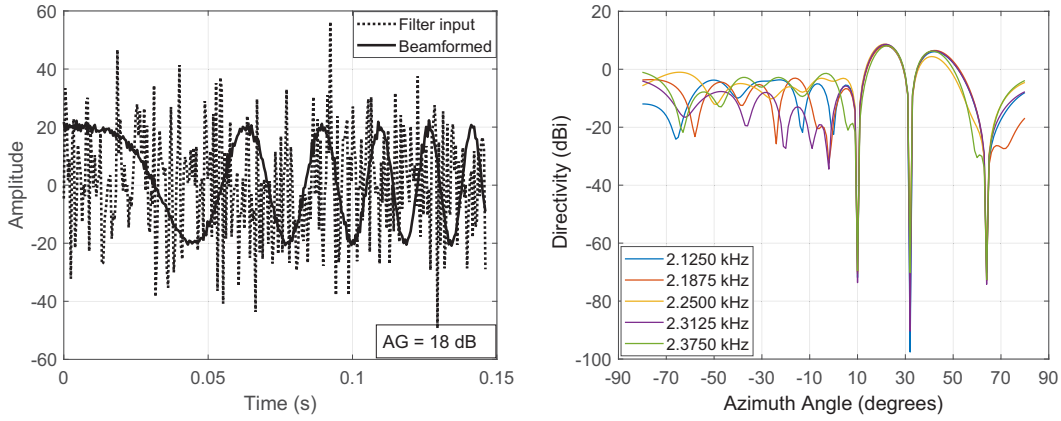

(a) (b)

Figure 5.16: (a) The input and output of the MVDR beamformer for a chirp signal processed in AWGN and multiple interferers (plane waves). (b) The beam pattern at the output of the MVDR beamformer showing that nulls were placed at in the direction 10°, 32° and 64° of the interferers.

mitigate the impact of the vessel noise on the chirp signal. The measured vessel noise is processed over K snapshots as described in Section 3.5. After bandlimiting the noise, each snapshot of the time series occupies a window of 512 points (i.e. about 0.25 seconds) in which the beamformer is applied.

It is observed from Fig. 5.17b and Fig. 5.17d that the beamformer is able to place a null in the direction of the vessel from 42° and 132° at discrete time intervals. A second null (at about 48°) is observed in Fig. 5.17d, suggesting that multiple energy peaks are present at this time. Also, Fig. 5.17a and Fig. 5.17c show a gain of about 18.4 dB and 5.6 dB respectively, measured at the output of the beamformer.

Fig. 5.17b represents the time when the vessel was relatively approaching the array, while at the snapshot at Fig. 5.17d represents the vessel while traveling away from the array. This observation can also be confirmed in Fig. 3.15. Although the specific range of the vessel at these discrete snapshots are not accurately known (as described in Section 3.6.4), by visually inspecting the power spectrum of the time series or by an audio inspection, it can determined whether the vessel is close to the array or not.

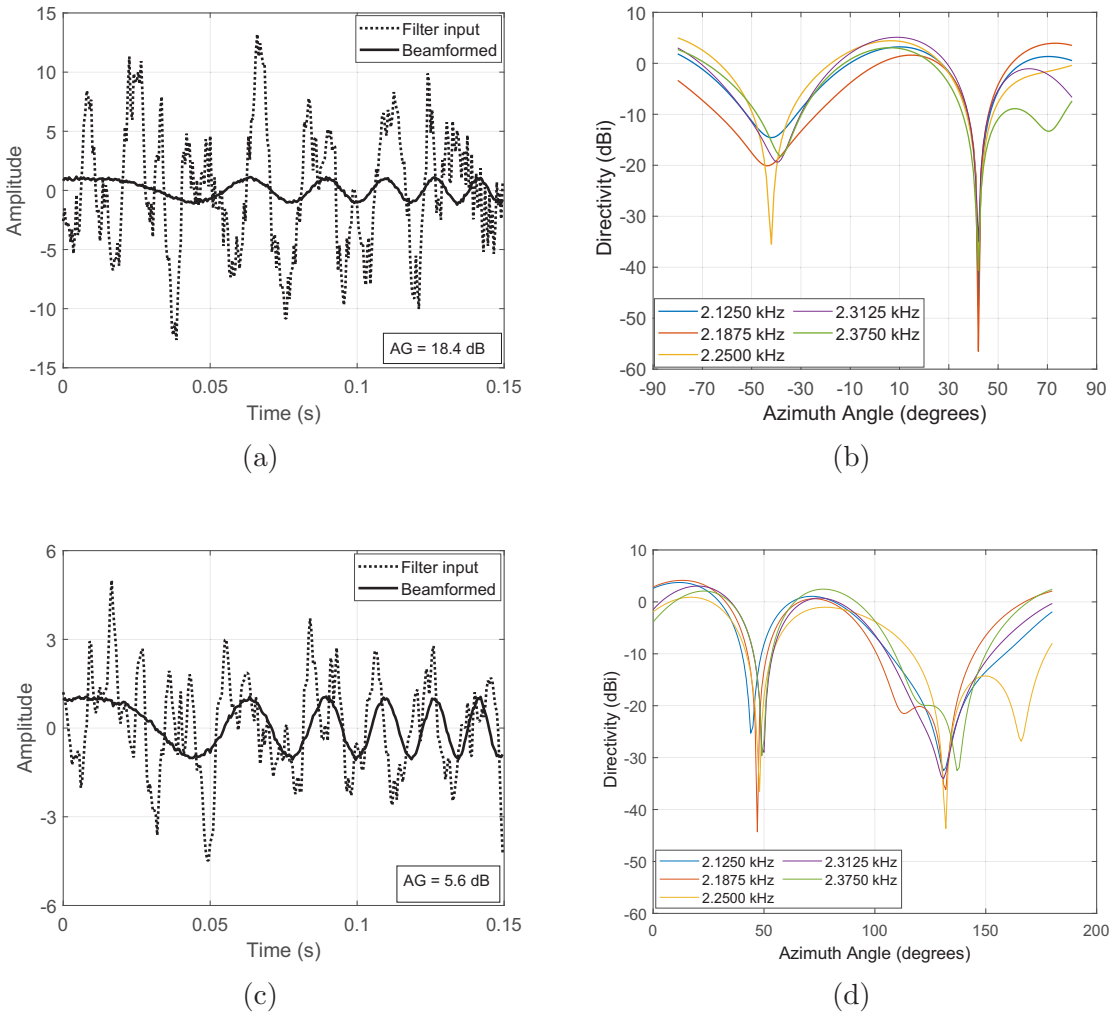

Figure 5.17: Fig. (a), (c) shows the beamformer input and the recovered signals at the output of the beamformer, while Fig. (b), (d) shows the beam pattern for vessel noise impinging at 42° and 132° respectively.

In this section, with a prior knowledge of the directionality of a vessel, it is demonstrated that the wideband beamformer is able to improve the quality of the received signal significantly. The beamformer was able to achieve a gain of about 18 dB when the vessel is at a relatively close distance to the array.

5.5 Chapter Summary

The contributions in this chapter are in three parts. First, are the computational analyses of the impacts of OAN compared to that of AWGN in an UWAC link. Second, is the design of a space-time decision feedback equalizer combined with spread spectrum technology used to improve the communication reliability over an array of receivers. Third, is the description of a beamforming technique that is applicable for mitigating vessel noise in a broadband UWAC link.

To summarize, the impact of ocean ambient on an UWAC system has been demonstrated in this chapter. First, it has been shown that the AG and the BER of signals processed in OAN do not compare with that of AWGN. It has also been shown that defining an optimum frame structure that is able to adapt to the temporal variability in OAN is key to maximizing the link reliability. The accuracy of the noise models described in this work has been tested in an UWAC receiver. Furthermore, a DFE with hypothesis testing applied for an array of receivers has been been developed. It was demonstrated that this receiver structure is able to mitigate the impact of OAN even in realistic deployment conditions where the signal is propagated with multipath reflections. Finally, a wideband MVDR beamformer has been applied to mitigate the impact of vessel noise in a broadband signal. A summary of the research developed in this dissertation is presented in Chapter 6.

Chapter 6

Conclusion

In this work, three different contributions have been presented on the central theme of OAN. First, the directional properties of OAN have been characterized through acoustic source localization. Second, two distinct models have been developed to characterize the properties of ambient noise. Third, the impact of ambient noise on an UWAC receiver has been analyzed. The methodologies developed in this work have been applied to actual acoustic measurements derived from three different experiments – CANAPE, ADEON and DalComm1.

In the first contribution, a ML beamformer has been applied to demonstrate the directional property of OAN. A combination of the ML-BF and the CB-MFP has been applied to track the course of vessels from measured acoustic data. Measured noise from the CANAPE and ADEON experiments were used to characterize the ability of these algorithms to estimate the bearing and range of the vessels to the arrays. The AIS positions reported on CANAPE's vessel have been compared with the results from the acoustic processing. Although, there were insufficient data points obtained from the AIS, it was demonstrated that the AIS also detects a vessel in the vicinity of the array. Also, it has been demonstrated that the limitation of the CB-MFP is constrained on the ability of the array to capture sufficient interference pattern, which is determined by the elemental separation of the VLA.

In the second contribution, two distinct methodologies – the DBM and the CBM have been developed to model the properties of ambient noise. The DBM relies on the knowledge of the directionality function of the noise field, while the CBM relies on the knowledge of the coherence function at any pair of spatial sensors. Either method is applicable to characterize the noise properties depending on the application and whether the noise directionality or the coherence is known. However, it was found that in an UWAC system, the CBM is better applicable when using the array gain as a figure of merit to characterize the system performance. Both methodologies do

not perfectly compare with the BER analysis in measured DalComm1 noise. It is proposed that the noise models be optimized by including temporal variability in the noise statistics.

In the third contribution, the impact of ambient noise on an UWAC system was verified. The assumption of uncorrelated OAN in an UWAC link was verified as inaccurate and the impact of the directionality of OAN in a narrowband communication system was established. It was established that for a 5-element array, the STF must be trained for at least 4 seconds to achieve convergence in the presence of space-time ambient noise. Also, to achieve a relatively constant BER, the STF must be retrained after approximately 4 seconds, since as the payload duration becomes excessively long, the BER degrades, although marginally due to the temporal change in the space-time noise properties.

Furthermore, a STF that is able to mitigate the multipath channel distortion as well as OAN in realistic conditions has been described. Finally, a wideband beamformer was proposed at the receiver to mitigate the impact of vessel noise on an array of receivers. It was established that the beamformer can achieve up to about 18 dB gain in the presence of vessel noise. It was also noted that just as in the estimation of the vessel's directionality, the performance of the beamformer will be degraded when the vessel is in a close proximity to the array.

Overall, this work demonstrates that naturally occurring ambient noise sources can impact the reliability of an UWAC link. It is proposed that the UWAC channel propagation model must include the impact of ambient noise to achieve a high reliability, especially in noisy environments where low power transmission is also a requirement. More importantly, the impact of OAN even in narrowband conditions has been evaluated. Therefore, the findings from this research can be applied in narrowband subcarrier system.

The author hopes that the results from this research enlightens the UWAC community about the impact of OAN on the UWAC link. It is highly recommended that the design of narrowband UWAC system and even narrowband subcarrier systems must consider the impact of directional ambient noise to achieve optimum signal detection at the receiver.

Bibliography

[1] R. J. Urick, "Principles of Underwater Sound for Engineers," *McGraw-Hill, New York*, pp. 181–210, 1967.

[2] S. Haykin and S. Haykin, *Adaptive Filter Theory*. Pearson, 2014.

[3] M. A. Chitre, J. R. Potter, and S.-H. Ong, "Optimal and near-optimal signal detection in snapping shrimp dominated ambient noise," *IEEE J. of Oc. Eng.*, vol. 31, no. 2, pp. 497–503, 2006.

[4] H. Cox, "Spatial correlation in arbitrary noise fields with application to ambient sea noise," *J. Acoust. Soc. Am.*, vol. 54, no. 5, pp. 1289–1301, 1973.

[5] B. F. Cron and C. H. Sherman, "Spatial-Correlation Functions for Various Noise Models," *J. Acoust. Soc. Am.*, vol. 34, no. 11, pp. 1732–1736, 1962.

[6] F. Jensen, W. Kuperman, M. Porter, and H. Schmidt, *Computational Ocean Acoustics*. American Inst. of Physics, 2000. [Online]. Available: https://books.google.ca/books?id=QHtx4zYPbzMC

[7] D. R. Jackson, "APL-UW High-Frequency Ocean Environmental Acoustic Model Handbook," *Technical Report*, 1994.

[8] Chitre, Mandar, "A High-frequency Warm Shallow Water Acoustic Communications Channel Model and Measurements," *The Journal of the Acoustical Society of America*, vol. 122, no. 5, pp. 2580–2586, 2007. [Online]. Available: http://scitation.aip.org/content/asa/journal/jasa/122/5/10.1121/1.2782884

[9] T. S. Rappaport, *Wireless Communications, Principles and Practice*. Prentice Hall, 1996.

[10] M. J. Buckingham, "Theory of the directionality and spatial coherence of wind-driven ambient noise in a deep ocean with attenuation," *The Journal of the Acoustical Society of America*, vol. 134, no. 2, pp. 950–958, 2013. [Online]. Available: https://doi.org/10.1121/1.4812270

[11] P. L. Brockett, M. Hinich, and G. R. Wilson, "Nonlinear and non-Gaussian ocean noise," *J. Acoust. Soc. Am.*, vol. 82, no. 4, pp. 1386–1394, 1987.

[12] M. Cobos, F. Antonacci, A. Alexandridis, A. Mouchtaris, and B. Lee, "A Survey of Sound Source Localization Methods in Wireless Acoustic Sensor Networks," *Wireless Communications and Mobile Computing*, vol. 2017, pp. 1–24, 08 2017.

[13] S. Pensieri, R. Bozzano, J. A. Nystuen, E. N. Anagnostou, M. N. Anagnostou, and R. Bechini, "Underwater acoustic measurements to estimate wind and rainfall in the mediterranean sea," *Advances in Meteorology*, vol. 2015, 2015.

[14] B. B. Ma and J. A. Nystuen, "Passive Acoustic Detection and Measurement of Rainfall at Sea," *Journal of Atmospheric and Oceanic Technology*, vol. 22, no. 8, pp. 1225–1248, 2005.

[15] D. Tse and P. Viswanath, *Fundamentals of Wireless Communication*, 2005.

[16] D. G. Manolakis and V. K. Ingle, *Applied Digital Signal Processing: Theory and Practice*. Cambridge University Press, 2011.

[17] H. Van Trees, *Optimum Array Processing*. Wiley-Interscience, 2001, no. pt. 4. [Online]. Available: https://books.google.ca/books?id=BYPkswEACAAJ

[18] W. Liu and S. Weiss, *Wideband Beamforming: Concepts and Techniques*. Wiley Publishing, 2010.

[19] A. Egbewande and J. Bousquet, "Space-Time Noise Characterization for Underwater Acoustic Communications," in *OCEANS 2018 MTS/IEEE Charleston*, 2018.

[20] A. Egbewande and J.-F. Bousquet, "Measurement of a Space-time Noise Mitigation Technique," in *Proceedings of the International Conference on Underwater Networks & Systems*. ACM, 2017, p. 26.

[21] M. B. D. J. Piper, G.D Cameron, "Quaternary Geology of the Continental Margin of Eastern Canada," *Geol. Surv. Canada, Map A*, vol. 1711, 1988.

[22] D. R. Barclay and M. J. Buckingham, "Depth dependence of wind-driven, broadband ambient noise in the Philippine Sea," *The Journal of the Acoustical Society of America*, vol. 133, no. 1, pp. 62–71, 2013.

[23] A. V. Oppenheim, R. W. Schafer, and J. R. Buck, "Discrete-time signal processing (2nd ed.)," *Prentice-Hall, Inc.*, 1999.

[24] L. M. Wolff and S. Badri-Hoeher, "Convolutionally coded hopping pattern for mfsk modulation in underwater acoustic communication," *IEEE Access*, vol. 7, pp. 95 569–95 575, 2019.

[25] J. Potter, J. Alves, D. Green, G. Zappa, I. Nissen, and K. McCoy, "The janus underwater communications standard," in *2014 Underwater Communications and Networking (UComms)*, 2014, pp. 1–4.

[26] R. P. Gooch and B. J. Sublett, "Joint spatial and temporal equalization in a decision-directed adaptive antenna system," in *Twenty-Second Asilomar Conference on Signals, Systems and Computers*, vol. 1. IEEE, 1988, pp. 255–259.

[27] H. Song, "An Overview of Underwater Time-Reversal Communication," *IEEE Journal of Oceanic Engineering*, vol. 41, no. 3, pp. 644–655, July 2016.

[28] M. Stojanovic, J. A. Catipovic, and J. G. Proakis, "Reduced-complexity spatial and temporal processing of underwater acoustic communication signals," *The Journal of the Acoustical Society of America*, vol. 98, no. 2, pp. 961–972, 1995.

[29] M. Stojanovic, J. Catipovic, and J. Proakis, "Phase-coherent digital communications for underwater acoustic channels," *IEEE J. Oceanic Eng.*, vol. 19, no. 1, pp. 100–111, 1994.

[30] M. Stojanovic and L. Freitag, "Hypothesis-feedback equalization for direct-sequence spread-spectrum underwater communications," in *OCEANS MTS/IEEE Conference and Exhibition*, vol. 1, 2000, pp. 123–129 vol.1.

[31] ——, "Multichannel Detection for Wideband Underwater Acoustic CDMA Communications," *IEEE J. Ocean. Eng.*, vol. 31, no. 3, pp. 685–695, July 2006.